

Vertex reconstruction in large liquid scintillator detectors

Vertex-Rekonstruktion in großen Flüssig- szintillator-Detektoren

by

David J. Meyhöfer

date of birth

November 15th, 1989

Master thesis in physics

Universität Hamburg

2016

1st reviewer: Prof. Dr. Caren Hagner

2nd reviewer: Dr. Björn Wonsak

Abstract

Large liquid scintillator detectors require an event reconstruction to determine the course of an event. Examples are the Jiangmen Underground Neutrino Observatory (JUNO), which is currently being built in China and the Low Energy Neutrino Astronomy (LENA) detector.

During this thesis a vertex reconstruction was developed. It is able to determine the event start time and position. In principle it can be applied to any unsegmented liquid scintillator detector and does not rely on the detector geometry. The reconstruction is able to determine the vertex for events with an energy ranging from a few MeV up to GeV and has been applied to events simulated in the LENA detector and in the JUNO detector. In the LENA detector for 10k simulated electron events in the energy range of 0.5 to 10 MeV the vertex was determined with a standard deviation of ± 14.06 cm. In the energy range of 5 to 10 GeV the reconstruction determined the particle track direction. For 99.2% of 2.5k muon events simulated in the LENA detector the true track direction was determined within 25 degrees and the distance of the reconstructed vertex to the track was determined with a standard deviation of ± 34.56 cm.

Zusammenfassung

Große Flüssigszintillator-Detektoren benötigen eine Event-Rekonstruktion, um den Ablauf eines Events zu bestimmen. Beispiele sind das Jiangmen Underground Neutrino Observatory (JUNO), das gerade in China gebaut wird und der Low Energy Neutrino Astronomy (LENA) Detektor.

Während dieser Thesis wurde eine Vertex-Rekonstruktion entwickelt. Die Event-Startzeit und die Position können bestimmt werden. Im Prinzip kann diese auf alle unsegmentierten Flüssigszintillator-Detektoren angewendet werden und braucht keine Rücksicht auf die Geometrie des Detektors zu nehmen. Der Rekonstruktion ist es möglich, den Vertex für Events mit einer Energie von einigen MeV bis zu GeV zu bestimmen. Sie wurde auf simulierte Events im LENA-Detektor und im JUNO-Detektor angewendet. Für 10k im LENA-Detektor simulierte Elektronen-Events mit einer Energie von 0,5 bis 10 MeV konnte der Vertex mit einer Standardabweichung von $\pm 14,06$ cm bestimmt werden. In dem Energiebereich von 5 bis 10 GeV bestimmt die Rekonstruktion die Teilchenspurrichtung. Für 99,2% der 2,5k im LENA-Detektor simulierten Myon-Events konnte die wahre Richtung innerhalb von 25 Grad bestimmt werden und der Abstand von rekonstruiertem Vertex zur Spur wurde mit einer Standardabweichung von $\pm 34,56$ cm bestimmt.

Contents

Introduction	1
1 Neutrino physics	3
1.1 History	3
1.2 Neutrinos as part of the Standard Model	4
1.3 Interaction & detection	6
1.4 Origins of neutrinos	8
1.5 Neutrino physics today	14
1.5.1 Neutrino flavor oscillation	14
1.5.2 Neutrino mass ordering	16
1.5.3 Open questions	17
2 Large liquid scintillator detectors	19
2.1 Light in a liquid scintillator detector	20
2.1.1 Light emission	20
2.1.2 Light propagation	23
2.1.3 Light detection	24
2.2 LENA detector	29
2.2.1 Physics motivation	29
2.2.2 Design	30
2.3 JUNO detector	33
2.3.1 Physics motivation	34
2.3.2 Design	36
3 Event simulation	39
3.1 LENA simulation	39
3.1.1 Geometrical layout	39
3.1.2 Material physics and light emission model	41
3.1.3 PMT model	43
3.2 JUNO-simulation	45
3.2.1 Geometrical layout	45
3.2.2 Material physics and light emission model	46

3.2.3	PMT model	49
4	Reconstruction	51
4.1	Reconstructions for LENA	52
4.1.1	Novel Track Reconstruction for LENA	52
4.2	Reconstructions for JUNO	54
4.2.1	Low energy	54
4.2.2	High energy	56
5	The vertex reconstruction	59
5.1	Overview	59
5.1.1	The goal for this vertex reconstruction	59
5.1.2	Underlying principle	59
5.2	Implementation detail	62
5.2.1	Charge barycenter	62
5.2.2	Position grid	63
5.2.3	Time difference histogram	64
5.2.4	Angular acceptance	66
5.2.5	Additional light weighting and evaluation	67
5.2.6	Time fitting and evaluation algorithm	69
5.2.7	Direction determination and HE algorithm	70
6	Results of the vertex reconstruction	75
6.1	LENA-Detector	75
6.1.1	Low energy	75
6.1.2	High energy	84
6.2	JUNO-Detector	91
7	Conclusion and outlook	93
	List of Figures	95
	List of Tables	97
	List of abbreviations and acronyms	99
	Bibliography	101

Introduction

"The progressive development of man is vitally dependent on invention. It is the most important product of his creative brain. Its ultimate purpose is the complete mastery of mind over the material world, the harnessing of the forces of nature to human needs. ..." - Nikola Tesla [64].

To make use of anything nature provides, one needs at least a basic understanding of it. But to advance further and develop humanity as a whole, common knowledge is not enough. This is why physicists strive to describe nature and fundamental research is the foundation of any model that tries to describe it. Experiments are the tool to verify if a model is valid. Inventions and ingenuity always made experiments possible. Today the research is so advanced that experiments need to be carefully planned and simulations are one part to test the feasibility of an experiment. Furthermore, simulations are necessary for the interpretation of data, from the experiment. They help foresee problems and enable one to anticipate possible experimental output before any data is taken. This makes it possible to work with simulated output before the experiment is built, which was done during this thesis.

One field of fundamental research, in physics today, is the measurements of particle properties. A particle that was predicted as early as the 1930s [53] took 20 years to be experimentally proven to exist. The discovery of the neutrino was rewarded with The Nobel Prize in Physics in 1995 [23]. Some of the properties of the neutrino are still subject of research today. Recent experiments pursuing these parameters are, the *Low energy neutrino astronomy* (LENA) experiment and the *Jiangmen underground neutrino observatory* (JUNO). Liquid scintillator detectors have no intrinsic energy threshold and their target material can be highly purified and therefore can have very low radioactive contaminations, which makes them an excellent choice for low energy neutrino event research. In example the LENA project is pursuing low energy neutrino research for solar neutrinos, the diffuse supernova background and the measurement of geo-neutrinos. On the other hand JUNO is designed to precisely measure the flux of low energy reactor neutrinos to determine the neutrino mass ordering.

Simulations for both of these experiments have been developed and reconstructions handling the output are in development. One kind of reconstruction is the determination of position and time of an event inside the detector. It is called a vertex reconstruction. This kind of reconstruction is commonly used for low energy events, which means the MeV range, which is a typical event energy for neutrino interactions in a liquid scintillator detector. For the LENA detector the *Novel Track Reconstruction Approach* [40] has been developed, which in principal

can be used for any unsegmented liquid scintillator detector. It is currently being adapted to also be used with the JUNO simulation.

The goal of this thesis was to develop a reliable method to determine the start position and time for events of a wide energy range, utilizing some of the same methods already used in the *Novel Track Reconstruction Approach*. Additionally the time to determine these parameters should be as short as possible.

The vertex reconstruction developed during this thesis is able to deliver the important input parameters for the *Novel Track Reconstruction Approach*, but can also be used as a standalone reconstruction in LENA and JUNO. To perform the reconstruction the first hits of each event are utilized. By calculating the time of flight, for photons from different positions in the detector to each photo multiplier, the reconstruction is able to determine the vertex for low energy events. For high energy events a direction determination for the particle track is performed. This makes it possible to discriminate photomultiplier tubes with first hits from the vertex and the developed vertex reconstruction for low energies can then also be applied for high energy events.

The structure of this thesis is as follows, in the first chapter neutrino physics is topic. A brief history and the role of the neutrino in the Standard Model is summarized. Furthermore, today's neutrino research as well as interactions and sources of neutrinos are annotated. The neutrino oscillation and mass ordering are to emphasize as important research topics of modern physics. Especially since these are topics that can be very well researched with large liquid scintillator detectors, which are subject of the following chapter. In this second chapter, first the general principle of large liquid scintillator detector is summarized, following *the journey of light*, then later in that chapter first the LENA detector and finally the JUNO detector are motivated and explained. In the third chapter, the LENA-simulation software and the framework utilized to generate simulated events for the JUNO detector are described. These programs have been used to provide the vertex reconstruction with events. A short summary of vertex reconstruction in general and the reconstruction algorithm status of LENA and JUNO are provided in chapter four. The vertex reconstruction, that was developed in the course of this thesis, is explained in detail in chapter five, providing everything from the basic idea to the implementation details. Results of this vertex reconstruction and evaluation of its performance are given in chapter six. Finally a summary and conclusion is given in chapter seven.

Chapter 1

Neutrino physics

1.1 History

Proposal of the neutrino Wolfgang Pauli first postulated the neutrino in the year 1930. He mentioned it in an open letter to *the group of radioactive Ladies and Gentlemen* [53]. A picture of Wolfgang Pauli can be seen in 1.1a and a copy of his letter is shown in figure 1.1b.



Original - Photocopy of PCC 0393
Abschrift/15.12.56 PW

Offener Brief an die Gruppe der Radioaktiven bei der
Gesellschafts-Tagung zu Tübingen.

Abschrift
Physikalisches Institut
der Eidg. Technischen Hochschule
Zürich
Zürich, h. Des. 1930
Gloriastrasse

Liebe Radioaktive Damen und Herren,

Wie der Ueberbringer dieser Zeilen, den ich baldwollst
anuhören bitte, Ihnen des näheren auseinandersetzen wird, bin ich
angesichts der "falschen" Statistik der N- und Li-6 Kerne, sowie
des kontinuierlichen beta-Spektrums auf einen verweifelten Ausweg
verfallen um den "Wechselsatz" (1) der Statistik und den Energiesatz
zu retten. Nämlich die Möglichkeit, es könnten elektrisch neutrale
Teilchen, die ich Neutronen nennen will, in den Kernen existieren,
welche den Spin 1/2 haben und das Ausschliessungsprinzip befolgen und
sich von Lichtquanten ausserdem noch dadurch unterscheiden, dass sie
nicht mit Lichtgeschwindigkeit laufen. Die Masse der Neutronen
würde von derselben Grössenordnung wie die Elektronenmasse sein und
jedenfalls nicht grösser als 0,01 Protonenmasse. Das kontinuierliche
beta-Spektrum wäre dann verständlich unter der Annahme, dass beim
beta-Zerfall mit dem Elektron jeweils noch ein Neutron emittiert
wird, derart, dass die Summe der Energien von Neutron und Elektron
konstant ist.

Nun handelt es sich weiter darum, welche Kräfte auf die
Neutronen wirken. Das wahrscheinlichste Modell für das Neutron scheint
mir aus wellenmechanischen Gründen (näheres weiss der Ueberbringer
dieser Zeilen) dieses zu sein, dass das ruhende Neutron ein
magnetischer Dipol von einem gewissen Moment μ ist. Die Experimente
verleihen wohl, dass die ionisierende Wirkung eines solchen Neutrons
nicht grösser sein kann, als die eines gamma-Strahls und darf dann
 μ wohl nicht grösser sein als $e \cdot (10^{-13} \text{ cm})$.

Ich traue mich vorläufig aber nicht, etwas über diese Idee
zu publizieren und wende mich erst vertrauensvoll an Euch, liebe
Radioaktive, mit der Frage, wie es um den experimentellen Nachweis
eines solchen Neutrons stände, wenn dieses ein ebensolches oder etwa
lokal grösseres Durchdringungsvermögen besessen würde, wie ein
gamma-Strahl.

Ich gebe zu, dass mein Ausweg vielleicht von vornherein
wenig wahrscheinlich erscheinen wird, weil man die Neutronen, wenn
sie existieren, wohl schon längst gesehen hätte. Aber nur wer wagt,
gemut und der Ernst der Situation beim kontinuierlichen beta-Spektrum
wird durch einen Ausspruch meines verehrten Vorgängers im Amt,
Herrn Debye, beleuchtet, der mir kürzlich in Basel gesagt hat:
"0, daran soll man am besten gar nicht denken, sowie an die neuen
Steuern." Darum soll man jeden Weg zur Rettung ernstlich diskutieren.-
Also, liebe Radioaktive, prüfet, und richtet.- Leider kann ich nicht
persönlich in Tübingen erscheinen, da ich infolge eines in der Nacht
vom 6. zum 7. Des. in Zürich stattfindenden Balles hier unabhkömmlich
bin.- Mit vielen Grüssen an Euch, sowie an Herrn Reak, Euer
untertänigster Diener

W. Pauli

(a) A picture of Wolfgang Pauli, taken 1945. (b) The transcription of the letter in which Pauli first mentioned the idea of the neutrino.

Figure 1.1: Left, picture of Pauli 1954 [22]. Right, first mention of the neutrino [53].

The neutrino was proposed as a rescue attempt for the energy conservation, which the β -decay otherwise would have violated. Back then he used the name *neutron* since he thought it to be a neutral particle that exists within the core of an atom. Hence, the name neutr-on, with "-on" being the same ending as electr-on and prot-on, the other particles which at that time were thought to be the only particles that make up an atom. He also predicted that it will be a fermion and that it has spin $1/2$. Most impressively he also projected a small mass and velocity smaller than the speed of light, which does not comply with the *Standard model* (SM), but turned out to be true anyway and is now a hint for physics beyond the SM.

The term neutrino was brought up by Enrico Fermi. 1932 the neutron was found and at first the neutrino and the neutron were thought to be the same particle. Since they were not and to make them distinguishable the name neutrino was used, which means the "little neutral one" in Italian. Fermi published a paper 1934 [21] explaining the theory of β -decay under the assumption that the neutrinos exists, but no attention was given to his work at that time. With the proposed neutrino the β -decay could be described as:



Finally, when experimental evidence indicated a strict limit for electron energy at each type of *beta*-decay, his work found recognition, after Pauli publicly emphasized the existence of the neutrino.

Experimental discovery It took until the 1950th for the neutrino to be experimentally observed. High neutrino flux sources at that time (and still today) were nuclear reactors. The fission process includes unbound neutrons, which are likely to decay via the β^- -decay process. In 1953, a 300 liter liquid scintillator experiment was set up. The experiment of Clyde L. Cowan and Frederick Reines was looking for the reaction:



Due to the small target mass and leak of proper background shielding only a vague signal could be detected. A follow up experiment was conducted, using 4000 liters liquid scintillator and more background shielding. This time a clear signal could be observed. Clyde L. Cowan died in 1974 and Frederick Reines was awarded the Nobel Prize for his work on neutrino physics in 1995 [23].

1.2 Neutrinos as part of the Standard Model

Neutrinos are elementary particles in the standard model (SM) that, have no electric charge and no color charge. They are leptons and have spin $1/2$. The only interaction channels possible for neutrinos are *charged current* (CC) and *neutral current* (NC), which are part of the *weak force*.

The gauge bosons are W^\pm and Z^0 [50]. Neutrinos (antineutrinos) come in three flavors, ν_e ($\bar{\nu}_e$), ν_μ ($\bar{\nu}_\mu$) and ν_τ ($\bar{\nu}_\tau$) and are seen as the lepton counter parts of e , μ and τ . A scheme of the SM can be seen in figure 1.2.

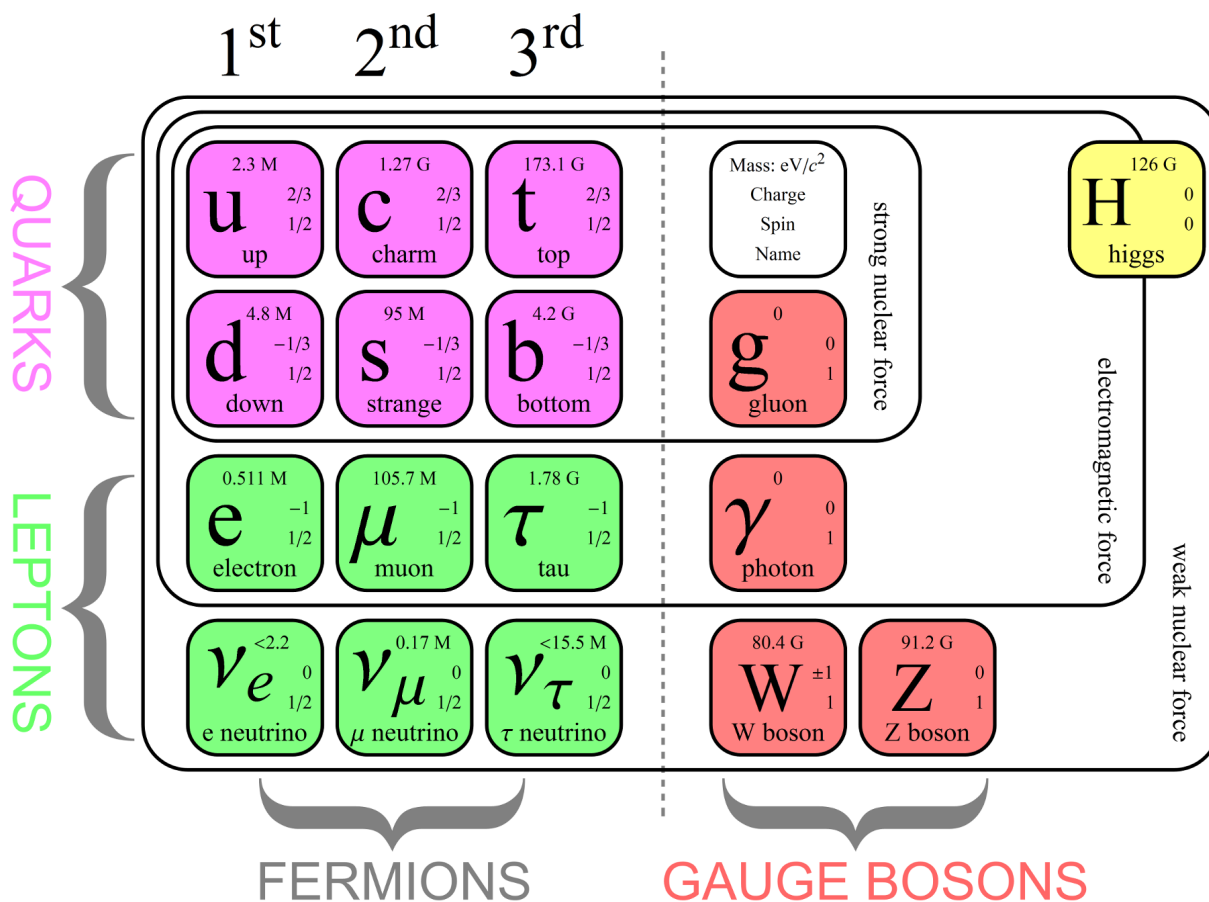


Figure 1.2: A schematic view of the Standard Model, used to illustrate the elementary particles and their interactions. It is to note, that the antimatter partners for each fermion exists in the model, but are not plotted in this picture. The three neutrino generations reside at the bottom left, below their leptonic counter partners. [62]

As e^+e^- -collider experiments indicate, the number of neutrinos with mass smaller than half the mass of Z^0 is 2.9840 ± 0.0082 [50]. The SM has massless neutrinos, which would make neutrino oscillation impossible, but neutrino oscillation has been observed by several experiments [14, 26, 25]. Surprisingly the SM is providing a good approximation for real experiments. This can be understood considering that real experiments are performed with ultra-relativistic neutrinos. This is due to the suppression of the *chiral right-handed* neutrino component and the equivalent *left-handed* antineutrino component. In the SM these components do not exist for neutrinos. For massless particles the *helicity* is valid, the special case of *chirality* for massless particles. The *helicity* projects the angular momentum onto the direction of momentum. A motivation why neutrinos interact in most cases as if they would be massless particles, even though they have mass, is given in the next paragraph.

Chirality As an example the chirality projection operators are used on a spinor travelling along the z axis. The chirality projection operators are defined as follows:

$$P_L = \frac{1}{2}(1 - \gamma^5) \quad \text{and} \quad P_R = \frac{1}{2}(1 + \gamma^5), \quad (1.3)$$

with γ^5 being:

$$\gamma^5 = i\gamma^0\gamma^1\gamma^2\gamma^3 = \begin{pmatrix} 0 & I \\ I & 0 \end{pmatrix}. \quad (1.4)$$

The Dirac-Pauli notation for γ^0 and γ^i is:

$$\gamma^0 = \begin{pmatrix} I & 0 \\ 0 & -I \end{pmatrix} \quad \text{and} \quad \gamma^i = \begin{pmatrix} 0 & \sigma^i \\ -\sigma^i & 0 \end{pmatrix}. \quad (1.5)$$

Here, I is the identity 2×2 -matrix and σ^i are the pauli matrices.

Now the chirality projection operators (1.3) are applying to arbitrary spinors u_L and u_R . Defining, as an example, a spinor $u^{(1)}(p)$ travelling along the z axis,

$$u^{(1)}(p_z) = N \begin{pmatrix} 1 \\ 0 \\ \frac{p_z}{E+m} \\ 0 \end{pmatrix}, \quad (1.6)$$

we get:

$$P_L u^{(1)}(p_z) = \frac{1}{2}(1 - \gamma^5)u^{(1)}(p_z) = \frac{1}{2}N \left(1 - \frac{p_z}{E+m}\right) \begin{pmatrix} 1 \\ 0 \\ -1 \\ 0 \end{pmatrix} \quad (1.7)$$

and

$$P_R u^{(1)}(p_z) = \frac{1}{2}(1 + \gamma^5)u^{(1)}(p_z) = \frac{1}{2}N \left(1 + \frac{p_z}{E+m}\right) \begin{pmatrix} 1 \\ 0 \\ 1 \\ 0 \end{pmatrix}. \quad (1.8)$$

For the ultra-relativistic limit ($E \gg m$, $E \approx p$) one can see that $P_L u^{(1)} \rightarrow 0$ and $P_R u^{(1)} \rightarrow u^{(1)}$.

1.3 Interaction & detection

Since neutrinos only interact via the weak force and gravitationally, their probability of interaction is very small. Depending on the neutrino flavor and interaction type, the cross-section at the energy of $E_\nu \approx 10$ MeV is about $10^{-40} - 10^{-44}$ cm⁻² [59]. In the case of high energy neutrinos, with $E_\nu > 100$ MeV, the kinetic energy of a neutrino is transferred into the creation of

other particles. For example, if one of these neutrinos interacts with a nucleus, various particles like pions and hadrons can form. These HE processes in combination with HE neutrino-lepton scattering are of interest for experiments like IceCube, which is researching cosmological HE neutrinos. More detailed HE neutrino interactions and detection can be found in Ref. [16]. The detection channels which liquid scintillator experiments, focus on are with neutrinos that have an $E_\nu \leq 100$ MeV. The next paragraphs will be about LE neutrino interactions, because these are of interest for JUNO and LENA. For low energies there are three types of interaction.

Inverse β -decay Free protons enable an electron neutrino to interact via the inverse β -decay (IBD). The reaction is as follows,

$$\bar{\nu}_e + p \longrightarrow e^+ + n . \quad (1.9)$$

Fortunately materials such as water and scintillator have many free protons and this detection channel is widely used in modern detectors. Also JUNO has the ability to utilize this. The energy threshold is $E_\nu \geq 1.8$ MeV [57]. What really makes this detection mode incredibly useful is the *delayed coincidence technique*, which can be used to tag the interaction and makes it possible to distinguish this interaction from background events. The positron annihilates in a timescale of nanoseconds, then about 250 μ s later the neutron gets captured. The capturing process has a probability of 99 % [12]. Upon capture γ -rays with a total energy of 4.9 MeV are emitted. To further enhance the neutron capture signal, the target material can be doped with gadolinium. This releases γ -rays with a total energy of 8 MeV. Because the cross-section of neutron capture by gadolinium is larger, the delay is reduced to about 30 μ s.

Elastic scattering This interaction has no energy threshold and works for any neutrino flavor. Therefore is especially useful to measure neutrino flavors other than electron neutrinos. This comes in handy when determining the solar neutrino flux or neutrinos from a supernova. The reaction for NC elastic scattering on an electron is,

$$\nu_i + e^- \longrightarrow \nu_i + e^- \quad \text{or} \quad \bar{\nu}_i + e^- \longrightarrow \bar{\nu}_i + e^- , \quad (1.10)$$

where i stands for any of the flavors e , μ or τ . A similar interaction is possible for elastic scattering on a proton, which the reaction is,

$$\nu_i + p \longrightarrow \nu_i + p \quad \text{or} \quad \bar{\nu}_i + p \longrightarrow \bar{\nu}_i + p , \quad (1.11)$$

Additionally a CC interaction is possible,

$$\nu_i + e^- \longrightarrow i^- + \nu_e . \quad (1.12)$$

This only works with electrons, since the neutrino energy is too small to create the corresponding lepton.

Even though there is no energy threshold the transferred energy of the neutrino to the scattering partner can be below the detector threshold. As an example, if it is a water cherenkov detector, the energy could be below the critical cherenkov energy threshold and no light could be produced.

Interactions with nuclei Another possibility for an interaction is neutrino capture by a nucleus. This CC interaction can be described by,

$$\nu_e + A_N^Z \longrightarrow e^- + A_{N-1}^{Z+1} \quad \text{or} \quad \bar{\nu}_e + A_N^Z \longrightarrow e^+ + A_{N+1}^{Z-1}, \quad (1.13)$$

with the nucleus A , that has Z protons and N neutrons. If the nucleus happens to decay shortly after and combining this with the prompt electron or positron signal, this interaction can be detected.

A NC interaction is the neutrino nucleus scattering. If this process leaves behind an excited nucleus, this can be detected, if it de-excites in a characteristic manner, with a detectable particle emission. On the other hand, if only recoil is generated, this is very low-energetic and has yet to be observed. The two interactions are as follows,

$$\nu_i + A_N^Z \longrightarrow \nu_i + A_N^{*Z} \quad \text{or} \quad \bar{\nu}_i + A_N^Z \longrightarrow \bar{\nu}_i + A_N^{*Z}, \quad (1.14)$$

$$\nu_i + A_N^Z \longrightarrow \nu_i + A_N^Z \quad \text{or} \quad \bar{\nu}_i + A_N^Z \longrightarrow \bar{\nu}_i + A_N^Z. \quad (1.15)$$

The A^* represents the excited nucleus state.

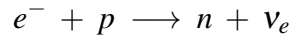
1.4 Origins of neutrinos

Neutrino research gives rise to many different subjects. Not only the characterisation of the particle is important, but also the examination of neutrino sources. They can give a deep insight into fundamental processes of the universe. In this section different neutrino origins and their implications will be discussed.

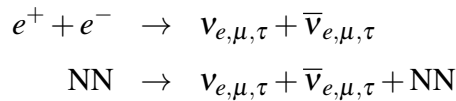
Core collapse supernova neutrinos The supernova (SN) type, which is being researched in today's neutrino physics, is the core collapse of a massive star at the end of its lifetime. This covers every type of SN except *thermonuclear* SN 1a. Core collapse SN are to be assumed from here on onwards. SN are one of the brightest phenomena in the universe, not only in the visible spectrum because they also have the brightest neutrino flux. In a tenth of a second about 10^{58} neutrinos and antineutrinos are emitted [31]. The visible light can outshine the light of the host galaxy for several weeks and some SNe can even be visible during daytime with the naked eye. Neutrinos are also the first signal that reaches us from a SN: Because they only interact

via the weak interaction, they can escape early. But even the neutrinos take about 10 s to reach the surface of the collapsing star, with about 10^9 bounces. Compared to the shock wave, which takes about 2 hours, this is still fast.

At the beginning of the core collapse neutrinos are created mostly by electron capture.



But these neutrinos are trapped, since the diffusion out of the core region matter takes longer than it takes the infalling matter to build up new areas to diffuse through. After nuclear matter density is reached, a shock front forms and traverses out through the infalling matter, to about 150 km [32]. It is stopped by thermal energy losses. A proto-neutron star is formed and is accumulating more matter. It mainly cools via ν_e emission. The so-called *prompt electron neutrino burst* comes from the rapid neutronization, about 50 km away from the center [32], around the proto-neutron star. This area gets heated up by the CC (re-)captures of ν_e and $\bar{\nu}_e$, so that it explosively ejects the star's shell. After this explosion the neutron star release gravitational binding energy through emission of all neutrino flavors. Produced by electron-positron annihilation and nucleon-nucleon (NN) bremsstrahlung.



99 % of the released energy is carried away by neutrinos and only 1 % is converted into kinetic energy and light. A more detailed explanation and neutrino reactions can be found in [32].

The exact progress of SN development is only understood to a certain extent. In the event of a SN the neutrinos measured by experiments like JUNO or LENA could very well bring new insight into this matter. In addition the formation of heavy nuclei in a SN could be studied. Furthermore, the neutrinos traverse high-density matter on their way to the surface of the star and are subject to the Mikheyev–Smirnov–Wolfenstein (MSW) matter effect, which could hold information on the neutrino MO. In the event of a close SN and therefore high rate of neutrino events even a new neutrino mass limit might be set. There also exists the prediction of *collective neutrino oscillation* during SN conditions and the resulting high neutrino flux [55], another phenomena which can only be studied with a SN.

The expected rate of SNe within our own galaxy is only 1-3 per century [55]. Because of this low rate it is vital to always take data. Also since neutrinos are the first signal from a SN, there are always several experiments on the watch for such an event. These are grouped together in the *supernova early warning system* (SNEWS) [58].

Diffuse supernova neutrino background Even though the SNEWS is constantly looking for SN events, it maybe possible to detect neutrinos from long passed SN. The existence of a *diffuse supernova neutrino background* (DSNB) is predicted. It is expected to yield a constant low flux

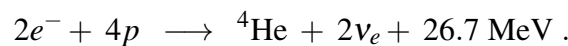
of SN neutrinos. The DSNB could not be measured so far.

The upper limit for DSNB currently is set by *Super Kamiokande* (SK). It resides at an energy of 13.3 MeV [74] for $E_{\bar{\nu}_e}$. Data of 960 days was taken and a *confidence level* (CL) of 90% was achieved. With more data it is expected to push this limit even lower down to 10 MeV. Furthermore the use of gadolinium tagging in SK was approved 2015 and higher sensitivity is to be expected.

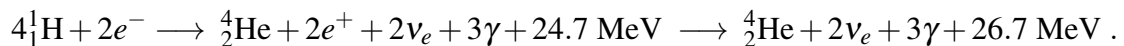
The rate of SN could be deduced from measuring the DSNB, but also it could advance SN models and help to clarify the idea of a standard SN. In general, significant statistics of DSNB neutrinos would provide information about the average SN, even without a SN in our own galaxy.

Solar neutrinos The sun produces about 3.8×10^{26} W of energy in the form of electromagnetic radiation [67]. The process freeing up this great amount of energy is fusion. Neutrinos are produced during this process. The energy of a photon takes more than 10^5 years to reach the surface of the sun [43]. On the other hand neutrinos mostly leave the sun without an interaction, which makes it possible to directly study the fusion process inside the sun. The flux of neutrinos from the sun is about $6.5 \times 10^{10} \text{ cm}^{-2} \text{ s}^{-1}$ [76]. The main fusion processes in the sun only produce ν_e , which limits the possible detection interactions, but also makes it easy to exclude these events if needed. They played an important role verifying the neutrino flavor oscillation.

The processes creating neutrinos through fusion are called proton-proton (pp) chain and carbon–nitrogen–oxygen (CNO) cycle. A diagram of the pp chain can be seen in figure 1.3a. The pp-chain accounts for the release of about 98.5 % of the energy. The overall energy production for this reaction is given by



The second mechanism is the CNO cycle, a diagram is shown in figure 1.3b. This cycle is also a fusion process, it uses carbon, nitrogen and oxygen as catalysts and releases ν_e during the process. Even though there are multiple parts, the overall net energy for all cycles is the same and can be given by



How well the catalyzation works, depends on the concentration of CNO elements and the temperature. One can study these factors with the neutrino flux from these processes. A defining part of this is the *metallicity* Z of the sun. It describes how much of the fraction of a star is not hydrogen X or helium Y . Core temperature and *metallicity* are part of the *standard solar model* (SSM). Depending on how well one can describe the sun with the SSM, also affects how one explains other star spectra. Therefore measuring the neutrinos from the CNO cycle is of the essence, to validate and adjust the SSM.

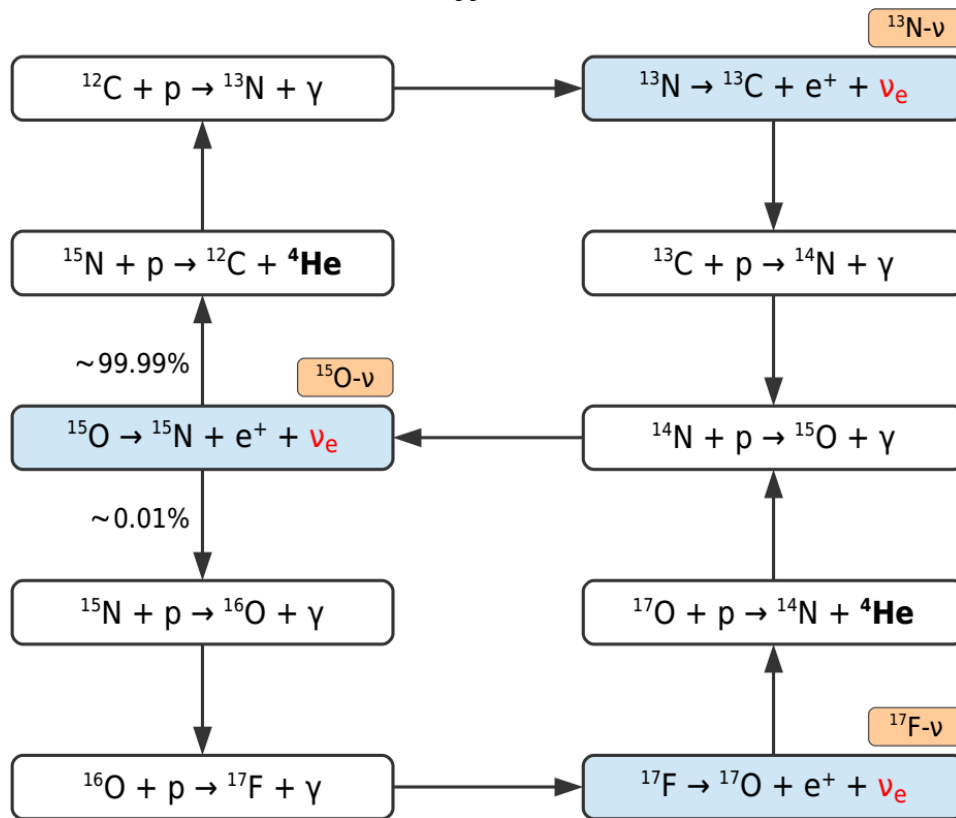
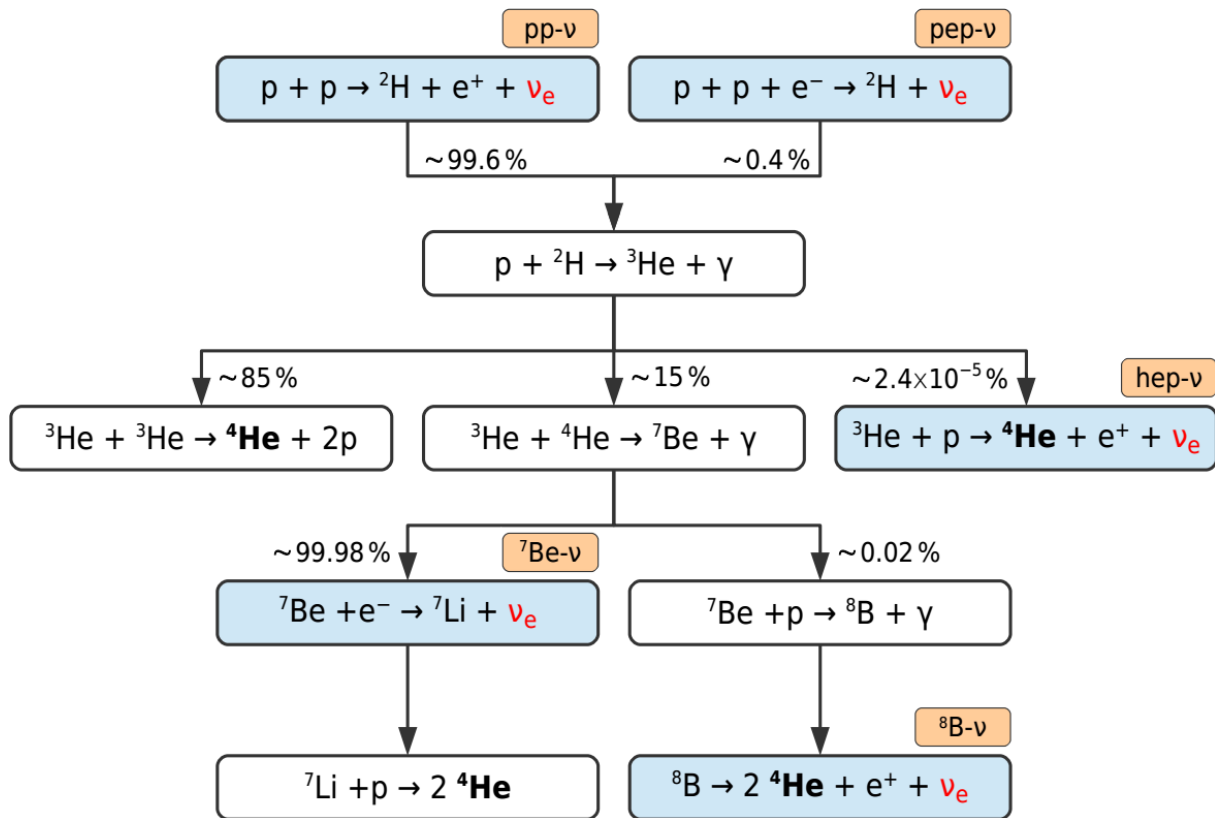


Figure 1.3: Diagram describing the fusion processes in the sun. (a) shows the *pp* chain directly combining two protons, hence its name. (b) shows the CNO cycles I and II, using CNO as catalysts. The parts of the processes releasing ν_e are marked in light blue. [40]

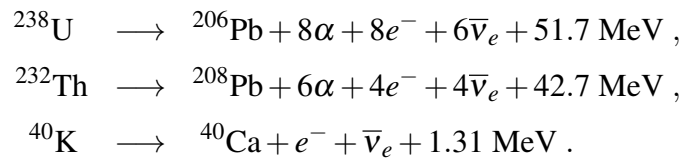
Atmospheric neutrinos The earth's atmosphere is constantly bombarded by cosmic rays. About 79 % of the incoming particles are protons and 14.7 % are helium nuclei. They can reach energies above 100 TeV, but their typical energy range is around a few GeV. Some of these will create showers of other particles in the upper atmosphere, including neutrinos and antineutrinos. A cascade of particle creation, annihilation and decay is formed. Depending on the energy, these particle showers can reach down to sea level. The neutrino and antineutrino creation mostly arises from decay processes of pions, kaons and muons. The probability of these decays to happen is given by the branching fraction (BF). A few of these decays are [50],

$$\begin{array}{lll}
\pi^+ \rightarrow \mu^+ + \nu_\mu, & \pi^- \rightarrow \mu^- + \bar{\nu}_\mu, & \text{BF: } \sim 99.99\%, \\
\pi^+ \rightarrow e^+ + \nu_e, & \pi^- \rightarrow e^- + \bar{\nu}_e, & \text{BF: } \sim 0.01\%, \\
K^+ \rightarrow \mu^+ + \nu_\mu, & K^- \rightarrow \mu^- + \bar{\nu}_\mu, & \text{BF: } \sim 64\%, \\
K^+ \rightarrow \pi^0 + e^+ + \nu_e, & K^- \rightarrow \pi^0 + e^- + \bar{\nu}_e, & \text{BF: } \sim 5.1\%, \\
K^+ \rightarrow \pi^0 + \mu^+ + \nu_\mu, & K^- \rightarrow \pi^0 + \mu^- + \bar{\nu}_\mu, & \text{BF: } \sim 3.4\%, \\
K_L^0 \rightarrow \pi^+ + e^- + \bar{\nu}_e, & K_L^0 \rightarrow \pi^- + e^+ + \nu_e, & \text{BF: } \sim 41\%, \\
K_L^0 \rightarrow \pi^+ + \mu^- + \bar{\nu}_\mu, & K_L^0 \rightarrow \pi^- + \mu^+ + \nu_\mu, & \text{BF: } \sim 27\%, \\
\mu^+ \rightarrow e^+ + \nu_e + \bar{\nu}_\mu, & \mu^- \rightarrow e^- + \bar{\nu}_e + \nu_\mu, & \text{BF: } \sim 100\%.
\end{array}$$

The flux of these neutrinos is hard to predict, because it depends on very varying factors. A challenging part is the constantly changing air density and condition, another part is the flux of incoming particles.

Atmospheric neutrinos are underlying the matter oscillations effects and future experiments will try to use this to determine neutrino MO [1]. Furthermore, there are hints that atmospheric neutrinos hold information about δ_{CP} and structure of the Earth could be deduced via atmospheric neutrino absorption [69]. This would be a great opportunity to verify more traditional methods like seismic tomography.

Geo-neutrinos Some neutrinos are naturally created on earth and originate from the β -decay of radioactive elements. The main elements producing these are ^{238}U , ^{232}Th and ^{40}K . The total reaction and energy release of the decay chains are,



Studying the $\bar{\nu}_e$ flux of about $10^6 \text{ cm}^{-2} \text{ s}^{-1}$ allows the measurement of the the distribution of radioactive elements in regions that could not be examined before. The crust and mantle¹ have

¹It is to note that samples from the upper mantle reach the surface through tectonic activity, and their composition may change because of the transportation.

been probed, but only geo-neutrinos can indicate information about the isotope composition of earth's core and lower mantle. When the composition of earth is determined this can be compared to extra terrestrial objects like comets and meteoroids and clarify the history of earth and the solar system. Already existing experiments like Borexino [5] and KamLAND [10] have examined geo-neutrinos, but measuring geo-neutrinos at different locations is still necessary, because one mainly probes the local abundance and only by combining results one can deduce the contributions of different layers to the total geo-neutrino flux.

Reactor neutrinos Another source of $\bar{\nu}_e$ is manmade. These also originate from β -decay of radioactive elements. These elements are subject to the fission process in nuclear reactors. The elements that account for 99.5 % of the fission process are ^{235}U , ^{238}U , ^{239}Pu and ^{241}Pu [34]. Reactors represent an adjustable neutrino source with relatively precise location and flux. A reactor approximately generates a $\bar{\nu}_e$ flux of about $2 \times 10^{20} \text{s}^{-1}$ per GW thermal power, in an isotropic manner [34].

Reactor neutrinos have been used to verify the existence of neutrinos and are still used in experiments today. Oscillation experiments measure neutrino mixing angles, e.g. Θ_{13} through disappearance of $\bar{\nu}_e$. Experiments that examined $\bar{\nu}_e$ are CHOOZ, DAYA BAY and RENO [15, 47, 61]. Furthermore, experiments like JUNO and RENO-50 will look into the oscillation fine structure to determine the neutrino MO. However, there are still two problems with the neutrino flux from reactors. The first is the *reactor antineutrino anomaly*, a 3 % higher flux and disappearance of 6 % more $\bar{\nu}_e$ than expected, which could be explained with a fourth neutrino generation. The second is a neutrino excess at around 5 MeV in the reactor antineutrino flux spectrum. These could be the result of failing to theoretically describe the reactor antineutrino flux, nevertheless further investigation is of the essence.

Neutrino beams Some experiments require a directed stream of neutrinos that were created at a certain distance. For these purposes, neutrino beams play an important role. The neutrinos are created from the decay of unstable particles, like mesons. Examples for these decays have been given in the section 1.4 about the same decays, where they happen in an uncontrolled manner. For neutrino beams, the mesons can be created with protons being accelerated into a target. This will create pions and kaons. Since focusing neutral charged particles like neutrinos is impossible, the charged particles, which will decay into the neutrinos, are focused instead. After that, these particles go along a decay tube and particles that did not decay are stopped by a hadron stop. Muons can not be completely stopped that way, but since they can be used to test the alignment of the beam with the experiment, it is also not wanted to stop those. Varying the length of decay tube allows different compositions of neutrino beams, because different mesons have different decay times. This also implies that a neutrino beam will always be to a certain degree contaminated with neutrino flavors that are not wanted for an experiment.

Experiments that use neutrino beams investigate neutrino oscillation. As an example, OPERA has excluded the absence of ν_μ to ν_τ oscillation at a level of 5.1σ [2].

1.5 Neutrino physics today

Neutrino physics is an ongoing field of research. Many questions have been addressed, but some open questions remain to be solved. Just recently, the Nobel Prize in Physics 2015 was awarded jointly to Takaaki Kajita and Arthur B. McDonald "for the discovery of neutrino oscillations, which shows that neutrinos have mass" [24]. The experimental proof of neutrino flavor oscillation represents a major milestone for particle physics. Its a great illustration that the SM is incomplete. Even though the debate of neutrinos changing flavor was a topic, since the neutrino was discovered, it took until 1998, when the Super-Kamiokande (SK) Collaboration presented convincing data, validating the neutrino oscillation discovery [24]. Then 2001/2002 the Sudbury Neutrino Observatory (SNO) Collaboration confirmed neutrino oscillation with their findings. The JUNO collaboration will utilize neutrino oscillation to determine the neutrino mass ordering (MO). Therefore, the next two subsections are about neutrino flavor oscillation and neutrino MO, followed by a commentary on other open questions in neutrino physics.

1.5.1 Neutrino flavor oscillation

In Vacuum In the following, the development of time dependent neutrino flavor transition probability from the general case of n arbitrary orthonormal Eigenstates in vacuum is shown. Let the flavor eigenstates $|\nu_\alpha\rangle$ be connected with the mass eigenvalues $|\nu_i\rangle$ through the unitary mixing matrix U in the following way:

$$|\nu_\alpha\rangle = \sum_i U_{\alpha i} |\nu_i\rangle, \quad (1.16)$$

where $|\nu_i\rangle = \sum_\alpha U_{\alpha i}^* |\nu_\alpha\rangle$ and for a finite number of n flavor eigenstates $\langle \nu_\beta | \nu_\alpha \rangle = \delta_{\alpha\beta}$ and mass eigenstates $\langle \nu_j | \nu_i \rangle = \delta_{ij}$ be defined.

Also because U is unitary,

$$U^+ U = 1, \text{ therefore } \sum_i U_{\alpha i} U_{\beta i}^* = \delta_{\alpha\beta}, \quad \sum_i U_{\alpha i} U_{\beta j}^* = \delta_{ij}. \quad (1.17)$$

The next step is using the time dependency of mass eigenstates $|\nu_i\rangle$:

$$|\nu_i(t)\rangle = e^{-iE_i t} |\nu_i\rangle. \quad (1.18)$$

Applying the time dependency (1.18) to the flavor eigenstate (1.16), one obtains:

$$|\nu(t)\rangle = \sum_i U_{\alpha i} e^{-iE_i t} |\nu_i\rangle. \quad (1.19)$$

This represents the time-development of a flavor eigenstate, which started pure at a time $t = 0$.

The time dependent transition amplitude then is given by

$$A(\alpha \rightarrow \beta; t) \equiv \langle \nu_\beta | \nu(t) \rangle = \sum_i U_{\alpha i} U_{\beta i}^* e^{-iE_i t} . \quad (1.20)$$

For the next step the energy-momentum relation is needed:

$$E_i = \sqrt{p^2 + m_i^2} \approx p + \frac{m_i^2}{2p} \approx E + \frac{m_i^2}{2E} . \quad (1.21)$$

Inserting equation (1.21), which is only allowed for $p \gg m_i$ and $E \approx p$, into transition amplitude (1.20) and using natural units ($\hbar = c = 1$) gives:

$$A(\alpha \rightarrow \beta; t) = \sum_i U_{\alpha i} U_{\beta i}^* \exp\left(-i \frac{m_i^2}{2E} L\right) = A(\alpha \rightarrow \beta; L) , \quad (1.22)$$

with $L = t$ being the distance from the ν_α neutrino source to the detector, where ν_β is detected. The neutrino flavor survival probability can be calculated from the transition amplitude (1.20) by:

$$\begin{aligned} P(\alpha \rightarrow \beta; t) &= |A(\alpha \rightarrow \beta; t)|^2 \\ &= \sum_{i,j} U_{\alpha i} U_{\alpha j}^* U_{\beta i}^* U_{\beta j} e^{-i(E_i - E_j)t} \\ &= \sum_i |U_{\alpha i} U_{\beta i}^*|^2 + 2\text{Re} \sum_{j>i} U_{\alpha i} U_{\alpha j}^* U_{\beta i}^* U_{\beta j} \exp\left(-i \frac{\Delta m_{ij}^2}{2E} L\right) \end{aligned} \quad (1.23)$$

As one can see from equation (1.23), the neutrino flavor oscillation is only sensitive to Δm_{ij}^2 . Therefore, the absolute neutrino masses can not be determined. Assuming CP invariance, the neutrino flavor survival probability (1.23) can be further simplified to:

$$P(\alpha \rightarrow \beta; t) = \delta_{\alpha\beta} - 4 \sum_{j>i} U_{\alpha i} U_{\alpha j} U_{\beta i} U_{\beta j} \sin^2\left(-i \frac{\Delta m_{ij}^2}{4E} L\right) \quad (1.24)$$

For the realization of three neutrino flavors the unitary matrix U becomes a 3×3 matrix, also called Pontecorvo–Maki–Nakagawa–Sakata (PMNS) matrix. A possible factorization of this matrix is given as:

$$U_{PMNS} = \begin{pmatrix} 1 & 0 & 0 \\ 0 & c_{23} & s_{23} \\ 0 & -s_{23} & c_{23} \end{pmatrix} \begin{pmatrix} c_{13} & 0 & s_{13} e^{-i\delta_{CP}} \\ 0 & 1 & 0 \\ -s_{13} e^{i\delta_{CP}} & 0 & c_{13} \end{pmatrix} \begin{pmatrix} c_{12} & s_{12} & 0 \\ -s_{12} & c_{12} & 0 \\ 0 & 0 & 1 \end{pmatrix} , \quad (1.25)$$

where $c_{ij} = \cos(\Theta_{ij})$, $s_{ij} = \sin(\Theta_{ij})$ and δ is the CP violating phase.

Since neutrino flavor oscillation exists, this leaves us with the discovery that neutrinos must have non-zero rest masses and mixing between neutrino flavors is possible. Also the eigenstates

can not have the same eigenvalues.

In matter Neutrino flavor oscillation also happens while a neutrino is traversing matter. The Mikheyev–Smirnov–Wolfenstein (MSW) effect describes the changes in neutrino flavor oscillation. Matter affects the neutrino because electrons and nucleons are around, which are prone for interaction. Especially the *coherent elastic forward scattering* contributes to the changes in oscillation. All flavors can scatter elastically with electrons via Z^0 , but only ν_e and $\bar{\nu}_e$ can via W^- . Therefore the *neutral current* (NC) scattering interactions cancel out, with the exception of ν_e and $\bar{\nu}_e$.

The MSW effect is important for the description of neutrino oscillation inside the sun and when neutrinos traverse the earth. Especially it was needed to unravel the solar neutrino problem. Also it was utilized to discuss a possible day-night effect of solar neutrinos flavor oscillation. Considering the difference in matter passed for solar neutrinos going through earth, to be detected on the night hemisphere.

1.5.2 Neutrino mass ordering

As established in section 1.5.1, the neutrino oscillation is only sensitive to the squared mass differences of the neutrino flavors. The absolute neutrino masses are unknown, but also the mass ordering (MO) is not resolved yet. The sign of the third neutrino mass state could not be determined so far. It involves $|\Delta m_{32}^2|$ and $|\Delta m_{31}^2|$. Therefore two possible orderings of the neutrino masses are possible. Either the normal ordering (NO), with $m_1 < m_2 < m_3$, is realized or the inverted ordering (IO), with $m_3 < m_1 < m_2$, is true. The best-fit parameters and their errors for the squared masses and mixing angles are stated in table 1.1, taken from Ref. [28]. A diagram

Table 1.1: A best-fit result from Ref. [28], for the squared masses and mixing angles. (1σ uncertainties and 3σ confidence level)

	$\Theta_{12} [^\circ]$	$\Theta_{13} [^\circ]$	$\Theta_{23} [^\circ]$	$\delta [^\circ]$	$\Delta m_{\text{sol}}^2 [\text{eV}^2]$	$\Delta m_{\text{atm}}^2 [\text{eV}^2]$
NO	$33.48^{+0.78}_{-0.75}$	$8.50^{+0.20}_{-0.21}$	$42.3^{+3.0}_{-1.6}$	306^{+39}_{-70}	$7.50^{+0.19}_{-0.17} \cdot 10^{-5}$	$2.457^{+0.047}_{-0.047} \cdot 10^{-3}$
IO	$33.48^{+0.78}_{-0.75}$	$8.51^{+0.20}_{-0.21}$	$49.5^{+1.5}_{-2.2}$	254^{+63}_{-62}	$7.50^{+0.19}_{-0.17} \cdot 10^{-5}$	$2.449^{+0.048}_{-0.047} \cdot 10^{-3}$

for the possible realizations of MO is given in figure 1.4. Θ_{12} and Δm_{21}^2 are known as *solar parameters* and Θ_{23} and Δm_{32}^2 (or Δm_{31}^2) are commonly names as *atmospheric parameters*. They can and have been measured using these neutrino sources and therefore U_{PMNS} is parametrized in a way to represent this.

Determining the neutrino MO and searching for leptonic CP-violation are top tasks in modern physics. Great efforts are being made to advance on these subjects. Especially for the MO

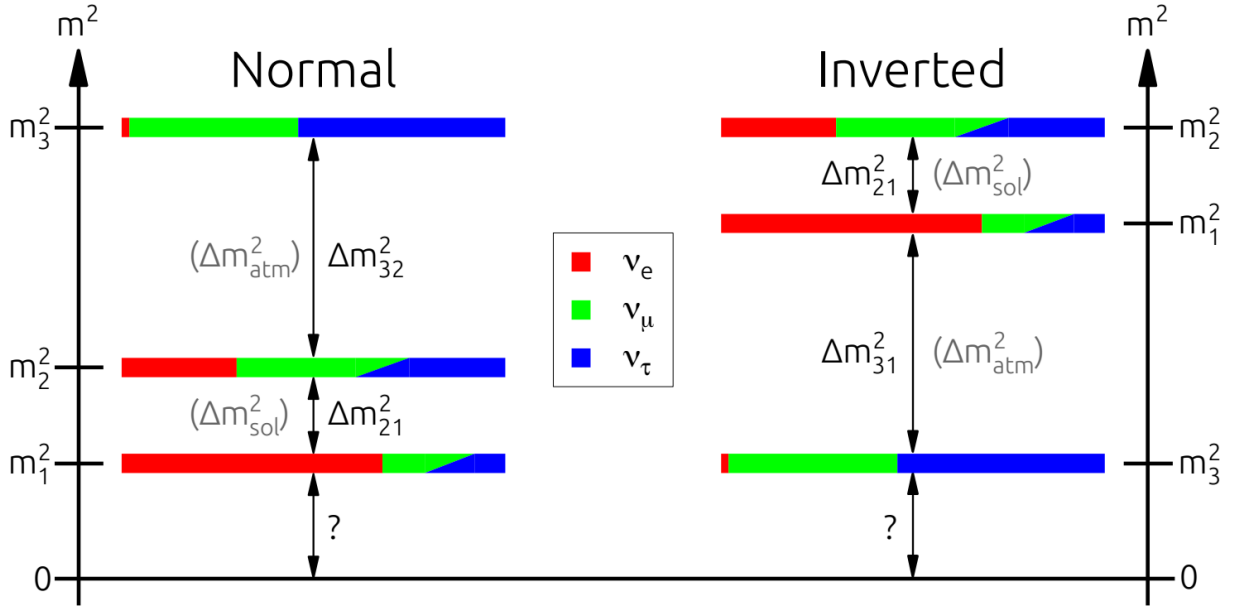


Figure 1.4: Resulting from the indeterminate neutrino flavor mass ordering, a diagram showing the possible realisation for NO (left) and IO (right). Represented by the horizontal colouring is the proportional part of mixture for the different flavors at that mass state. The diagonal division between ν_μ and ν_τ shows the uncertainty from the unknown phase δ_{CP} . The best-fit parameters from table 1.1 have been used to generate these flavor contents. [40]

multiple projects have been suggested and some have been approved. A suggested one is LENA which has the possibility to determine MO with long baseline neutrino oscillation [40]. An experiment that will be build and is under development right now is JUNO. It will investigate the flux of $\bar{\nu}_e$ from reactors with an unprecedented energy resolution and will be able to determine neutrino MO with 3σ , within six years of data taking [7].

1.5.3 Open questions

Some open questions apart from neutrino mass ordering and oscillation remain. Today's major research topics in neutrino physics are the possible CP violation and the neutrino mass, but also whether the neutrino could be its own antiparticle and the existence of sterile neutrinos. A short commentary will be given in the next three paragraphs.

Absolute neutrino mass Apart from the unknown neutrino MO, the absolute neutrino masses are a point of discussion. The findings of Ref. [51] represent the sum of neutrino masses to be $\sum m_\nu < 0.12$ eV with in 95 % CL. This result was obtained fitting Ly α -forest power spectrum data to cosmological parameters and combining these with data from the *cosmic microwave background* (CMB). These findings remain yet to be confirmed by experiments not only derived from cosmological parameters.

An upper limit for the electron neutrino mass has been establisher by precisely measuring the

β^- decay spectrum. *Troitsk* [11] has set the upper limit $m(\nu_e)$ to < 2.1 eV at 95 % CL. The upcoming experiment *Karlsruhe Tritium Neutrino Experiment* (KATRIN) [8] is estimated to be sensitive to $m(\nu_e) \sim 0.2$ eV at 90 % CL.

Experiments researching the $0\nu\beta\beta$ -decay are also sensitive to the effective Majorana ν_e mass m_{ee} , but will be challenged by great uncertainties, especially due to nuclear physics. The sensitivity limit for current experiments is 0.1 eV for m_{ee} and probably will half in future experiments [17].

Dirac or majorana It is possible that the neutrino is its own antiparticle. Leptons in the SM of particle physics are *Dirac fermions*, but the neutrino could be a *Majorana fermion*. A promising method to determine this is given by the $0\nu\beta\beta$ -decay [50]. If the decay is proven to exist, it becomes mandatory, that the neutrino is a *Majorana* particle. Because otherwise this process would violate lepton number conservation.

There are several experiments looking for the $0\nu\beta\beta$ -decay. So far there have been claims of a signal (See Ref. [35]), but no signal was seen by the *Germanium Detector Array* (GERDA) [4]. The experiments could set lower limits for the half-life of $0\nu\beta\beta$ -decay. The combined half-life limit of $0\nu\beta\beta$ -decay for ^{76}Ge yields $T_{1/2}^{0\nu} > 3.0 \times 10^{25}$ yr.

Sterile neutrinos At the current state of research there are some anomalies, that could very well be explained utilizing sterile neutrinos. Either by challenging the unitarity of the PMNS matrix and adding more generations of neutrinos or by adding right-chiral counterparts to existing neutrinos.

Unexpected results in several experiments, with up to 3σ confidence, give rise to the assumption of sterile neutrinos. Most commonly known is the *reactor antineutrino anomaly* [42], a 3 % higher flux and disappearance of 6 % more $\bar{\nu}_e$ than expected. The *Gallium Anomaly* also experiences some flux discrepancies. Ref. [27] describes a deficit found by comparing the flux of high intense radio active calibration source with the expected values.

JUNO may be able to shed some light at the issue, since it will determine the solar mixing parameters at a very precise level, which will improve the testing of three flavor neutrino oscillation.

Chapter 2

Large liquid scintillator detectors

A new generation of liquid scintillator detectors will be build in the near future. These large unsegmented detectors will open new opportunities for research beyond the standard model. Examples for the current Liquid scintillator detectors generation are Borexino and KamLand. These smaller unsegmented LS detectors have proven the feasibility and necessity of new large volume projects like LENA and JUNO. They already measured geo-neutrinos, Δm_{21}^2 and other neutrino parameters. But in order to get higher statistics, lower errors and to solve other outstanding issues in neutrino physics, liquid scintillator detectors with significantly higher target masses are of the essence.

Liquid scintillator detector today are the perfect tool to do low energy electron- and anti-electron-neutrino physics, as well as neutrinos up to several MeV. Furthermore they are highly qualified to perform spectral measurements, due to their high energy resolution and almost no existent energy threshold.

The general geometry of a large liquid scintillator detector normally consists of a scintillation volume surrounded by a light detecting component. Of cause the scintillator needs to be contained in a tank, to prevent leaking and contamination. The light detecting component generally is PMTs, though silicon based light detectors are on the rise. If one aims to do neutrino physics with such a detector, it also needs to be shielded against backgrounds. Hence it is generally located underground and has a surrounding veto volume.

Its not easy to reach the anticipated physics potential. One of the main reasons for this is the backgrounds, which are summarized in this paragraph. In order to do neutrino physics the detector has to be build in a way that ensures the possibility of measuring neutrino events and its corresponding parameters. Therefore the backgrounds have to be as low as possible. They can be classified in accidental-, cosmogenic-, intrinsic- and neutrino-background. Accidental-background happens when a random coincident signal is falsely mistaken for a real signal. Cosmogenic-background comes from Cosmic rays inducing HE events in the atmosphere, this produces for example HE muons which can pass through the detector. This is also the main reason why the detector should be underground. It will reduce the muon flux a lot. Intrinsic-background originates from radioactive nuclei, which come from contaminated surfaces or are embedded inside the detector components. Neutrino-background are neutrino events which do

not origin from the neutrino events that are researched for the performed analysis. It is not possible to shield against this, especially not in a neutrino experiment.

A general event evolution in a liquid scintillator detector is described now for comprehensibility, in this paragraph. On the verge of an event the particle interaction takes place at the vertex. For simplicity it is assumed to be inside the detector, though an interaction could also arise outside the detector with a part of the track leaking into the detector. The involved particles then initiate the scintillation, which will be covered in subsection 2.1.1. The PMTs detect the light and their respective times of arrival. Finally the readout electronics transmit the signal to a computer to reconstruct the event.

2.1 Light in a liquid scintillator detector

Following the journey of the light will highlight the operating principle of the detector. In the following sections different stages of the process will be further discussed.

2.1.1 Light emission

The main light source in liquid scintillator is the scintillation, hence scintillation will be further conducted in the next paragraph. But there is also another source, the cherenkov light. It will be summarized in a paragraph afterwards.

Scintillation light The process of scintillation is subsequently the property of luminescence. To initiate a luminescent process energy is transferred to the scintillation material and a characteristic spectrum is emitted. The energy transfer can happen in many different ways. For example through chemical reactions, mechanical stress or radiation. Luminescence can be further categorized into fluorescence with τ being about $10^{-9} - 10^{-8}$ seconds and phosphorescence $\tau \gtrsim 10^{-4}$ seconds [13]. Two important properties for a scintillating material to be used in a detector, are energy deposition and emission time τ . The energy deposition determines the light yield and the time τ specifies spacial resolution. As a rule of thumb, the higher the energy deposition the more light will be emitted. And the shorter the mean emission time, the better the spacial resolution will be.

As established before, the emission of scintillation light, precedes an excitation of an electron. The excitation through charged particles is the one of interest for a detector. The deexcitation then emits a photon in a random direction in a corresponding wavelength. Hence the scintillation light is emitted isotropically with a scintillator specific spectrum. Deexcitation of an electron in the scintillator happens after a random time interval and the probability is give by a decay function. The rate of decay is proportional to the number of electrons that are excited. Under the assumption of no rise time for a pulse, the pulse can be described by a weighted sum of exponential decay functions. Hence, the photon emission time t with n decay components is

described by the probability density function (p.d.f.) $\Phi_{em}(t, \tau, \omega)$ (2.1).

$$\Phi_{em}(t, \tau, \omega) = \sum_{i=1}^n \frac{\omega_i}{\tau_i} e^{-\frac{t-t_0}{\tau_i}}, \quad t \geq t_0, \quad \sum_{i=1}^n \omega_i = 1 \quad (2.1)$$

τ_i is the mean lifetime of component i and ω_i the corresponding weight. Energy deposition and population of electron states change depending on the particle and on the combinations of τ and ω . One can use this effect to discriminate different particles by pulse shape [56].

Light yield depends on the energy deposition dE/dx and the scintillator it self. The energy deposition dE/dx can be described by the *Bethe-Bloch-equation* (2.2). This is valid for charged particles heavier than electrons and $0.1 \lesssim \beta\gamma \lesssim 1000$. Outside of that, radiative corrections have to be used [50]. See table 2.1 for the used variables.

$$\left\langle -\frac{dE}{dx} \right\rangle = K z^2 \frac{Z}{A} \frac{1}{\beta^2} \left[\frac{1}{2} \ln \frac{2m_e c^2 \beta^2 \gamma^2 W_{max}}{I^2} - \beta^2 - \frac{\delta(\beta\gamma)}{2} \right] \quad (2.2)$$

$$W_{max} = \frac{2m_e c^2 \beta^2 \gamma^2}{1 + 2\gamma m_e/M + (m_e/M)^2}$$

Table 2.1: This table holds the variables used in the *Bethe-Bloch-equation* (2.2). [52]

Symbol	Definition	Value or (usual) units
A	atomic mass of absorber	g mol^{-1}
β	v/c	
$\delta(\beta\gamma)$	density effect correction to ionization energy loss	
γ	Lorentz factor	
I	mean excitation energy	eV
K	$4\pi N_A r_e^2 m_e c^2$	$0.307\,075 \text{ MeV mol}^{-1} \text{ cm}^2$
M	incident particle mass	MeV/c^2
$m_e c^2$	electron mass $\times c^2$	$0.510\,998\,928(11) \text{ MeV}$
N_A	Avogadro's number	$6.02214129(27) \times 10^{23} \text{ mol}^{-1}$
r_e	classical electron radius	$e^2/4\pi\epsilon_0 m_e c^2 = 2.817\,940\,3267(27) \text{ fm}$
W	energy transfer to an electron in a single collision	MeV
z	charge number of incident particle	
Z	atomic number of absorber	

The response of organic scintillator is not linear, because quenching effects can reduce the luminescence. As an example for reduced luminescence, protons and α -particles create high ionizations along their track and ionized scintillator molecules can not participate in the scintillation process. An empirical model to describe the luminescence per unit length $d\mathcal{L}/dx$ is given by the *Birks' Law*. Stated in equation (2.3).

$$\frac{d\mathcal{L}}{dx} = \mathcal{L}_0 \frac{\frac{dE}{dx}}{1 + kB \frac{dE}{dx}} \quad (2.3)$$

Birks' constant kB is material dependent and must be measured. For example kB in LAB is about $0.009 \text{ cm MeV}^{-1}$ [65]. In general $\sim 3\%$ of the deposited energy is transformed into optical photons [50].

There is a wide range of scintillating materials, they can be gaseous, liquid or solid. Also there are organic and inorganic compounds. Organic scintillators often have aromatic rings where the excitations take place. Inorganic scintillators are normally crystals where excitation takes place within the crystals band structure.

The base scintillation compound which was planned to be used in LENA and will be used in JUNO, is *linear alkylbenzene* (LAB, $C_{18}H_{30}$), a liquid organic scintillator. LAB has a high light yield, optical transparency and low radioactive contamination. Also it has a high flash point, is cheap and has no concerns for the environment or human health. LAB as the scintillator will be assumed from here onwards.

Cherenkov light When a charged particle passes through a dielectric material, with a speed greater than the material speed of light, then cherenkov light is emitted. The charge of that passing particle polarizes the material and because of its great velocity it distorts the local electric field. Breaking the sound barrier is a comparable effect. The distortion transfers polarization energy, which is release in the form of electromagnetic waves. This effect contributes to the energy deposition per unit length dE/dx , but it is negligible since the contribution is only about $\sim 10^{-3} \text{ MeV cm}^2\text{g}^{-1}$ [37].

Cherenkov radiation is emitted under a specific angle, called the cherenkov angle Θ_c . The cherenkov angle is given by equation (2.4).

$$\Theta_c = \arccos \frac{1}{\beta n(\epsilon)} \quad (2.4)$$

$n(\epsilon)$ is the refractive index, depending on the energy of the associated photon wave package. This implies a threshold of $\beta = 1/n(\epsilon)$. Because of Θ_c it is emitted in a cone shape. A schematic of the cherenkov wavefront can be seen in figure 2.1. Additionally the cherenkov light is also linear polarized. In the direction perpendicular to the particle trajectory.

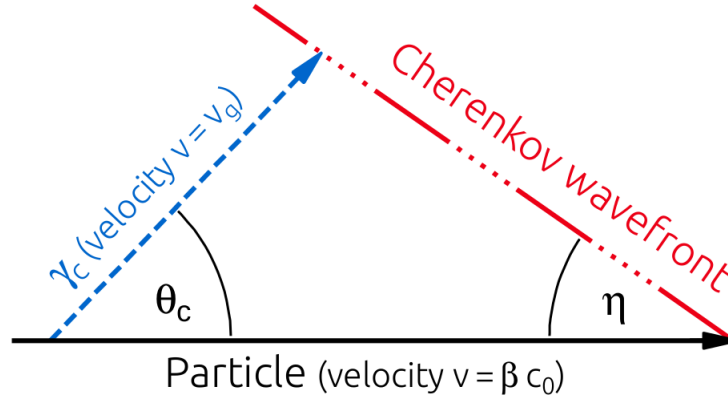


Figure 2.1: This schematic shows the cherenkov wavefront, with a photon γ_c emitted under the cherenkov angle Θ_c . The particle direction (black) is shown by the lower vector. The wavefront forms a cone, with an opening angle of η . [40]

Cherenkov radiation light yield, as number of emitted photons N per unit length x and $d\varepsilon$, is given by the *Frank-Tamm-formula* (2.5).

$$\frac{d^2N}{d\varepsilon dx} = \frac{\alpha z^2}{\hbar c} \sin^2 \Theta_c(\varepsilon) \quad (2.5)$$

With α being the fine structure constant. Compared to the light yield of liquid scintillator, cherenkov radiation only makes up for a small part of the emitted light. About 7% of the detected light was found to be cherenkov light in a simulation of JUNO for a HE muon event. Nevertheless it still holds some useful information, e.g. directional and time information, which theoretically could be deduced with a topological reconstruction approach.

2.1.2 Light propagation

Once light is created it holds information which is needed if one tries to resolve the course of events. Detecting photons is enough to get an idea of the deposited energy. But the timing information of photons can be used to determine the time and position of an event. By using the photon speed it is possible to get the time of flight (TOF), an important concept in reconstructions. The speed of a photon in a medium is given by the group velocity v_g . But a photon passing through material holds the possibility of absorption or scattering. This can distort or erase the information of that photon. Processes like this are *Rayleigh scattering* and *Mie scattering*, as well as absorption by molecules. These effects reduce the information on time and localization. Furthermore absorption and subsequent conversion to heat energy reduces the event energy resolution. To describe the probability of a photon to undergo such an information reduction, formula (2.6) can be used.

$$\Phi_{att}(x, L) = \frac{1}{L} e^{-x/L} \quad (2.6)$$

L is the attenuation length, which can be further broken down into formula (2.7).

$$\frac{1}{L} = \frac{1}{l_A} + \frac{1}{l_S} \quad (2.7)$$

l_A is the characteristic absorption length and l_S the characteristic scattering length. Since there are multiple scattering mechanisms it can be split into formula (2.8).

$$\frac{1}{l_S} = \frac{1}{l_{are}} + \frac{1}{l_{ray}} + \frac{1}{l_{mie}} \quad (2.8)$$

In this formula, l_{are} is the part of the absorption with subsequent re-emission. *Rayleigh scattering* and *Mie scattering* make up the other parts.

To enhance the transparency the attenuation length L needs to be maximized. This is done by maximizing the contributors. *Rayleigh scattering* is an intrinsic feature, from the bound electrons of the scintillator and can only be changed by changing the scintillator. *Mie scattering* on the other hand comes from impurities in the solvent. A clean scintillator is the key. But it is to consider that also pure scintillator would not work well, because the spectrum that is emitted by the luminescent process is also the spectrum that the scintillator absorbs. So a wavelength shifting component is mixed into the scintillator to reduce absorption. An achievable attenuation length is ~ 20 m. To further increase attenuation length the possibilities of water based liquid scintillators are investigated [72]. Even though the light yield is drastically lower than the light yield of full scintillator mixtures, the raised attenuation length of up to ~ 100 m can contribute to a much larger detector target volume. Choosing the scintillator mixture effectively limits the size of the detector.

2.1.3 Light detection

To gain information about an event the photons need to be detected. The standard way for liquid scintillator based detectors is the use of *photomultiplier tubes* (PMT). There also are novel ways possible, by using Large-Area Picosecond Photo-Detectors (LAPPD) or silicon based detectors more commonly known as *Silicon strip detectors* (SSD).

Photomultiplier tube The commonly used technology to detect light, when a large detector surface needs optical coverage, is the PMT. It holds the possibility to have single photon detection and still a big surface for a reasonable price. Commonly a PMT consists of a glass body, which contains all components. The inside of the front is coated with the photocathode layer. The dynodes which are responsible for multiplication process are located in the back. In front of them is a focusing electrode. The back of the PMT is sealed and has only the connectors sticking out. Everything else inside the glass body is normally vacuum. The photoelectric effect can transform a photon signal into an electric one. A single electron is enough to start a chain reaction of multiplication, through a geometric configuration of dynodes. A scheme can be seen in figure 2.2.

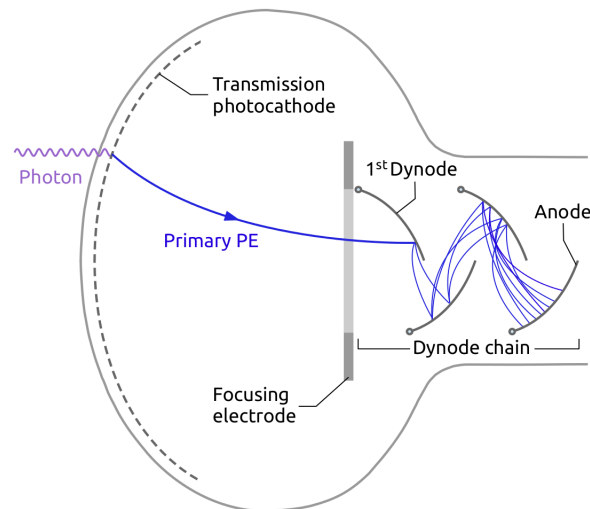


Figure 2.2: A scheme of a common PMT layout is shown, with a possible trajectory for a photon to be translated into a signal. The photon (purple) hits out a electron (blue) via photoelectric effect. That electron is then accelerated on to the first dynode where it hits out other electron. This repeats in the dynode chain. [40]

But because one electron can be enough to start an avalanche, this also implies any electron that did not take the path described by figure 2.2, creates an unwanted signal. Other signal origins can be seen in figure 2.3. An electron which has its origin from elastic scattering at the first dynode for example, can create a pre-pulse. On the other hand, an after-pulse could be created by an electron which is from the photocathode transmission layer, but was knocked out by a positively charged ion, that it self could have been created by a passing electron inside the PMT. Also the possibility of so called *dark current* exists, which happens when an electron is released due to thermal evaporation. These effects increase with higher voltage and temperature of the electrodes. Processes like these can distort the signal a PMT is giving.

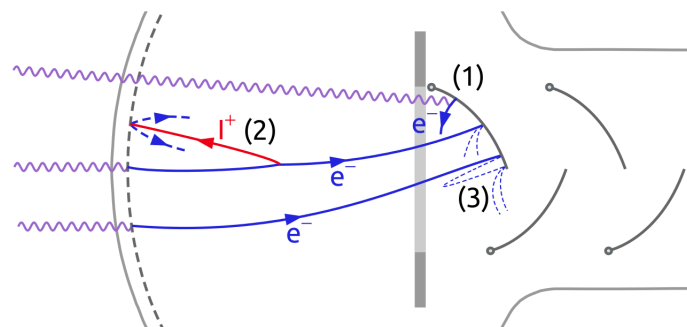


Figure 2.3: The figure shows different possibilities for the creation of pre- and after-pulses. (1) A photon passes the photocathode layer without transformation and knocks out an electron on the first dynode, resulting in a pre-pulse. (2) An ion I^+ created inside the PMT, from a passing electron, drifts towards the photocathode. Knocked out electrons create an after-pulse. (3) Additional electrons get knocked out at the first dynode, by a photo electron, also holding the possibility of after-pulse creation. [40]

The time it takes for a photon to be translated into a signal, is described by the *transit time* T . The *average transit time* \bar{T} in combination with a fluctuation δT , makes up $T = \bar{T} + \delta T$. δT commonly is described by an asymmetric statistical distribution $\Phi_{\delta T}$, which is characterized by the *transit time spread* (TTS) ΔT . \bar{T} and ΔT depend on the geometry of the PMT and as a rule of thumb with larger geometry these increase as well.

Using the photoelectric effect also implies that not all photons are translated into an electrons. This limits the effectiveness of a PMT and is described by the *quantum efficiency* (QE) η_{PMT} . The number of electrons N_e per incident photon $N_\gamma(\varepsilon, x)$ describes the ratio of a photon being converted into an electron, which is stated in equation (2.9).

$$\eta_{\text{PMT}} = \frac{N_e}{N_\gamma(\varepsilon, x)} \quad (2.9)$$

This property depends on the energy ε of the incident photon and the material chosen as photocathode. Therefore the material should be suitable for the emitted liquid scintillator spectrum.

For event energy reconstruction the optical coverage is important. To further increase the effective PMT surface, one can add light concentrators. It can be a cone, centred around the PMT-axis, with a parabola shape. The reflective inner surface funnels the photons on to the PMT. This is commonly known as a *Winston-cone*. This can reduce the amount of PMTs needed for the same optical coverage. But even though the effective PMT surface increases, the angle acceptance will be lower than before and the *average transit time* \bar{T} will increase. It is exposed when photons arrive, with an incident angle, lower than a critical angle. Then the photon is not reflected onto the PMT, but instead reflected onto the other side of the *Winston-cone* and then reflected out of the light concentrator. A scheme can be seen in figure 2.4.

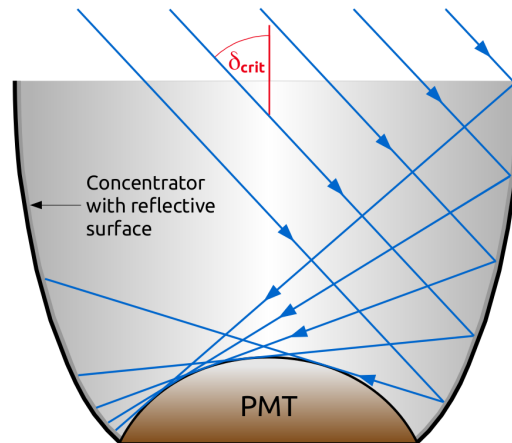


Figure 2.4: In the figure a PMT with light concentrator is shown and photons (blue) entering at the critical angle δ_{crit} . The concentrator has a reflective inner surface. Photons get reflected of it and do not hit the PMT. [40]

Silicon strip detectors Silicon strip detectors have proven the capability of delivering great time and spacial resolution. Big collider experiments like ATLAS and CMS are already us-

ing this technology for their trackers. Commercially available Charge-coupled devices (CCD) would not work for single photon detection, they produce a lot of dark current. *Silicon strip detectors* are based on CCD-technology but there is an important difference. Common intrinsic¹ semiconductors have $> 10^6$ electrons per cubic centimeter excited to the conduction band [66]. The free electrons need to be removed, to be able to detect single photons. This is done with a high electric field inside the semiconductor. Now one can effectively suck out all free electrons without the creation of new electron-hole pairs. This is possible if the semiconductor has a diode structure, then it can be reversely biased, which results in a very small leakage current. Hence, the semiconductor has no free electrons in the conduction band left.

The basic geometry is a p-n-diode, where the p-type surface has been segmented. The n-type bulk is depleted of free charges, up to a thickness of 300 nm. The assembly is mounted on a n^+ -type back implant. The operation principle is comparable to an ionization chamber. An incident particle deposits energy and excites electrons into the conduction band, along the way. This creates electron-hole pairs. The charges then drift to the closest electrode. A schematic can be seen in figure 2.5

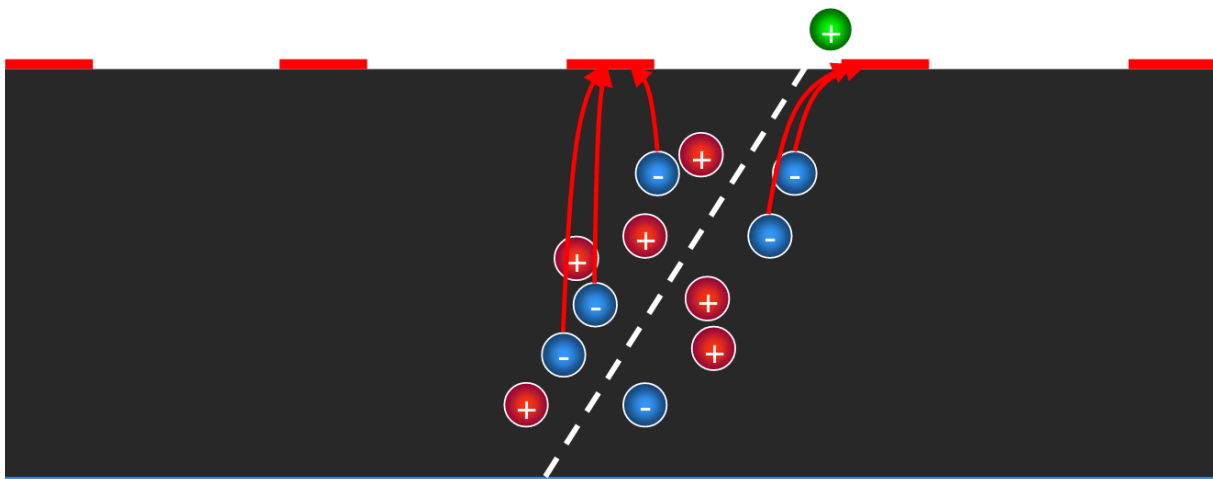


Figure 2.5: A schematic view showing the profile of a silicon strip detector. A particle (green) just passed through. Electron-hole pairs have been created along the track and the charges start drifting to their respective anode and cathode. [66]

A big drawback and the main reason why these are not used in liquid scintillator detectors today, is that large surface CCDs for single photon applications are still expensive and a high detector surface coverage is essential for a high energy resolution. But this may change in the near future, due to great investments in R&D, not only from science facilities but also commercial companies.

Large-Area Picosecond Photo-Detectors In 2009 LAPPD-Collaboration was formed. Its goal is to develop a photodetector which has picosecond timing and the size of a few decimeters.

¹Intrinsic semiconductors have very few impurities.

Since then several prototypes have been produced and recently a level of applicable photodetectors have been reached. A profile view is shown as a scheme in figure 2.6. The top window

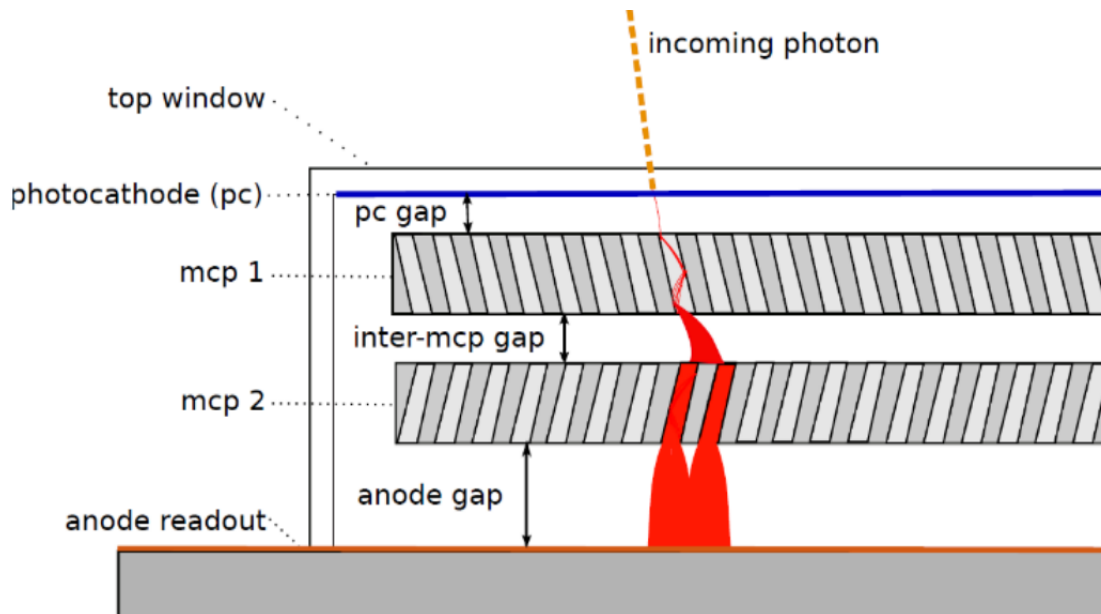


Figure 2.6: The profile view of a LAPPD. The top window has the photocathode (blue) on the inside. Two MCPs are the heart of the LAPPD. Only small gaps are in between the components, to keep the distance that electrons have to travel small. The readout anode (orange) picks up the knocked out electrons. All inner components are inside vacuum. [19]

is covered by the photocathode on the inside. Below that are multi channel plates (MCPs). The anode strips are located at the back. All inner components are in Vacuum.

A main feature for an LAPPD is the small TTS which enables the picosecond timing. This is feasible due to the use of MCP. The MCP is replacing the commonly used dynode setup. All distances between the components are small to keep electron travel times low. The MCP also enable the LAPPD to cover a large area. MCPs are basically about 2 mm thick plates made from lead glass, which have holes in the micrometer range in them. These are parallel and covered with semiconductor material inside. They are tilted about 10° , to ensure multiple scattering of entering electrons. Each hole acts as a continuous dynode.

An event in an LAPPD could develop as follows. A photon knocks out an electron at the photocathode which then enters the MCP. The electron is accelerated by a strong electric field and initiates a cascade inside the MCP. This results in a gain factor of about 10^7 after it was amplified by the 2 MCPs. This electric signal is then picked up by the anode strips at the back and can be read out.

Recent prototypes have shown a positional resolution of < 1 mm and a gain $> 10^7$. The single photoelectron (PE) timing with ~ 50 ps is very short compared to normal PMTs in nanosecond range. QE of about 5.5% is pretty low, considering the QE of common PMTs with 20-40%. Therefore future devices will aim for a QE of 20%. The size of an LAPPD is about 20×20 cm, which is about 1/5 of the surface a common 20 inch PMT covers. an Development of mass

production is planned as a next step. R&D costs let the price for LAPPDs still be high in the near future. Hence covering a large surface will be cheaper with standard PMTs, but one should not undervalue the advantages of LAPPDs. At the moment LAPPDs are available for the price of \$10000 each, when a volume of 1000 or higher is ordered [19].

2.2 LENA detector

As part of the *Large Apparatus studying Grand Unification and Neutrino Astrophysics* (LAGUNA) project, LENA was developed to help study the field of extraterrestrial neutrino physics and the *Grand Unification Theory* (GUT). Especially to investigate low energy neutrinos from sources like core collapse supernova explosions, the sun and the Earth. Its large target volume of 50 kt exceeds comparable existing detectors and with prime location it is very well capable of delivering precise measurements of low energy events. Moreover, by also researching the proton decay and delivering a precise measurement of neutrino flavor oscillation parameters, it would also greatly contribute to the GUT.

LENA would be the next-generation neutrino observatory in Europe and the world first utilizing large scale liquid scintillator technology, for its 50 kt target mass. In comparison to similar sized cherenkov detectors, LENA could measure neutrino events at energies way lower, than their threshold. At present LENA is not built and probably will not be built, but processes investigated for this project still generated useful knowledge for physics and other detector projects.

2.2.1 Physics motivation

Low energy neutrino events and proton decay are the driving factors for LENA. GUT and precise measurement of different neutrino sources hold great potential to learn something about our universe.

Core-collapse supernova neutrinos When the life of a star ends with a core-collapse SN, this is a great opportunity to understand HE physics. Especially if this happens within a distance to earth of less than 10 kp. Then LENA would be able to detect up to 10^4 neutrino events in about 10 seconds. Because of LENA's low energy threshold and precise energy resolution, one could test SN theory, by using the measurement of the ν_e and $\bar{\nu}_e$ fluxes with charge current interactions and the determination of total flux with various neutral current fluxes. Furthermore LENA would be part of the *Supernova Early Warning System* (SNEWS) and in cooperation could provide distance and direction of the SN, even in the case of visual obscuration. The so far undetected DSNB can possibly be detected with LENA, between the energy of 9.5 and 25 MeV. Due to interfering backgrounds, it would take 10 years to accumulate 20 to 40 confirmed signal events. This could give evidence for the existence of DSNB, with a significance of 3σ .

If no signal would be observed, LENA would improve the upper limit for DSNB by a factor of eight [45].

Solar neutrinos No intrinsic energy threshold and a large target volume of 50 kt liquid scintillator, with high radiopurity, enables LENA to do a precise measurement of solar neutrino fluxes. Due to the high rate of about 10^4 ^7Be -neutrino interactions per day, variation could be investigated. This enables one to research the stability of fusion in the sun. Furthermore a measurement of pep and CNO neutrinos would be possible, around 1-2 MeV. This holds information about the solar metallicity. Even though the background from ^{11}C is eight times higher, than the signal from pep and CNO neutrinos, one could probe the solar neutrino survivability P_{ee} , in the range of 1-5 MeV. The MSW effect predicts an upturn for P_{ee} in this range, which could be verified by LENA with a significance of 5σ [46].

Geo-neutrinos The $\bar{\nu}_e$ flux from the Earth can be measured with LENA. At the preferred potential location Pyhäsalmi, a precision of 2%, can be reached after 10 years. This already considers future planned reactors, in Finland. Also it would be possible to determine the flux contribution and ration of ^{238}U and ^{232}Th . Also within 10 years, the precision of flux for ^{238}U would be 4%, for ^{232}Th 7% and the ratio precision 11%.

Proton decay GUT and some *Supersymmetry* models, hypothesise the proton decay, based on deliberate breaking of baryon number symmetry. This would enable protons to decay in example, via Higgs particle or magnetic monopoles. A channel that could be observed with a liquid scintillator detector is $p \rightarrow K^+ + \bar{\nu}$. Measuring with LENA for ten years without any signal, would set a new limit for the proton time constant $\tau > 4 \times 10^{34}$ years.

2.2.2 Design

Location Possible sites for the detector location have been elaborated during the LAGUNA-Project. The most favorable places are the *Pyhäsalmi-mine* in Finland and *Modane Underground Laboratory*² (LSM) in France. The *Pyhäsalmi-mine* is currently the deepest mine in Europa, with a bottom level of about 1450 m below ground. For more muon shielding LSM with about 1700 m of rock overburden could be chosen. But the nearest nuclear power plant in *Pyhäsalmi* would be 350 km away and in LSM, 180 km. This has to be taken in to account for the $\bar{\nu}$ background flux. The radioactivity from surrounding rock, due to radon, is a higher at *Pyhäsalmi*, with 20 Bq/m³ than at LSM, with 15 Bq/m³. They both have fully developed access roads, but *Pyhäsalmi* also has rail access.

Geometry The current LENA detector layout for the site *Pyhäsalmi* can be seen in a cross section a figure 2.7. The 50 kt liquid scintillator LAB target is in the center, contained by a

² Laboratoire Souterrain de Modane (LSM)

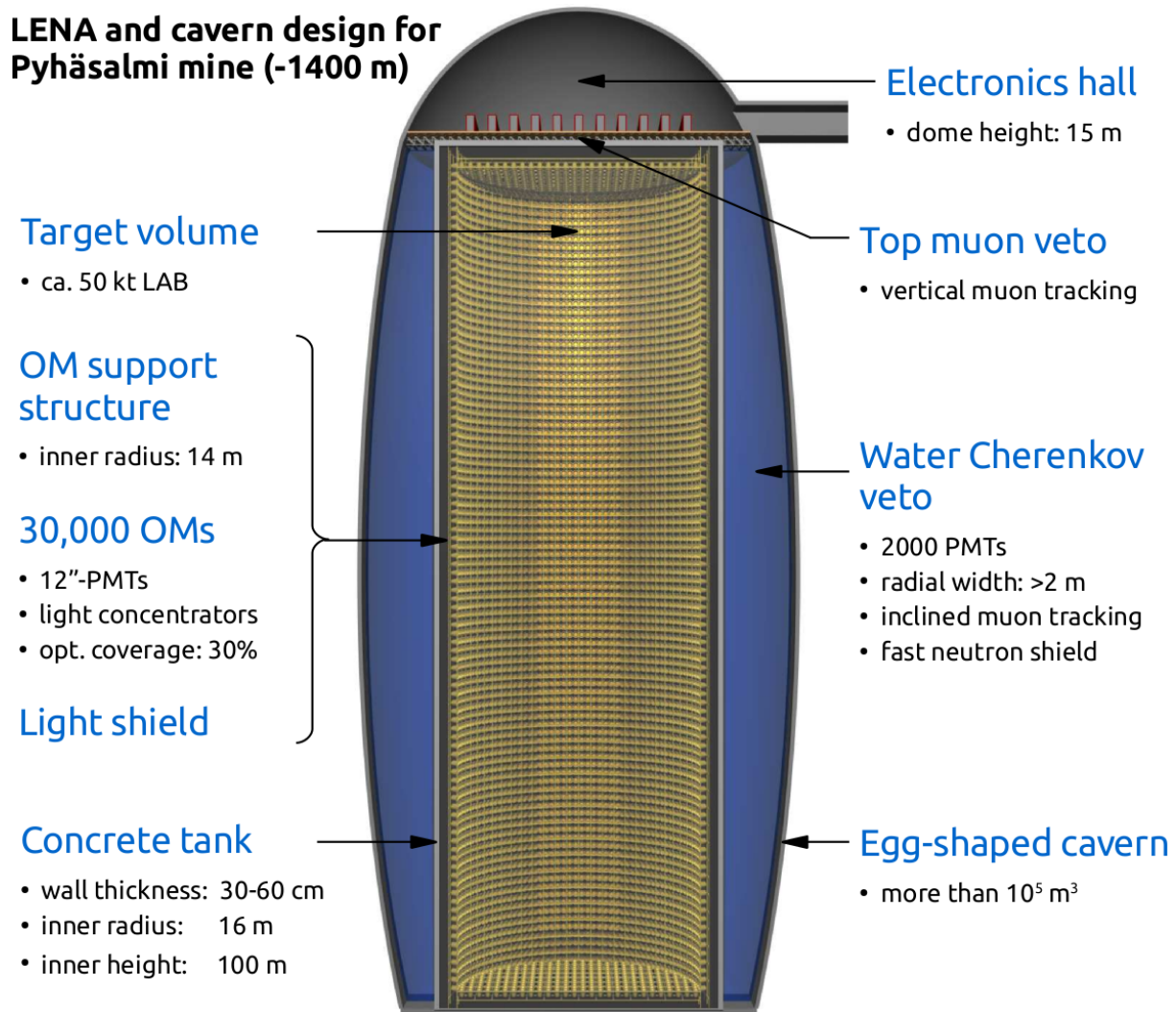


Figure 2.7: A cross section is shown, of the LENA detector as it planned at *Pyhäsalmi*. The center is accommodating one of the most important parts, the target, 50 kt of liquid LAB scintillator. The liquid scintillator is filling up the entire concrete tank and is also behind the OM support structure. The light shield prevents light to be detected from the scintillator that was generated behind the PMTs. It is also mounted on the OM support structure, like the 30000 OMs them self. The area between the cavern and the outside of the concrete tank is filled with water and acts as a muon veto via cherenkov radiation. The top dome is not filled with water and has electronics as well as the top muon veto in it. [70]

concrete tank. The cylindrical target is 96 m high and has a radius of 14 m. The concrete tank is 100 m high and has an inner radius of 16 m. To prevent contamination, a stainless-steel liner is mounted at the inner concrete wall. The *optical modules* (OMs) are mounted on the OM support structure, a scaffolding, which it self is anchored at the tank and is also inside the scintillator. The scaffolding also holds up the light shield, which prevents light to be detected by the OMs, when it was generated behind the OMs. The light shield is an opaque foil. OMs are mounted in such a way, that they are just outside the target volume. The OMs on the side wall look towards the center axis and the OMs on ceiling and floor look strait up/down. Outside of the concrete

tank is a muon veto, utilizing cherenkov radiation. It is filled with water. The water is situated between the cavern wall and the tank, which have a distance ≥ 2 m. To prevent water leaking through the concrete tank, the outside wall of it is coated with a *spray-on* plastic. The veto is equipped with about 2000 PMTs. The concrete tank ceiling is not covered with water, as instead it has a muon veto system mounted on top, to track down going muons. The cavern has also space to hold the data acquisition electronics.

Liquid scintillator General aspects of liquid scintillator are high radiopurity and a pulse shape, which enables pulse shape discrimination, for background rejection. Also the light emission fluorescence time should be taken into account, for time based reconstructions. Requirements for the liquid scintillator in LENA are determined by its geometric and optical design as well as LENA's research program. Because of the large dimensions, the scintillation light should be able to cover a distance above 15 m before being detected. Therefore an attenuation length of about 20 m and light yield of about 10000 photons per MeV are sensible. For the detection of proton decay, the proton density needs to be considered.

The two favoured bases for the LENA liquid scintillator mix are LAB and PXE. Even though PXE has faster scintillation light emission, ultimately LAB was chosen. LAB has a higher attenuation length and a higher number of free protons. But what really decided, was the fact that LAB already had a wide application in other experiments and therefore more knowledge about it. To increase attenuation length it would be mixed with 3g/l 2,5-diphenyloxazole (PPO) and 20 mg/l 1,4-Bis(2-methylstyryl) benzene (bis-MSB), resulting in a scintillation spectrum with a peak at 430 nm and a fast decay component of about 4.4 ns. A schematic of the scintillation process can be seen in figure 2.8.

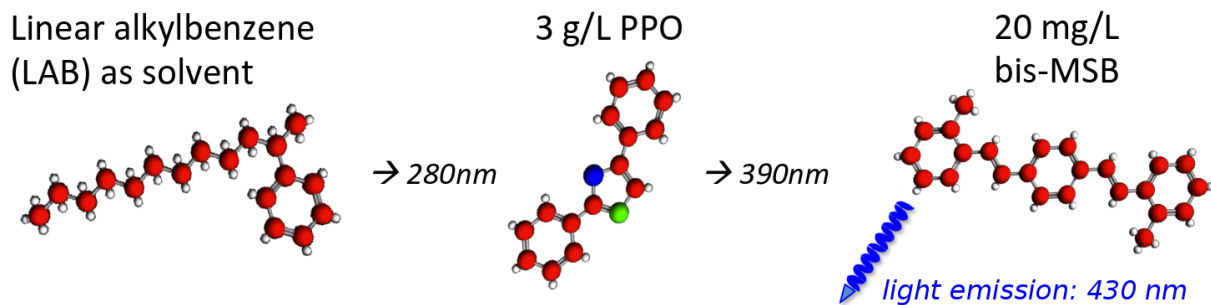


Figure 2.8: The scintillation process anticipated for LENA. On the left a LAB molecule producing the initial scintillation light. The light is being shifted by PPO from 280 nm to 390 nm. Finally the light is emitted by bis-MSB shifted to a wavelength of 430 nm. The resulting fast decay component is about 4.4 ns. [70]

Optical modules Part of the OM is the PMT, but other things are also included in the OM. A scheme is shown in figure 2.9. The OM is planned with a steel encapsulation, which has an acrylic glass window. That way it can withstand the hydrostatic pressure. The Winston cone is mounted inside the OM, on top of the PMT. Radiation from the acrylic glass could produce

light right in front of the PMT. To prevent this from happening between the acrylic window and the PMT, the inside of the Winston cone, is filled with non scintillating mineral oil. The PMT is mounted in the PMT socket, which is hold in place by polyurethane. To shield the PMT against the outside magnetic fields it is surrounded by a sheet of μ -metal. Its a 12" PMT, with a peak quantum efficiency $> 20\%$ and a TTS of < 1.5 ns. The light concentrator raise the effective area of a PMT by a factor of 1.5, this increase the optical coverage. It is to note that this lowers the angular acceptance, to a cone with an opening angle of about 90° .

LENA is planned to contain 30000 of these OMs, with 4×4 arrays being mounted into the scaffolding. Optical coverage would be 30%, with the mentioned PMT quantum efficiency of 20%, the overall light collection efficiency lies around 6%.

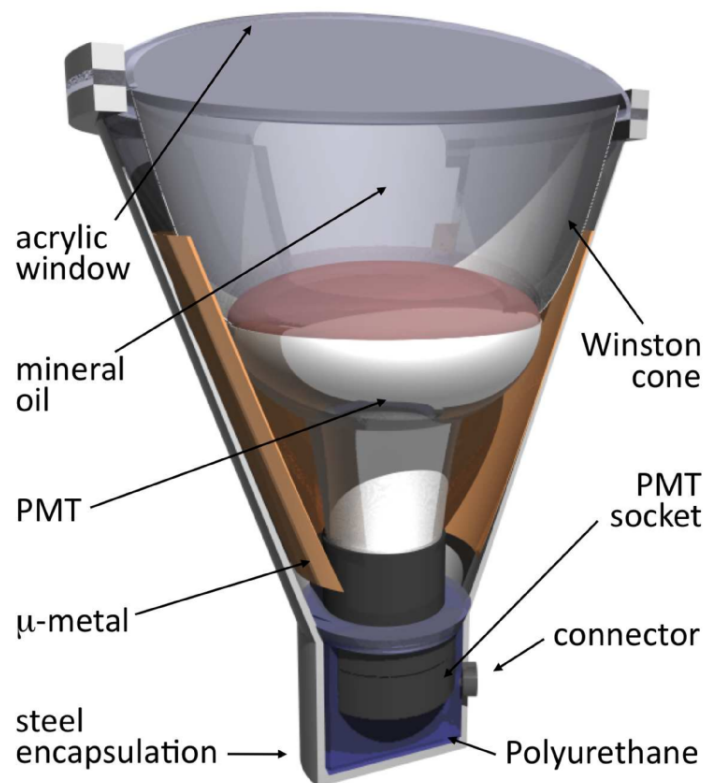


Figure 2.9: The basic OM planned for LENA. It consists of a 12" PMT shielded with μ -metal, a light concentrator on top and all encapsulated by steel and an acrylic window. The PMTs peak quantum efficiency is $> 20\%$ and has a TTS < 1.5 ns. The light concentrator increases the effective area by a factor of 1.5 but lowers the radial acceptance. [70]

2.3 JUNO detector

2008 DAYA BAY II was proposed, a medium baseline reactor neutrino experiment. 2012 the preferred detector location changed to *Jiangmen city* in the *Guangdong* province, China. Hence

the experiment was renamed to Jiangmen Underground Neutrino Observatory (JUNO). The main goal is to determine the neutrino MO. This will be done utilizing reactor $\bar{\nu}_e$ disappearance with a baseline of about 52 km. Other physics goals are, the precise measurement of neutrino flavor oscillation and solar, geo-neutrino, SN neutrino as well as DSNB measurements.

2.3.1 Physics motivation

The research program of JUNO is comparable to the one LENA has proposed, with the exception of the precise measurement of neutrino flavor oscillation parameters, to determine the neutrino MO. For this an excellent energy resolution is of the essence. JUNO is aiming for a relative visible energy resolution of at least 3% [38]. This would result in a confidence level of 3 to 4 sigma for neutrino MO. Respectively for the true MO, the equations (2.10) for neutrino mass-squared differences are valid [73].

$$\begin{aligned} \Delta m_{31}^2 &= \Delta m_{32}^2 + \Delta m_{21}^2 \\ \text{NO: } |\Delta m_{31}^2| &= |\Delta m_{32}^2| + |\Delta m_{21}^2| \\ \text{IO: } |\Delta m_{31}^2| &= |\Delta m_{32}^2| - |\Delta m_{21}^2| \end{aligned} \quad (2.10)$$

It would be possible to determine the MO by a precise measurement of $|\Delta m_{31}^2|$ and $|\Delta m_{32}^2|$, but in reality this is difficult since Δm_{21}^2 is only $\sim 3\%$ of $|\Delta m_{32}^2|$. Therefore Δm_{21}^2 and $|\Delta m_{32}^2|$ need to be measured with a precision higher than 3%, which also is a reason for JUNOs energy resolution. The underlying method, to determine MO by a single remote detector with reactor antineutrinos, is described in [36]. It does not rely on the reactor flux spectrum or matter effects. Instead it uses a Fourier transformed L/E spectrum of the reactor neutrinos. The reactor $\bar{\nu}_e$ spectrum $F(L/E)$, for a baseline L and energy E , can be written as

$$F(L/E) = \phi(E) \sigma(E) P_{ee}(L/E), \quad (2.11)$$

where $\phi(E)$ is the reactor $\bar{\nu}_e$ flux, $\sigma(E)$ is the cross section at energy E for the inverse- β decay ($\bar{\nu}_e + p \rightarrow e^+ + n$) and $P_{ee}(L/E)$ is the survival probability for an $\bar{\nu}_e$. $P_{ee}(L/E)$ is given by equation (2.12):

$$\begin{aligned} P_{ee}(L/E) &= 1 - P_{21} - P_{31} - P_{32} \\ P_{21} &= \cos^4(\Theta_{13}) \sin^2(2\Theta_{12}) \sin^2(\Delta_{21}) \\ P_{31} &= \cos^4(\Theta_{12}) \sin^2(2\Theta_{13}) \sin^2(\Delta_{31}) \\ P_{32} &= \cos^4(\Theta_{12}) \sin^2(2\Theta_{13}) \sin^2(\Delta_{32}), \end{aligned} \quad (2.12)$$

where $\Delta_{ij} = 1.27 \frac{\Delta m_{ij}^2 L}{E}$, Δm_{ij}^2 is the neutrino mass-squared difference and Θ_{ij} is the neutrino mixing angle. The three oscillation components P_{21} , P_{31} and P_{32} are proportional to $|\Delta m_{ij}^2|$. $P_{ee}(L/E)$ is dominated by $1 - P_{21}$ and P_{31} , P_{32} are the components which are sensitive to neutrino

MO.

The neutrino spectrum in L/E space can be seen in figure 2.10. A baseline L of 60 km was used, the other parameters can be found in the TABLE 1 of ref. [73]. For comparison also the spectrum with no oscillation and the spectrum for only $1 - P_{21}$ part are shown. Performing a Fourier transformation on $F(L/E)$ will allow the determine of the true neutrino MO.

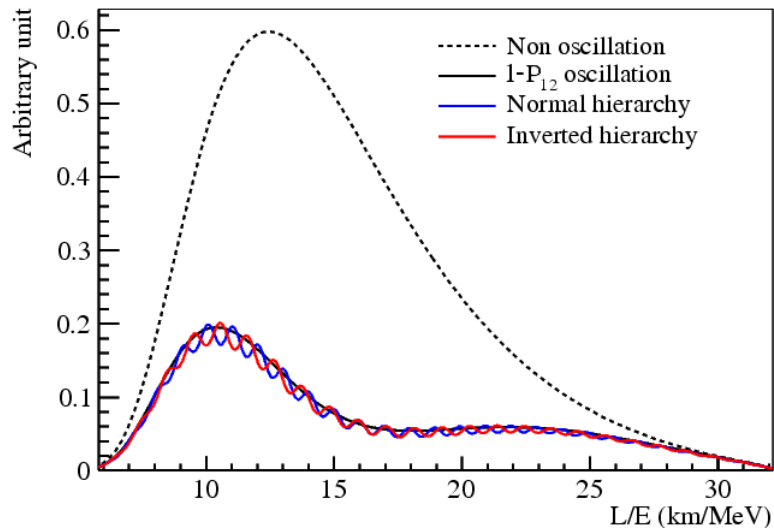


Figure 2.10: Reactor neutrino spectra in L/E space. A baseline of 60 km was used. Black dashed line for no oscillation, black line only $1 - P_{12}$ term. Blue line expected if normal MO is true and red line expected if inverted MO is true. Original graph and parameters used to generate it can be looked up in [73].

The high energy resolution and expected large number of events enables JUNO to perform a precise measurement of neutrino flavor oscillation parameters. Possible high precision measurements are Δm_{21}^2 , $\sin^2(\Theta_{12})$ and $|\Delta m_{ee}^2| = |\cos^2\Theta_{12}\Delta m_{31}^2 + \sin^2\Theta_{12}\Delta m_{32}^2|$. The predicted measurement uncertainties are stated in Table 2.2.

Table 2.2: Precision improvement for Δm_{21}^2 , $|\Delta m_{ee}^2|$ and $\sin^2(\Theta_{12})$, which is made possible with JUNO. The 1σ uncertainties after six years. Precision today from a global analysis [28]. Feasibility for JUNO measurement calculated in [7].

oscillation parameter	precision today	precision JUNO
Δm_{21}^2	2.4%	0.59%
$ \Delta m_{ee}^2 $	1.9%	0.44%
$\sin^2(\Theta_{12})$	4.1%	0.67%

In general all the points stated in section 2.2.1 of LENAs research program are also applicable for JUNO and will be measured by it. LENA has a larger target volume and would be deeper underground, which would result in more events and lower background. JUNO on the other hand has a superior energy resolution, which is perfect for the research focus it has.

2.3.2 Design

Location The detector construction site is located in *Jinji town*. The nuclear power plants are in *Yangjiang* and *Taishan*, with six and four cores, they will provide the main $\bar{\nu}_e$ flux. Even though these are in different cities, the detector location is chosen in such a way that the baseline of 52.48 km varies less than 500 m. The 215 km distant nuclear reactor, at *Daya Bay*, will only contribute $\sim 2.8\%$ to the $\bar{\nu}_e$ flux. To reduce cosmogenic background events, the detector will be built ~ 460 m underground, at a location that has a 268 m high hill on top. The muon rate at that depth is estimated to be $\sim 3 \text{ s}^{-1}$, in the whole detector volume. Measurements of the rock radio activity revealed 1305 Bq/kg [7].

Detector geometry The geometry is mainly derived from the need of a superior energy resolution, to fulfill JUNO's physics potential. Hence, the main effort is being put into the discrimination of single PE, in order to maximise detection and minimize statistical uncertainty. For a uniform PE detection the target is a sphere. A profile of the currently planned detector can be seen in figure 2.11. The target holds 20 kt of the liquid scintillator LAB. The diameter is \sim

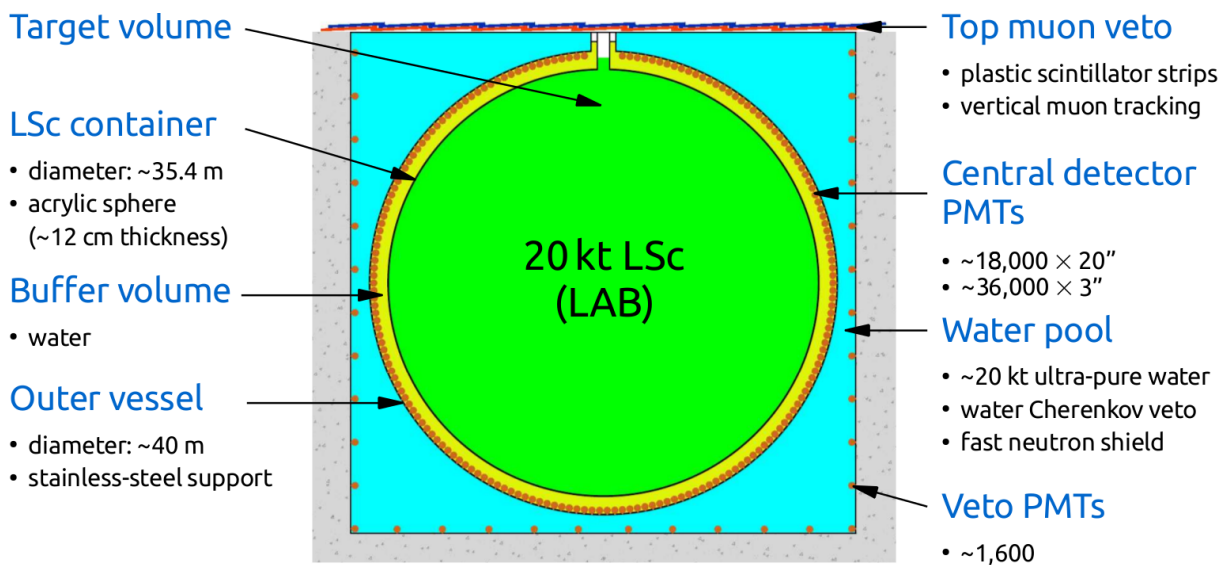


Figure 2.11: A profile view of the planned JUNO detector. The inner target volume (green) is filled with 20 kt liquid scintillator LAB. It is contained in an acrylic sphere, which has a thickness of ~ 12 cm. About 18000 20" + 36000 3" PMTs (orange dots) will face directly onto the acrylic sphere, into the target volume. They are mounted on a stainless-steel support, which also holds the acrylic sphere in place. All this stands in a cylindrical volume, filled with pure water. About 1600 PMTs are mounted at the inner surface of that. Light leaking from the outside veto water (cyan) to the detector and buffer water (yellow) is prevented. Plastic strip detectors will be mounted on top of the whole detector. [7]

35.4 m and the scintillator is contained in an acrylic sphere. Anything outside of that sphere is submerged in pure water. Arising from the different densities inside and outside the acrylic sphere, it needs to be ~ 12 cm thick to withstand the forces. To hold the liquid scintillator bub-

ble below the water, a stainless-steel support is constructed, which holds the acrylic sphere and also the PMTs in place. The structure has a diameter of ~ 40 m. Directly facing the center are ~ 18000 20" PMTs. Additionally there are ~ 36000 3" PMTs in between the 20" PMTs, which also face the center. The water also shields against emitted radiation from the support structure and PMT glass. The cylindrical volume of ~ 20 kt water, in which the detector stands, also acts as a cherenkov muon veto and fast neutron shield. There will be about 1600 PMTs mounted at the inner cylinders surface for this purpose. Light leaking from the veto into the inner detector is prevented. On top of the detector a muon tracker consisting of scintillator strips is mounted. It will be reusing the target tracker of the OPERA experiment. It will cover more that 25% of the detectors ceiling.

Liquid scintillator Due to the needed energy resolution and size, an attenuation length of ≥ 22 m is needed, at a wavelength of 430 nm. This results in an absorption length of 60 m. The light yield should be around 10000 photons per MeV.

LAB is the base for the mixture used in JUNO. The mixture will also contain PPO and bis-MSB like intended for LENA. The scintillation process will be the same as the one that can be seen in figure 2.8, but the quantities will change. Still 3 g/L PPO will be used, but 15 mg/L bis-MSB are intended. The mix will not be doped with gadolinium [7]. The central detector will be filled with 20 kT liquid scintillator. The needed radiopurity, to be able to detect antineutrino and solar neutrino events, is stated in table 2.3.

Table 2.3: The needed radiopurity for liquid scintillator to be used in JUNO. Lower concentrations enable the detection of antineutrinos and solar neutrinos. [18]

Concentrations [g/g]	$\bar{\nu}_e$ detection	ν_e detection
^{238}U	$\leq 10^{-15}$	$\leq 10^{-17}$
^{232}Th	$\leq 10^{-15}$	$\leq 10^{-17}$
^{40}K	$\leq 10^{-16}$	$\leq 10^{-18}$

Optical modules Achieving the energy resolution of $3\%/\sqrt{E(\text{MeV})}$, implies a great challenge for the photon detection in JUNO. With a Monte Carlo simulation, based on Daya Bay, it was determined that an optical coverage $\geq 75\%$ and a QE $\geq 35\%$ will be needed. Then the energy resolution of $3\%/\sqrt{E(\text{MeV})}$ can be reached with the selected scintillator mixture.

The final design for the optical module is not decided yet, but specifications for the photon detection already exist. The peak photon detection efficiency needs to be $\geq 35\%$ and for the broad scintillation spectrum photon detection efficiency $\geq 30\%$ is anticipated. To achieve this,

the anode is implied to have a 93 % collection efficiency and the photocathode needs to reach a peak QE of 38 % at ~ 430 nm [18].

So far these were unreachable levels for commercially available large PMTs. Therefore, R&D for a new kind of PMT was initiated. The result is the MCP-PMT. A concept drawing can be seen in figure 2.12. This MCP-PMT has a spheric concept design (another concept design looks more parabolic shaped), with two hemispheres that have different photocathodes. The front one is a traditional transmission photocathode and the back one is a reflection photocathode. In case of a photon not being converted at the transmission photocathode, there is the possibility of conversion in the back of the PMT at the reflection photocathode. Through variation of photocathode thickness the high QE which is needed may be achieved.

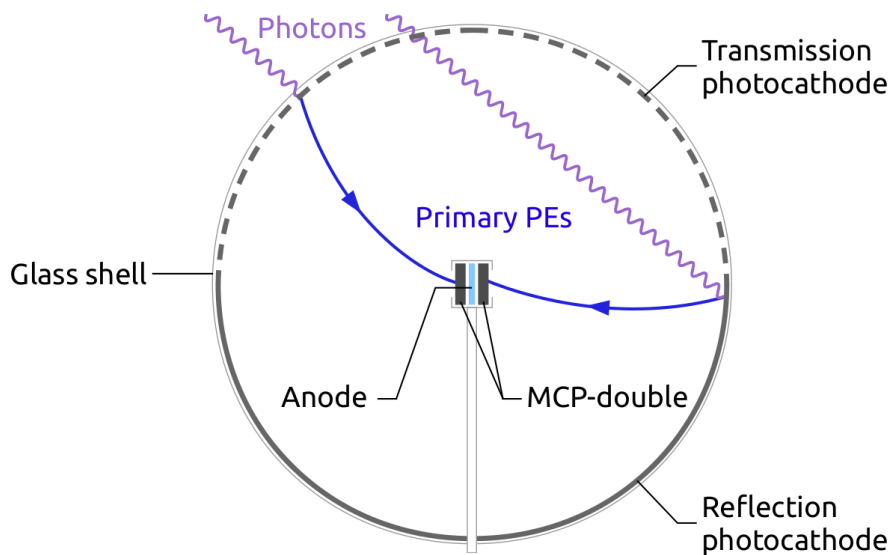


Figure 2.12: A concept view of a MCP-PMT. As an example event, two parallel incident photons (purple) reach the PMT. One is converted in to an electron at the transmission photocathode and the other one is converted later at the reflection photocathode. The photoelectrons (blue) drift into the MCPs and generate an avalanche of electrons, which becomes a measurable signal. [40]

Meanwhile, *Hamamatsu*³ has developed highly efficient 20 ” dynode-PMTs for the future experiment Hyper Kamiokande, in Japan. These are based on their already existing 20 ” PMT designs. Hence, now two possible PMT solutions are available for JUNO. Both designs, the one from *Hamamatsu* and the MCP-PMT, will be used in JUNO. The gaps between the large PMTs will be filled with ~ 36000 3” PMTs. This enhances the optical coverage even more and therefore reduce the needed PDE. How many actually will be put into the detector depends on the space that the final optical module setup will take up. The size and shape of the OMs is partly determined by the implosion prevention, the use of light concentrators and the use of additional magnetic field shielding.

³Manufacturer for optical sensors, in Japan.

Chapter 3

Event simulation

For the two experiments, LENA and JUNO, their respective simulation software has been used. In case of the LENA experiment the similarly named Simulation (LENA Simulation) was used and for the JUNO-Experiment, *Software for Non-collider Physics Experiment* (SNiPER-Framework), has been the tool for event simulation. In the next section there will be more detail about the functions and settings that have been imposed, for the different experiments.

3.1 LENA simulation

This simulation is programmed in C and C++. The backbone of the actual physics simulation is made with GEANT4¹[3, 6]. For easy result utilization ROOT²[9] was chosen, it stores the simulation output. The LENA detector Simulation was first developed at "Technische Universität München", in 2005, for low energy neutrino detection and proton decay. The scope has since then grown in a fully developed detector simulation, supporting various aspects, like multi-GeV neutrinos and muons [68, 44].

The simulation was used to provide the vertex reconstruction with the same data, as is used in the LENA reconstruction. To be able to generate a significantly large quantity of sample data, the simulation does not capture the LENA detector in all physical detail, but instead some optimization for otherwise computation time intensive processes have been made. The differences between the optimizations and the underlying physics will be described in the next sections.

3.1.1 Geometrical layout

The construction of the detector in GEANT4, consists of multiple, encapsulated, tubes. A scheme of the simulated detector geometry can be seen in figure 3.1. The exact dimensions are stated in table 3.1 and the distribution of optical modules can be found in table 3.2. The innermost cylinder is the target volume, containing liquid scintillator and has a radius of 14 m.

¹*Geometry and tracking* (GEANT) a toolkit to simulate the interaction of particles with matter. Its based around MC methods. Version 4.9.6 was used.

²An Object-Oriented Data Analysis Framework. Version 5.34.07 was used.

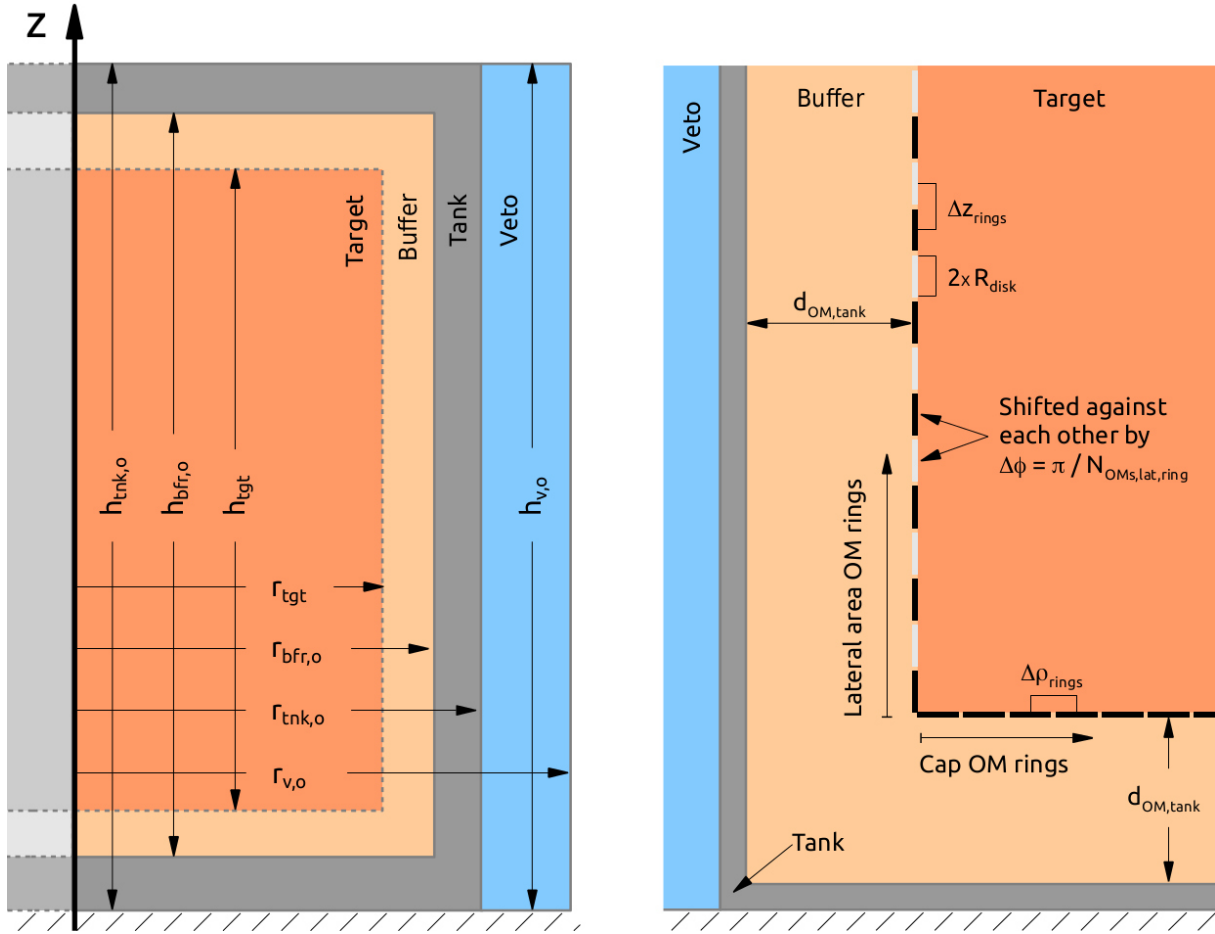


Figure 3.1: LENA detector simulation geometrical layout. In this not to scale schematics, one can see on the left a projection of the simulated, encapsulated, tubes. The innermost cylinder is the target. Enclosed by the buffer, then the tank and the outer most cylinder being the Veto. The used geometry parameters are stated in table 3.1. On the right the positioning of the optical modules, which are approximating the PMTs, are shown. These circular disks are located 5 cm outside the target volume. At the wall of the cylinder, they form rings which are shifted against each other by $\Delta\phi = \pi / N_{OMs,lat,ring}$. The exact positioning parameters can be obtained from table 3.2. [40]

Table 3.1: This table contains the geometric parameters used for the event simulation, with the LENA detector. The corresponding parameters can be found in schematic 3.1.

Description	Parameter	Value
Target radius	r_{tgt}	14.0 m
Buffer outside radius	$r_{bfr,o}$	16.0 m
Tank outside radius	$r_{tnk,o}$	16.6 m
Veto outside radius	$r_{v,o}$	18.6 m
Target hight	h_{tgt}	96.0 m
Buffer outside hight	$h_{bfr,o}$	100.0 m
Tank outside height	$h_{tnk,o}$	101.2 m
Veto outside height	h_{tgt}	101.2 m

Table 3.2: The parameters in this table describes the optical module distribution. A visualization of these parameters can be found in schematic 3.1.

Description	Parameter	Value
Number of optical modules	N_{OMs}	30542
Optical modules on wall	$N_{OMs,lat}$	26640
Optical modules per ring	$N_{OMs,lat,ring}$	144
Number of rings on wall	$N_{rings,lat}$	185
Optical modules on cap	$N_{OMs,cap}$	1951
Rings of optical modules on cap	$N_{rings,cap}$	25
Optical modules cap inner ring	$N_{1stRing,cap}$	6
Optical modules inner wall distance	$d_{OM,tank}$	195 cm
Hight difference of adjacent wall rings	Δz_{rings}	51.9 cm
Radial distance to adjacent cap rings	$\Delta \rho_{rings}$	55.1 cm
Radius of the optical module disks	R_{disk}	25.5 cm

Just outside of that, in a distance of 5 cm, are the optical modules located, which approximate the PMTs in this simulation. They are located inside the buffer volume. It is enclosing the target volume and is also filled with liquid scintillator. There is no physical separation implemented between these 2 volumes, but the buffer volume can not emit light and no light is reflected from the inner tank wall. The simulation was build this way, since in the real experiment it was planned to have the PMT holding structure inside the liquid scintillator and a light absorbing foil in the same plane as the PMTs. That way no light could leak from behind the PMTs. The same is achieved with this simulated setup, of target and buffer. The foil and PMT holding structure are not implemented in the simulation. Also not implemented is a shielding of the inner tank wall to prevent contamination of the liquid scintillator, which does not happen in the simulation anyway. The tank encapsulating the liquid scintillator is simulated to be out of concrete and outside of that is the veto which is filled with water.

3.1.2 Material physics and light emission model

Materials in the simulated detector compared to the reality are some what different. Most of the physical effects are simulated by GEANT4 already, for example the Cherenkov light emission and Rayleigh scattering process. Some modules were custom made for the detector simulation, partly for optimization reasons and partly to exceed the GEANT4 model. The custom modules mostly affect the liquid scintillator, hence the next part will be about that.

The liquid scintillator used for all simulated events is LAB. Parameters defining LAB in the simulation are stated in table 3.3. The target and buffer volume are purely filled with LAB, no wavelength-shifting component or dissolved impurities are mixed into the simulated material. However, the wavelength shifting effect is taken into account and emulated, by the weights and timing described by the p.d.f. for the photon emission, which corresponds to a mixture of LAB and 2 g/l PPO[49]. This is part of the custom module for the scintillation process. It was

Table 3.3: This table holds the parameters for the liquid scintillator (LAB) used for the simulation. The Parameters refractive index, absorption and scattering length are in reality wavelength dependent, but the simulation treats them wavelength independent for optimization. [44]

Description	Parameter	Value
Mass density	ρ_m	0.86 g cm^{-3}
Refractive index	n	1.484
Absorption length	l_A	20 m
Rayleigh scattering length	l_{ray}	40 m
Isotropic scattering length	l_{iso}	60 m
Light yield (target)	\mathcal{L}_0	2000 MeV^{-1}
Light yield (buffer)	\mathcal{L}'_0	0 MeV^{-1}
Birks constant	kB	0.15 mm MeV^{-1}
1 st time component	τ_1	4.6 ns
2 nd time component	τ_2	18.0 ns
3 rd time component	τ_3	156.0 ns
Weight of 1 st time component	ω_1	0.71
Weight of 2 nd time component	ω_2	0.22
Weight of 3 rd time component	ω_3	0.07
Re-emission time constant	τ_{rem}	1.2 ns

implemented to replace the GEANT4 scintillation process, which does not support more than two time components τ for the timing p.d.f. and does not respect quenching effects.

Another unique module is the scintillation process. The custom implementation of the scintillation process calculates the deposition of energy per unit length dE/dx , for a charged particle. According to that energy the mean number μ_γ of emitted scintillation photons is determined. The actual number of photons is then randomly chosen from a Poisson distribution $\mathcal{P}(\mu_\gamma)$. If the mean number μ_γ happens to be smaller or equal to 10 a normal distribution $\mathcal{N}(\mu_\gamma, \sqrt{\mu_\gamma})$ is replacing the Poissonian, as an optimization. The photons are isotropically, uniformly emitted along the track segment and have a random linear polarization. The emission time is randomly delayed according to the p.d.f. weighted with the scintillation components from table 3.3. To save computation time wavelength-dependent effects are neglected. Hence the refractive index, absorption and scattering length are set to fixed values. Also the emitted photon wavelength is limited to a range of 420-430 nm, which is close to the emission maximum of the anticipated scintillator mixture. Therefore all photons travel with a constant phase velocity of $c = c_0/n$.

The isotropic scattering in the simulation is also a custom module [40]. A measurement of isotropic scattering in LAB revealed that absorption and reemission is the largest contributor [71]. Hence it was implemented that the incident photon is absorbed and a new photon is isotropically re-emitted. It is linear polarized and the wavelength is restricted to $\lambda_{in} < \lambda_{out} \leq 430$ nm. The time Δt to be re-emitted is randomized, weighted by the p.d.f. in equation (3.1) and the re-emission time constant τ_{rem} is 1.2 ns, as stated in table 3.3.

$$\Phi(\Delta t; \tau_{rem}) = \frac{1}{\tau_{rem}} e^{-\frac{\Delta t}{\tau_{rem}}} \quad (3.1)$$

To speed up the simulation the cherenkov light and backgrounds are not simulated in any of the used LENA-Events. This also introduces some simplifications for the reconstruction. Hence, reconstructing events in a real experiment would not be reconstructed as well as the simulated events would suggest. Further testing is of the essence.

3.1.3 PMT model

For simplification the PMTs are not modeled in great detail. Instead they are approximated by a flat circular disc, which have the radius of the Winston cone opening and one photosensitive side. This optical module accepts photons based on incident angle Θ . It is modeled after the light concentrator acceptance probability $P_{accept}(\Theta)$, of a Winston cone. First the angle Θ is determined, then the acceptance probability is looked up in a table. The table drawn as a dependence of Θ can be seen in figure 3.2. It was calculated by simulating a significant amount of photon tracks onto a geometrically modeled winston cone [44]. The data is averaged and hence it is used on all points of the photosensitive side. Weighted with the probability $P_{accept}(\Theta)$ a MC process determines if the photon hit is accepted or not. Not accepted photons are not reflected. Even though the probability of reflection exists in the real experiment, it is

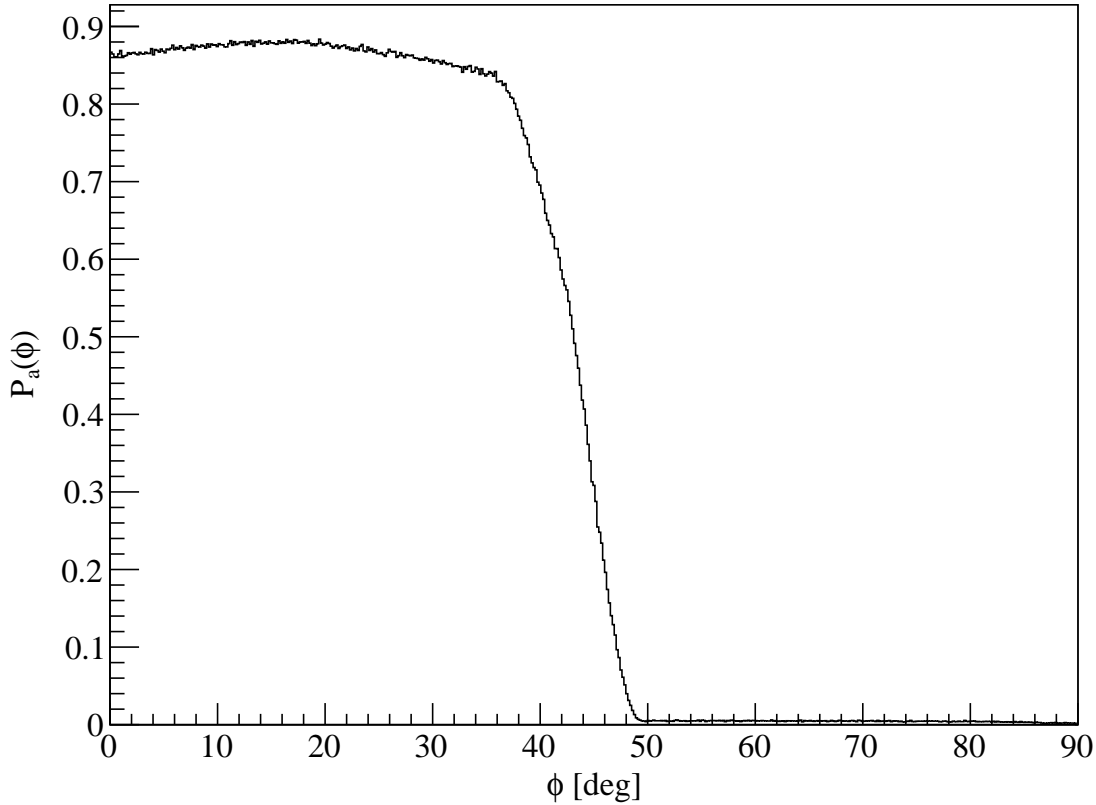


Figure 3.2: Winston Cone acceptance histogram. Probability $P_a(\Phi)$ over Angle Φ from PMT-axis in degrees. This histogram is used to determine the probability of photons being accepted by the Optical module. It was generated with a MC simulation, which used the geometrical model of the light concentrator used in Borexino [48]. The reflectivity was 87% and it had a critical incident angle of about 44° . The critical incident describes the angle from which on less than 50% of the photons are detected. This lookup table is taken from the simulation.

about 4% and therefore negligible [44]. Every accepted photon counts as a direct PMT hit and its arrival time is saved to the unique ID of the optical module. This would create a QE of 100%, but to counter this and further reduce computation time the light yield of $\sim 10000 \text{ MeV}^{-1}$ is reduced to 2000 MeV^{-1} , which corresponds to a QE of 20%.

No proper model for the attaching PMT electronics was developed. The only effect emulated from the electronics is the transit time spread, of the electron multipliers. Therefore the exact photon arrival times t are smeared out to t' , after the simulation in the manner of equation (3.2). The δt is the random time spread, which is drawn from a normal distribution $\mathcal{N}(0, \Delta T)$. The FWHM of this $\mathcal{N}(0, \Delta T)$ is 2.4 ns.

$$t' = t + \delta t \quad (3.2)$$

3.2 JUNO-simulation

The JUNO-simulation this has been used for the creation of sample data. But not in large quantities as instead as a prove of concept, that the vertex reconstruction also is applicable for the JUNO experiment.

The SNI_{PER} framework [75] is makes use of with python and C++. The JUNO-simulation is implemented with the SNI_{PER} framework and the JUNO software is called *Offline* within the framework. The physics simulation is being done with GEANT4 and for result utilization, ROOT is used to save the generated data. The implementation of JUNO in the SNI_{PER} framework aims to produce a very accurate simulation of the JUNO detector. At the current status many details have already been incorporated. The next sections will describe the geometry and physic parameters used in the simulation.

3.2.1 Geometrical layout

The geometry of the detector is simulated with GEANT4. A schematic showing how the detector is geometrically arranged, can be seen in figure 3.3.

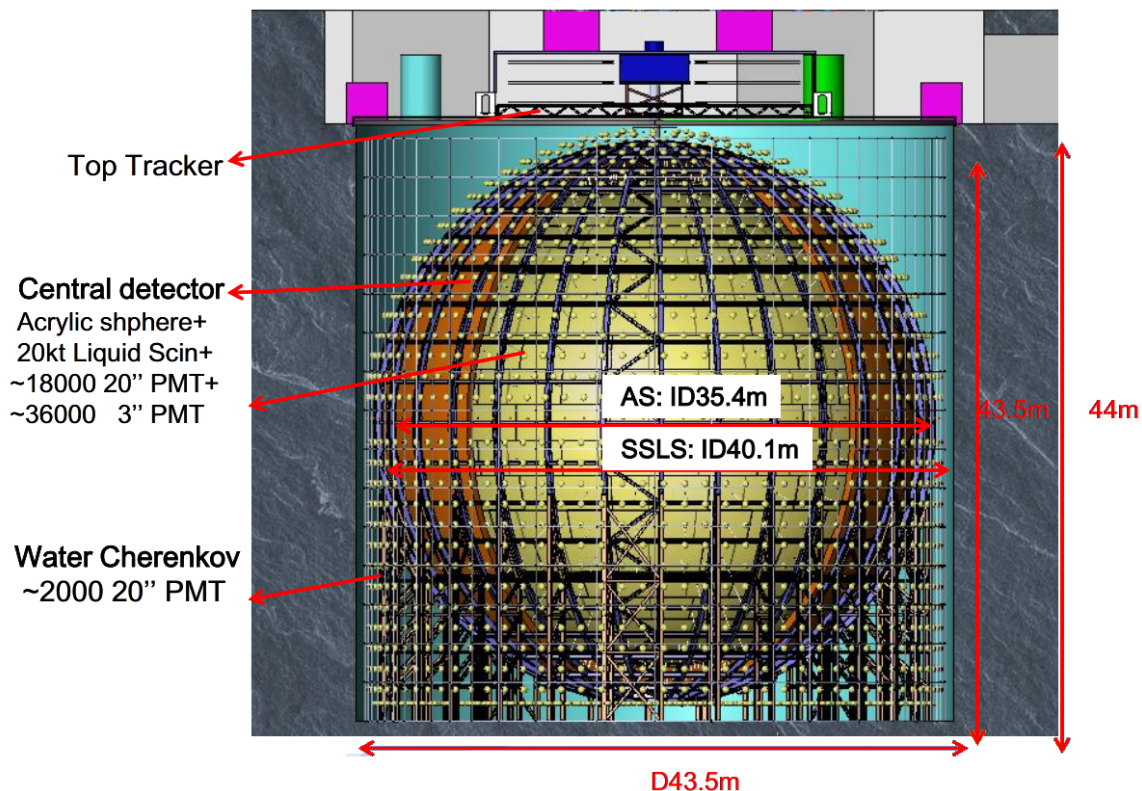


Figure 3.3: A schematic view showing the simulated geometry of the JUNO detector. One can see the simulated structure in the detector. The illustration is detailed, showing the target surrounded by the acrylic sphere construction and the support structure. Also the PMT positions for the water cherenkov veto are shown, as well as the experimental hall above with the top tracker. Also the surrounding rock is simulated. [41]

The simulation incorporates the central detector, which is composed of the target, the PMTs, the acrylic sphere construction and the supporting structure. It is emerged in the water of the water cherenkov veto. Also the rock surrounding the experiment and the top tracker inside experimental hall on top of the detector is simulated. The used dimensions can be taken from table 3.4.

Table 3.4: The geometric parameters describing the JUNO detector in the simulation.

Description	Value
Inner diameter acrylic sphere	35.4 m
Acrylic sphere thickness	0.12 m
Inner diameter support structure	40.1 m
Water veto volume height	43.5 m
Water veto volume diameter	43.5 m
Experiment hall height	18.6 m
Experiment hall in x & y	48.0 m

The number of PMTs in the simulation are stated in table 3.5. The exact PMT positions are saved in hard coded lists and can be found in the simulation code, in `offline/Simulation/DetSimV2/DetSimOptions/data/`.

Table 3.5: Number of PMTs used in the JUNO detector simulation.

Description	Value
Central detector 20" PMTs	17739
Central detector 3" PMTs	36572
Water veto detector 20" PMTs	2307

3.2.2 Material physics and light emission model

The material properties in the JUNO simulation are wavelength dependent. The currently implemented parameters can be seen in the figure 3.4 and figure 3.5. The decay components of the liquid scintillator are stated in table 3.6. The scintillation light yield is set to 11522 MeV^{-1} .

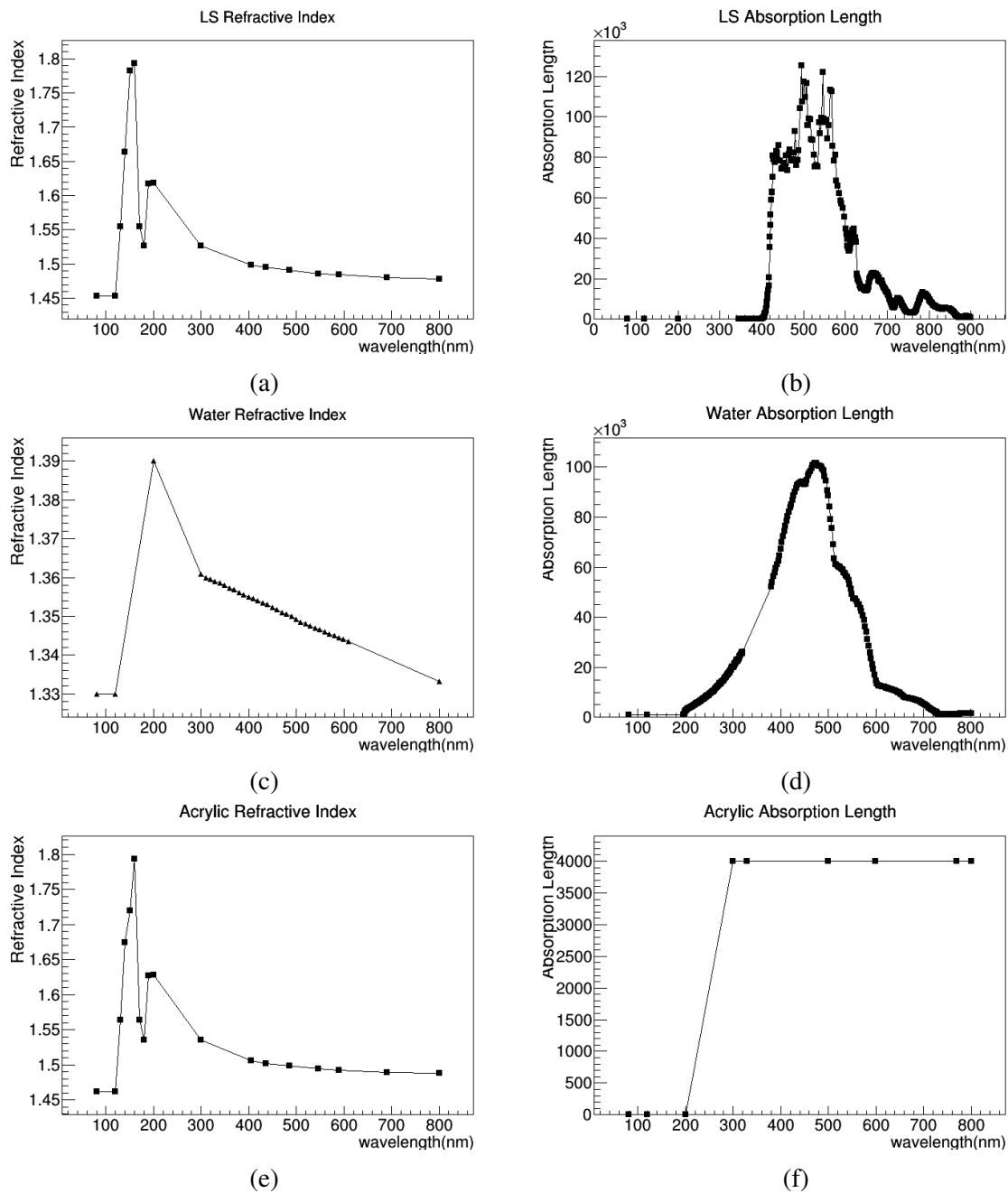


Figure 3.4: The refractive indices (left) and absorption lengths (right) for different materials in the JUNO simulation. They are wavelength dependent. (a) & (b) are for liquid scintillator, (c) & (d) are for water and (e) & (f) are for the acrylic sphere construction. [33]

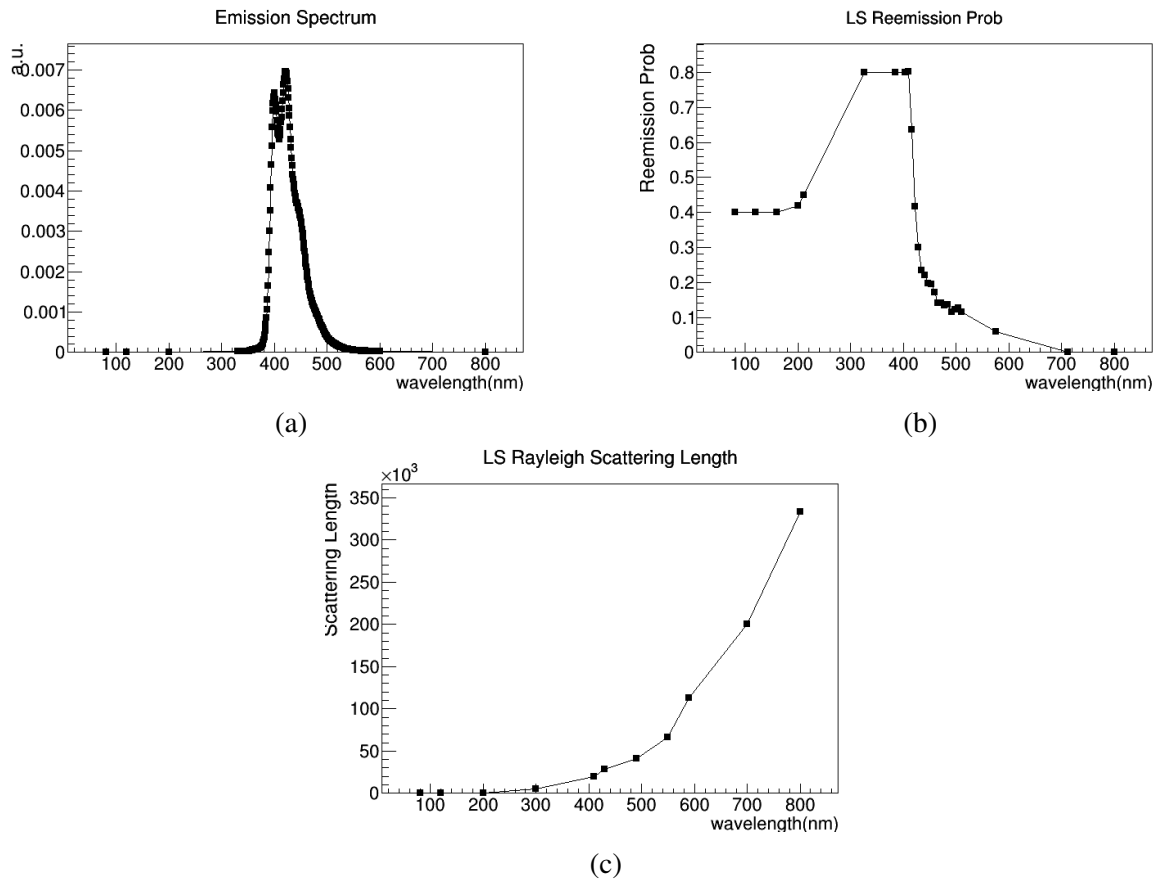


Figure 3.5: (a) is the emission spectrum of the liquid scintillator depending on the wavelength, (b) the reemission probability depending on the wavelength and (c) the rayleigh scattering length also depending on the wavelength. [33]

Table 3.6: The scintillation light decay times and corresponding weights, depending on the incident particle. [33]

Particle	fast [ns/(ratio)]	slow [ns/(ratio)]	slower [ns/(ratio)]
$\gamma, e+, e-$	4.93/(79.9%)	20.6/(17.1%)	190/(3.0%)
α	1.00/(65.0%)	35.0/(22.75%)	220/(12.25%)
N, P	1.00/(65.0%)	34.0/(23.1%)	220/(11.9%)

3.2.3 PMT model

In the simulation light detection determination consists of the quantum efficiency (QE) and collection efficiency (CE). The QE represents the conversion rate from a photon to an electron and the CE represents the the probability that the created electron is collected. Combined these make the detection efficiency (DE).

$$DE = QE(\lambda) \times CE(\Theta) \quad (3.3)$$

The $QE(\lambda)$ is given as a function of wavelength, while $CE(\Theta)$ depends on the latitude or position on the PMT surface. In the simulation the reflectivity of the optical surface is set to zero and depending on the $QE(\lambda)$, GEANT4 samples if an arriving photon is converted into an electron. After that, it is decided if the electron will be collected. The $CE(\Theta)$ takes into account where the photon hit the PMTs surface and it is sampled if the photoelectron is collected or not. An example for a PMT geometry in the JUNO simulation can be seen in figure 3.6.

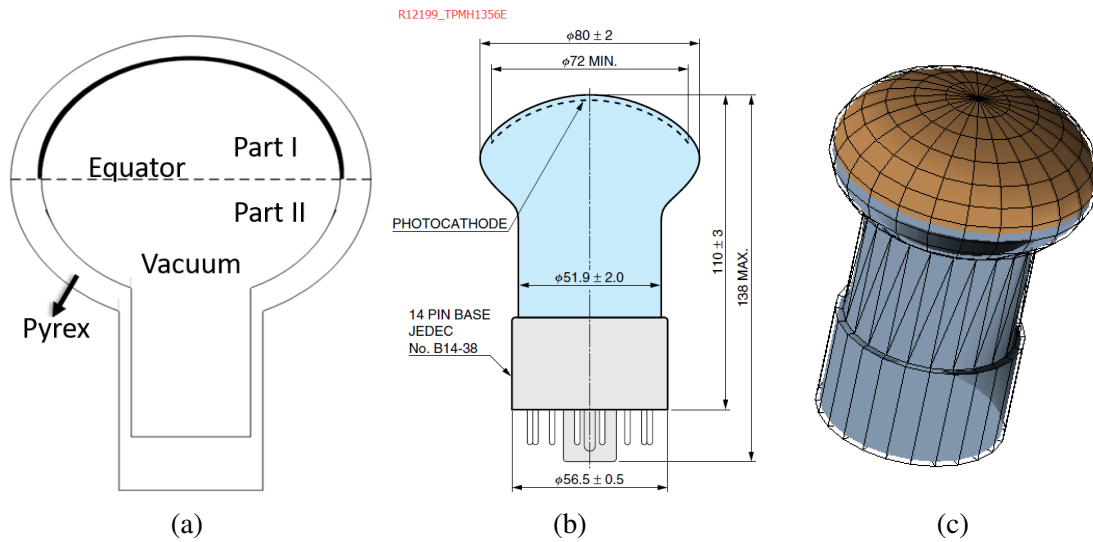


Figure 3.6: Example for a PMT implemented in the JUNO simulation. On the left the basic geometry for a PMT in the simulation. In the middle (b) the Hamamatsu R12199. The schematic is from [20]. On the right (c) a visualisation of the PMTs parts in the simulation, created by solid maker. [39]

There are several PMTs types implemented. The Hamamatsu R12199 is an example, but the general geometry setup and simulation process is the same. The PMT consists of one PMT body and two inner parts I and II. The optical surface is then attached to the inner volume I.

Chapter 4

Reconstruction

Reconstructing in particle physics is the procedure of determining the initial physical process from electronic signals produced by a detector and determining original parameters of particles, e.g. momenta, directions and the primary vertex, for an event. An event is the result of a fundamental interaction, which developed in a short time span at a confined region in space.

A *primary vertex reconstruction* is the reconstruction of the point in time and space, where and when the initial interaction happens. From here on the *primary* vertex is to assume. Many different events can happen in a liquid scintillator detector, but not all are of interest for the research that is performed. In other words, the registration that an event happened in the detector generally does not automatically mean it is wanted. Many events are considered as background and also the events of interest need to be further analysed. Therefore, a reconstruction for events is of the essence.

For an event starting inside the detector a reconstruction in a liquid scintillator detector will always determine the vertex. In the case of muons passing through, normally the entry and exit point is enough.

The common approach for reconstruction in a large unsegmented detector is a likelihood based system. The typical event energy for liquid scintillator detectors during neutrino events is a few MeV. These events have a point like energy deposition in the reconstruction, because the spatial resolution of the reconstruction is not enough to resolve events in the MeV range.

A general sequence for a likelihood approach could go as follows. For point like events a valid estimation for the vertex is the calculation of the charge barycenter. It can be calculated with equation (5.3). Then for that point in the detector and some area around it, quality factors are determined, which normally give indication of the likelihood that the vertex is at that position. Depending on the calculated probability for the different points, the most likely true vertex position is decided. If the new point is different from before, the calculation quality of factors starts again around the new point. Otherwise the most likely vertex position is found and additional verifications or important event parameters can be calculated, for an example the point in time when the event happened or the energy deposition.

The role of the vertex determination in LENA will be discussed next. After that the progress on vertex determination for JUNO will be annotated and the currently selected default vertex

reconstruction will be explained in more detail.

4.1 Reconstructions for LENA

Reconstructions for the LENA detector have been developed [29, 30], for HE events, utilizing likelihood and topological approaches. These can be used to discriminate muon background events. Especially one approach, a topological reconstruction for a broad energy range, is to emphasize, the *Novel Track Reconstruction* described in [40]. It holds the possibility of reconstructing dE/dx energy loss information, which could drastically reduce the exempt areas from muon passings and therefore increase the efficiency of the experiment.

4.1.1 Novel Track Reconstruction for LENA

This reconstruction works for HE events as well as for LE events. It aims to reconstruct the *spatial number density distribution of photon emissions*. At the current stage the reconstruction makes the following assumption:

- All light originates from the scintillation process.
- Individual emission times can be assigned to each photon.
- The initial particle travels with the speed of light.
- The initial particle travels in a straight line.
- A start point in time of the event is known.
- A start point in space of the event is known.

The last two points are currently provided by the MC truth, but the algorithm developed during this thesis aims to provide these in the future.

A very brief summery of the *Novel Track Reconstruction* will be stated next. An event broken down to a basic concept, is to assume a straight travelling particle that prompts scintillation photons along the way and these photons then being detected by the PMTs. A schematic can be seen in figure 4.1. Then for a spatial point x along the track the time t it takes a photon to be detected at point r_j is given by,

$$t(x) = t_{\text{ref}} \pm \frac{|x - r_{\text{ref}}|}{c_0} + \frac{|r_j - x|}{v_g(\mathcal{E})}, \quad (4.1)$$

where t_{ref} and r_{ref} are the reference points in time and space, currently given by the MC truth. c_0 is the speed of light and $v_g(\mathcal{E})$ is the group velocity of a photon in liquid scintillator. However, this equation simplifies to much. A more sophisticated version also considers the uncertainties

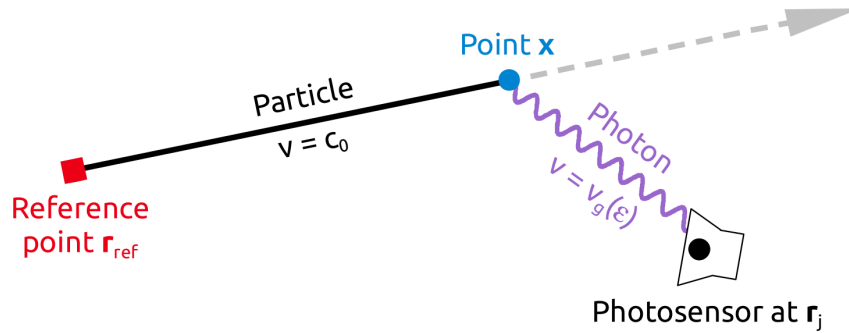


Figure 4.1: An illustration describing the basic principal of the *Novel Track Reconstruction*. A particle travels along a straight track with the speed of light and emits a photon at point x . Reference point r_{ref} and time t_{ref} will be provided by the developed vertex reconstruction in the near future. [40]

of photon emission and of detection times. The equation, which is considering these effects, is given by,

$$t(x) = t_{\text{ref}} \pm \frac{|x - r_{\text{ref}}|}{c_0} + t_{ph}(x, r_j) - t_s, \quad (4.2)$$

where $t_{ph}(x, r_j)$ replaces the fixed photon contribution and t_s is incorporating the uncertainties of photon emission and detection times. Hence, the corresponding p.d.f. $\Phi_{t_{ph}}$ includes the optical model of the liquid scintillator, of photon emission, propagation and detection [40]. The spatial p.d.f. $\Phi_{j,k}(x)$ is given by,

$$\Phi_{j,k}(x) = \omega_{j,k} \int_0^{\text{inf}} \tilde{\Phi}_{j,k}(\hat{t}(x; t_{ph} = t', t_s = 0)) \Phi_{t_{ph}}(t'; x, r_j) dt'. \quad (4.3)$$

This needs to be normalized for 1 hit and additional contributions like angular acceptance of the OM, photon scattering and absorption effects need to be considered. Then that is the *spatial number density distribution of detected scintillation photon emissions* $\Phi_{j,k}^*(x)$ for one detected photon. Because of the normalization of 1 hit, the number density distribution $\hat{\Gamma}_{\text{det},j}(x)$ for one photosensor j , can then be obtained by adding up as follows,

$$\hat{\Gamma}_{\text{det},j}(x) = \sum_{k=1}^{N_{\text{hits},j}} \Phi_{j,k}^*(x). \quad (4.4)$$

The reconstruct with all photosensors can be done with,

$$\hat{\Gamma}_{\text{det}}(x) = \sum_{j=1}^{N_{\text{PMT}}^{\text{hit}}} \hat{\Gamma}_{\text{det},j}(x). \quad (4.5)$$

This enables one to calculate the *spatial number density distribution of all emitted scintillation photons* $\hat{\Gamma}_{\text{em}}(x)$

$$\hat{\Gamma}_{\text{em}}(x) \equiv \sum_{j=1}^{N_{\text{PMT}}^{\text{hit}}} \hat{\Gamma}_{\text{em},j}(x) = \frac{1}{\varepsilon(x)} \sum_{j=1}^{N_{\text{PMT}}^{\text{hit}}} \hat{\Gamma}_{\text{det},j}(x), \quad (4.6)$$

where $\varepsilon(x)$ is the *local detection efficiency*. For a more in depth explanation take a look into reference [40].

4.2 Reconstructions for JUNO

At the moment there are 20 different reconstruction methods listed in the SNI_{PER} framework. There are also some reconstructions in development, which are not implemented in the framework yet. A large portion is devoted to LE reconstruction for neutrino physics and another large contribution is made by reconstructions for high energy muons. The list of reconstructions can be seen in table 4.1. These reconstructions are still in development and are subject to change and maybe even merge. Only some of the reconstructions are vertex reconstructions and some are for different parts of the detector. Most of them have a specific task or are slightly different copies of each other, with more specialization and improvements.

Table 4.1: List of reconstructions currently developed within the SNI_{PER} framework

BundleRecByChargeTool	PmtRec	RecRelease	SpmtMuonRecTool
Deconvolution	PoolMuonRecTool	RecSampleAlg	WaveFitAlg
IntegralPmtRec	PushAndPull	RecTimeLikeAlg	TemplateFitAlg
LsqMuonRecTool	QCtrRecAlg	RecWpMuonAlg	TTTracking
OMILREC	RecCdMuonAlg	SmartRec	VertexFitAlg

4.2.1 Low energy

At the current stage there are several reconstructions in development for the LE range. Some common approaches are based on already existing reconstructions from other unsegmented liquid scintillator experiments. These work well for point like energy depositions. Some of these have already been deployed and are implemented in the SNI_{PER}-framework. Examples for these are *RecTimeLikeAlg*, *SmartRec* and *PushAndPull*.

To have a comparison, for the developed reconstruction, the default reconstruction *RecTimeLikeAlg* [54] for JUNO is described. For a first guess on the positional vertex, the charge barycenter is calculated, e.g. with (5.3). From there the time residual function is calculated,

depending on the hit times of every PMT, as shown in equation (4.7),

$$t_{i,\text{res}} = t_i - \text{TOF}_i - t_0, \quad (4.7)$$

where t_i is the hit time of each PMT, TOF_i is the time of flight of the scintillation photon and t_0 is the real time of the event. The TOF can be calculated with,

$$\text{TOF}_i = \sum_{\alpha} \frac{L_{\alpha}(\vec{R}_0, \vec{R}_i)}{c_{\alpha}}, \quad (4.8)$$

where R_0 is the current guess for the event vertex, R_i is the position of the PMT i , L is the distance between R_0 and R_i , c is the speed of light and α stands for the different materials (scintillator, water). Hence, the residual time distribution is calculated by,

$$f(t_{i,\text{res}}) = \left(t_i - \sum_{\alpha} \frac{L_{\alpha}(\vec{R}_0, \vec{R}_i)}{c_{\alpha}} - t_0 \right). \quad (4.9)$$

The time likelihood function can be expressed as,

$$-\ln \mathcal{L} = -\sum_i f(t_{i,\text{res}}). \quad (4.10)$$

This is minimized over a 27 cube grid to find the time and position of the events vertex. If the same time and position is found the grid size is adjusted. This is iterated 100 times. After this the energy reconstruction is initiated. The likelihood function for charge minimization in *RecTimeLikeAlg* can be expressed as,

$$-\ln \mathcal{L}(E_{\text{vis}}; x_1, x_2, \dots, x_n) = -\sum_{i=1}^n \ln P(x_i | E_{\text{vis}}), \quad (4.11)$$

where the probability $P(x_i | E_{\text{vis}})$ of position x_i to hit the i th PMT is,

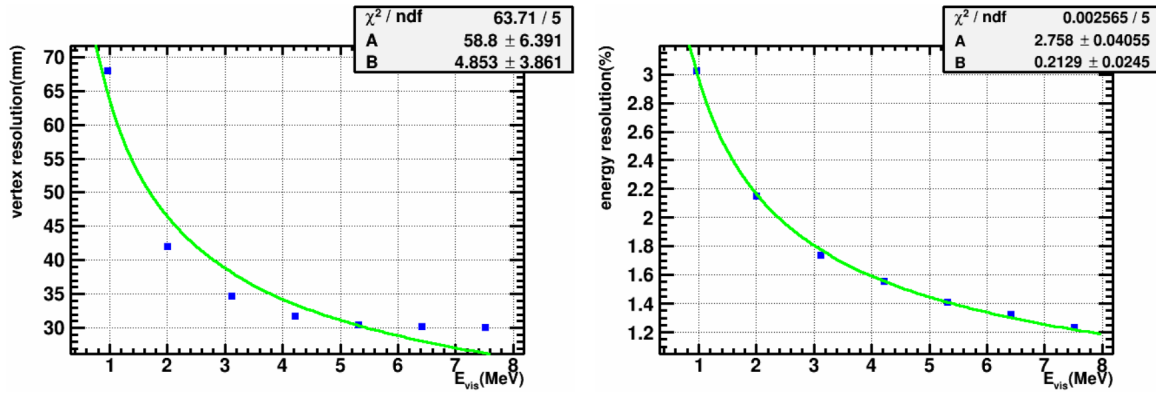
$$P(x_i | E_{\text{vis}}) = \frac{v_i^{x_i} e^{-v_i}}{x_i!} \quad (4.12)$$

and v_i is the expected number of photoelectrons given by,

$$v_i = Y E_{\text{vis}} \frac{\Omega(\vec{r}, \vec{R}_i)}{4\pi} \exp \left(-\frac{L_{\text{LS}}(\vec{r}, \vec{R}_i)}{\lambda_{\text{LS}}} - \frac{L_{\text{water}}(\vec{r}, \vec{R}_i)}{\lambda_{\text{water}}} \right), \quad (4.13)$$

where λ is the attenuation length for the medium. The function (4.13) consists of solid angle Ω acceptance and survival probability, but lacks PMT angle acceptance. By putting in equation (4.11) the position of the reconstructed vertex from equation (4.10) the energy of a point like event can be determine, with the *RecTimeLikeAlg* algorithm.

The performance of the default *RecTimeLikeAlg* in the center of the JUNO detector can be



(a) Vertex reconstruction resolution depending on energy of the initial particle. (b) Energy reconstruction resolution in % depending on energy of the initial particle.

Figure 4.2: The time and energy resolution depending on the energy of the incident particle. It was obtained simulating 10000 electrons in the center of the JUNO detector and reconstructing the events with the *RecTimeLikeAlg*. Average time to reconstruct one event is 5 seconds. These are preliminary results from the default reconstruction *RecTimeLikeAlg*, for LE events. [54]

seen in figure 4.2. The average distance of the reconstructed vertex to the MC true vertex is smaller than 10 cm in the range of 1 MeV to 8 MeV. This result has to be looked at cautiously, since all 10000 electron events, which have been used to obtain this result, were simulated right in the center, where symmetry effects can play an important role. Theoretically the center should have the worst resolution, since the fewest photons reach the PMTs uninterrupted from that position, but geometry effects have magnitudes greater influence on the result than photon counts in the energy range of more than 1 MeV. The time it takes to reconstruct one LE event with the *RecTimeLikeAlg* is about 5 seconds per event. These are preliminary results from the default reconstruction *RecTimeLikeAlg*, for LE events.

4.2.2 High energy

For the HE regime there are efforts being made to reconstruct muon tracks, but not necessarily to find the vertex. Instead these are used to reduce the dead time of the detector, by discriminating volumes of the detector which muons recently have passed and where they could have produced radioisotopes, like ^{10}C and ^{11}C .

Finding the vertex of high energy muons is not always possible, because it is very likely that these have been created way outside of the detector in atmospheric events. Track reconstruction are under development, namely *LsqMuonRecTool* and *ConeMuonRecTool* have shown promising preliminary results. A point that can be described as a vertex in these conditions is the point of entry of the tracks. This is commonly choose as the first hit PMT, which is likely to be directly hit, because of the high surface density of PMTs around the target volume in JUNO. So far no effort was being made to develop a vertex reconstruction for high energy events starting inside the detector.

The vertex reconstruction, developed in the course of this thesis and discussed in the next chapter, is the first to cover a wide energy spectrum for the JUNO detector and can even be applied to find high energy event vertices which are starting inside the target volume.

Chapter 5

The vertex reconstruction

5.1 Overview

In the course of this thesis, a vertex reconstruction method was developed. This approach utilizes primarily topological methods and is based on photon travel time estimates. It can in principle be applied to any unsegmented liquid scintillator detector, with any geometry. Like the *Novel Track Reconstruction*, which was shortly discussed in the chapter before this. The vertex reconstruction utilizes some of the same topological approaches.

In subsection 5.1.1 the goal of this vertex reconstruction is summarized. In the following subsection 5.1.2 the underlying principle is introduced. The next section 5.2 will in detail describe the realization of the reconstruction method.

5.1.1 The goal for this vertex reconstruction

The goal of this thesis was to develop a reliable method to determine the start position and time of events, with a wide energy range, utilizing some of the same methods already used in the *Novel Track Reconstruction Approach*. Additionally the time to determine these parameters should be as short as possible.

5.1.2 Underlying principle

Some expressions have to be clarified first. An *event* is a fundamental interaction, that developed in a short time span and a confined region in space. A *primary vertex* is the point in time and position where the first interaction of an event happened. The *time of flight* is the time it takes a photon to travel from its point of creation to the point of detection. The difference between time of flight and measured hit time $t_{i,dif}$ is given by

$$t_{i,dif} = t_i - \text{TOF}_i, \quad (5.1)$$

where i is the index for a detected photon, with t_i being the detection time of the photon hit i on a PMT. TOF_i is defined as:

$$\text{TOF}_i = \frac{L(x_0, x_i)}{c_{\text{LC}}}, \quad (5.2)$$

where TOF_i is the time of flight from photon emission point $x_i(0)$ to the detection position $x_i(t)$ and L is the distance. A scheme can be seen in figure 5.1

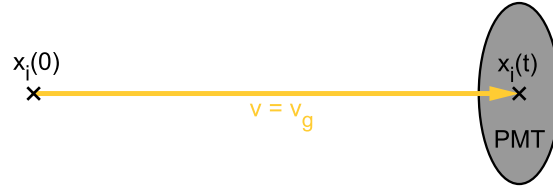


Figure 5.1: A schematic for time of flight. $x_i(0)$ is the photon emission position and $x_i(t)$ is the detection position. The photon travels along the yellow line with velocity v_g and hits a PMT.

c_{LC} is the group velocity v_g in liquid scintillator. Equation (5.2) is as simplification compared to reality, because in the LENA simulation only material with the refractive index of liquid scintillator is traversed by the photons from their creation till their detection and the refractive index is wavelength dependent in reality, but not in the LENA simulation.

For a position in the detector the time $t_{i,\text{dif}}$ can be calculated for every detected photon hit and the resulting time differences can be filled into a histogram. Examples for two of these *time difference histograms* (TDHs) can be seen in figure 5.2. (a) is calculated near the position of the

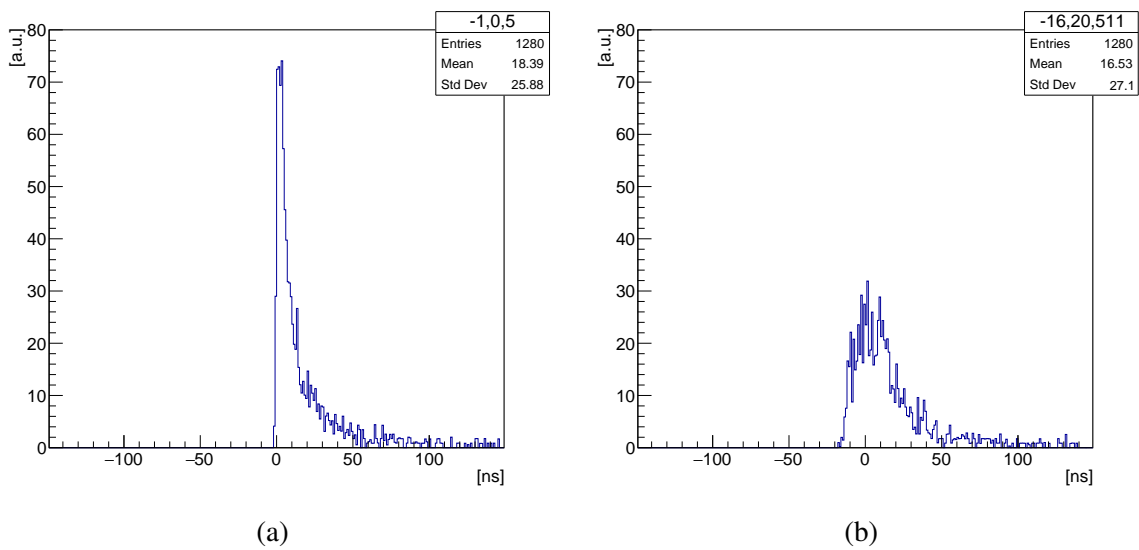


Figure 5.2: (a) a histogram calculated near the position of the true MC vertex. (b) is the a histogram for the same event calculated at a position about 5 m away from the true MC vertex. Both histograms have been calculated with equation (5.1) for a LE electron event in the center of the detector.

actual simulated vertex and (b) is calculated about 5 m away from it.

The main idea behind the vertex reconstruction is as follows: The TDH is calculated for different positions inside the detector. When light was emitted from a position, the TDH will show a clearly visible peak. For positions where no light has been emitted from, the TDH shows no peak or only a small peak. By iterating over different positions in the detector the event position is revealed.

A similar approach for a reconstruction was used in reference [63]. The same basic idea was used, but the vertex reconstruction in this thesis does not calculate the figure of merit used in reference [63] and attempts to find the primary vertex and not the track.

This basic idea is highly simplified in comparison to the real world. Different effects can alter the time of flight and not all photons that reach a PMT will be detected. While an event develops a photon can be emitted by the scintillator. The process from excitation of the scintillator, through wavelength shifting and emission is not instantaneous. The time it takes can be described by the decay components of the liquid scintillator. After this, the photon travels through the scintillator and in the case of JUNO, before it can reach the OM, it also has to transverse an acrylic sphere and water. During this travel time it is subject to absorption and scattering effects, which can alter the trajectory of a photon or lead to complete absorption. The *easy-to-estimate* direct path can be distorted and in the case of absorption without remission no information can be acquired at all. In the case that a photon does reach an OM it also has to be transformer into an electron. The probability for that is described by the QE of the PMT. A created photoelectron has to be collected to create a signal and the collection time of the PMT is also variable. An additional complication to find the vertex for GeV events is that most of the light detected will not be from the initial vertex, instead it will be emitted along the track.

There are some methods that try to compensate for the loss of information. For example the *Novel Track Reconstruction Approach* section 4.1.1, tries to approach these problems in reverse by describing the decay of scintillator, the survival of a photon on its trajectory and the acceptance of a photon by an OM, as probabilities. A *spatial number density distribution of all scintillation photon emissions* is calculated. A very detailed description of the different effects enable the reconstruction to calculate the course of event in great detail. But every method added also contributes to the execution time of the reconstruction. In summary, a very detailed reconstruction takes time.

On the other hand, maximum likelihood reconstructions do not explicitly try to compensate any of these effects. Instead, they find the parameters that maximize the likelihood of making the observation of given parameters. In reality the likelihood function, used to describe the connection between these parameter sets, often incorporates factors that do compensate the effects described above. In summary, a likelihood reconstruction may be fast, but is not explicitly considering the different effects that created the observed event data.

The developed vertex reconstruction is combining the best of both approaches, considering the crucial effects that lead to the observed event data, but not in all detail. Instead it uses the prior described most basic principle, which is similar to a likelihood approach and will

incorporate compensation methods, from the *Novel Track Reconstruction Approach*, in a way that is enhancing the results but does not create too much additional calculations.

By utilizing only the basic principle and minimal compensation methods the start position and time of an event can be provided, with no prior knowledge about the event. Also no geometrical symmetries of the detector are needed and the vertex reconstruction can therefore be applied to any unsegmented liquid scintillator detector. This is also true for the vertex reconstruction of HE events. Hence, this vertex reconstruction does not obstruct any of these same features described for the *Novel Track Reconstruction* in reference [40].

5.2 Implementation detail

The developed vertex reconstruction needs to be easily integrable into the *Novel Track Reconstruction*. Therefore, it utilizes the same software as the *Novel Track Reconstruction Approach*. Both use C++ as the main programming language and run on the *central processing unit* (CPU) of the computer. The vertex reconstruction also uses ROOT and BOOST C++ libraries [9, 60]. Furthermore, the libraries for the input and command line execution are the same as well. This makes it possible to integrate the developed vertex reconstruction by just copying the files into the *Novel Track Reconstruction* project code, so that both projects can be compiled and used as one application. Recent developments enable the *Novel Track Reconstruction* project to run parallelized in multiple threads, this feature was also added to the vertex reconstruction.

In the next sections the vertex reconstruction process will be described, while simultaneously explaining the used methods which make up this vertex reconstruction.

5.2.1 Charge barycenter

At the start of the vertex reconstruction, nothing is known about the event apart from the geometry of the detector and the hit times of photons, detected by the PMTs. For a LE event, the first estimate of the event position can be given by the charge barycenter. To calculate the charge barycenter the following formula can be used,

$$\vec{x} = \frac{\sum_{i=1}^n \vec{x}_i \cdot q_i}{\sum_{i=0} q_i}, \quad (5.3)$$

where \vec{x} is the position of the first estimate for the event vertex, \vec{x}_i is the position of the i -th PMT and q_i is the charge of the i -th PMT. Only the PMTs that actually have been hit are included in the sum. The charge q_i in the simulation can be given by adding up all detected hits of the i -th PMT, which is described by the following equation,

$$q_i = \sum_{j=1}^k h_j, \quad (5.4)$$

where h_j is the j -th hit on the i -th PMT. The sum j to k counts over all hits for the i -th PMT. For real event data, the collected charge of a PMT is related to the photoelectron hits and can be deduce. This can be used instead, as long as the PMT does not come close to saturation. The barycenter can also be calculated for HE events, but then this first estimate will give a point around the middle of the track and not the actual vertex of the event. How to deal with HE events will be further explained in section 5.2.7.

5.2.2 Position grid

The charge barycenter is a first estimate and can be calculated in milliseconds, but improvement is possible. The hit times of each hit can be utilized, to further reduce the distance of true vertex to reconstructed vertex. Other positions around the first estimate have to be considered. An organized way of doing this is a grid like structure. For each point on the grid, the TDH can be calculated, but doing that for a reasonably fine resolution of a few centimetres over the whole volume of the detector takes a lot of calculations. With the first estimate from the charge barycenter a grid consisting of $11 \times 11 \times 11$ points is constructed, for each of which the TDH is calculated. To determine the next estimate for the vertex, the TDH is constructed, which is shown in the next section. For now its enough to know a value is assigned to each point on the grid, which describe whether the grid point is close to the real vertex. A depiction of a 2 dimensional version of the grid can be seen in figure 5.3.

In the vertex reconstruction the grid is 3 dimensional. To get from a far grid position close to the true vertex an iteration is performed. During this iteration the grid is able to move around and the distance between the grid points can shrink. 11^3 TDHs have to be calculated for 1 iteration, but this number is far less than calculating TDHs on every point on a fine grid over the whole detector. The first estimate from the charge barycenter serves as the center for the first grid. When the calculation for all grid points is done, the point which is determined to be closest to the real vertex is chosen to be the center point for the next iteration. If the same center point is determined to be the center point for the next iteration the distance between the grid points is halved instead and a weighted barycenter from the grid values is calculated to determine the center for the next iteration. This process continues until the maximum resolution would be undershot for the next iteration. The starting distance between the grid points is 128 cm and the maximum resolution is set to 8 cm. A resolution finer than 8 cm did not enhance the results. For independence of the grid, from the first estimate, each time the resolution changes, a weighted barycenter of the grid values is calculated to determine the new center point. This also determines the reconstructed vertex in the end, when the maximum resolution would be undershot.

In order to reduce the execution time of the vertex reconstruction, the calculation of the TDHs for each grid point is parallelized. Calculating fewer TDHs than 11^3 also implies less calculations and therefore less execution time. Technically the grid, with the fewest points, which is still able to determine the change of the TDHs in each direction, has $2 \times 2 \times 2$ points

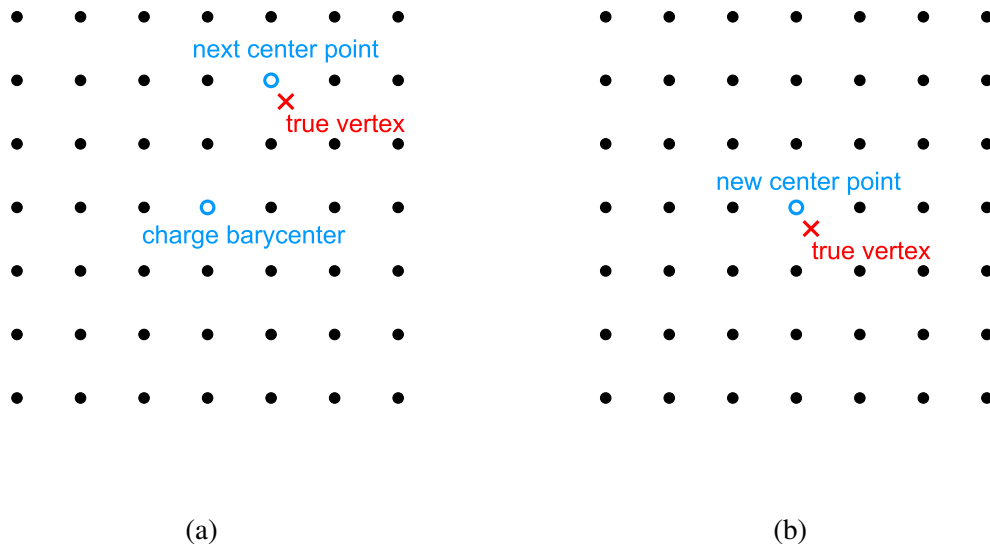


Figure 5.3: Layout of the grid. This example shows 7×7 grid points. The grid used in the software is 3 dimensional and has $11 \times 11 \times 11$ grid points. (a) The grid is initiated for the first time after the charge barycenter was determined. For the next iteration the center of the next grid is determined by the values assigned to each grid point, with the TDH. In this example the point closest to the true vertex is selected. (b) The next grid with a center near to the true vertex. If the center is determined to be also the center for the following iteration, instead the distance between the grid points will be halved and a weighted barycenter from the grid values is calculated, to determine the center for the next iteration.

around the center point. For a 3 dimensional world: $-X$, $+X$, $-Y$, $+Y$, $-Z$ and $+Z$. But the values determined for each grid point, through the TDHs, have local maxima. The grid needs to determine the global maximum. Therefore, a broader region was chosen to be analysed, to counter discontinues. The computer where this reconstruction was executed on had 12 cores. The grid was chosen to have $11 \times 11 \times 11$ points, because it was running fast and reliable with its CPU. Grid points, further away from the detector volume than $\frac{1}{2}\sqrt{\text{res}^2}$, where res is the current grid resolution, are not calculated. In the case of the grid moving to a new center point, some of the previously calculated grid points are calculated again and in principle these values could have been saved to be used again, but this case did not occur often and was therefore neglected.

5.2.3 Time difference histogram

An entry in the TDH can be calculated by determining the difference of time of flight to hit time of a photon on a PMT, using equation (5.1). Doing this for all photon hits creates TDH \mathcal{H} . Examples for the TDH can be seen in figure 5.2. When there are many entries near one time in the TDH, then it is probable that an event has taken place at that grid point. The TOF assumes instantaneous photon emission, a straight track from the emission position to the OM without and interactions and an instantaneous photon detection by the PMT. However,

the journey simulated for a photon does consider these effects, which generally results in an estimated TOF shorter than the actual TOF. Therefore, it is necessary to weight each hit and try to compensate the effects.

Different methods to weight photon hits will be discussed in the next two sections. A simple way to compensate scintillation decay times, scattering and absorption with remission is to only use first hits. Most of the first hits are not get scattered or absorbed and remitted and have been emitted during the short scintillator component decay. Also, less total hits mean less calculations to determine the TDH, but this also implies a loss of hits, which could have contributed valid information. For most of the results, presented in chapter 6, only first hits and angular acceptance have been taken into account. The different effects of first and full hit information will be discussed in chapter 6. The TDH calculated at the true vertex represents a superposition of photon emission times, delay times due to scattering and absorption and remission and the TTS of the PMTs. The TDH, at the vertex position, for a LE event, is expected to have the highest peak and shortest rise time.

The simplest way to determine the value V at a grid point from the TDH is to take the maximum value. However, compared to other methods, this does not yield the position reconstructed closest to the true vertex. Different approaches are possible. The Backtrack algorithm [63] suggests a figure of merit, integrating part of the TDH. The *RecTimeLikeAlg* calculates a likelihood function. Each of these could be implemented easily, but both of them take many more calculations than a simpler approach. Multiple algorithms have been implemented, into the vertex reconstruction, during this thesis. The obtained results have shown that the slope of the peak in the TDH yields the reconstruction of the vertex closest to the true vertex. To determine the slope a derivation of the TDH would be needed. This would require a fit of the TDH, which would take many calculations and therefore would massively increase execution time of the vertex reconstruction. Instead a much simpler method was chosen, which essentially finds the maximum slope. The method is described by the following equation,

$$V = \max_{j \in \mathbb{N}} \left\{ \sum_{i=2+j}^4 h_{\mathcal{H}i} - \sum_{i=-1+j}^1 h_{\mathcal{H}i} \right\}, \quad (5.5)$$

where $h_{\mathcal{H}i}$ is the value of weighted hits at the i -th nanosecond in the TDH \mathcal{H} . By adjusting j , this calculation is done for different points of the TDH. j is chosen to start at a few nanosecond bins before the event takes place. Then j is increased which shifts the equation (5.5) along the TDH. On its way along the nanosecond x axis the mean values $\frac{1}{3} \cdot (h_{\mathcal{H}j-1} + h_{\mathcal{H}j} + h_{\mathcal{H}j+1})$ and $\frac{1}{3}(h_{\mathcal{H}j+2} + h_{\mathcal{H}j+3} + h_{\mathcal{H}j+4})$ are calculated, to counter fluctuations. By subtracting these mean values, the slope between 3, 1 nanosecond bins is calculated. $\frac{1}{3}$ can be dragged out of the equation and is not performed, because dividing all results by $\frac{1}{3}$ does not affect the decision which V the maximum is, but would increase execution time. The maximum value V is assigned to the grid point.

5.2.4 Angular acceptance

Incorporating the angular acceptance has improved the vertex reconstruction results. The angular acceptance of an OM in LENA was simulated and the resulting graph can be seen in figure 3.2. The incident angle α of the photon on the OM is given by,

$$\cos \alpha = \frac{\vec{p} \cdot \vec{n}}{|\vec{p}| \cdot |\vec{n}|}, \quad (5.6)$$

where \vec{p} is the vector from a grid point to the OM and \vec{n} is the normal vector facing onto the optical surface. The incident angle α can be used to look up the angular acceptance from the histogram 3.2.

To have no lookup table loading time, the histogram was replaced by 3 simple functions,

$$\begin{aligned} P_1 &= \alpha^2 + 0.145 \alpha + 0.86, \\ P_2 &= \cos(9.13 \alpha - 5.5)0.42 + 0.42, \\ P_3 &= \cos(0.736 \alpha - 2.5)127 + 127, \end{aligned} \quad (5.7)$$

where α is the incident angle of the photon on the OM. The probability P_1 is valid for a range of α from 0 to 0.6 rad, P_2 describes the probability from 0.6 to 0.75 rad and P_3 is valid for the range of α being between 0.75 to 0.87 rad. If the incident angle α is bigger than 0.87 rad the angular acceptance probability is set to 0. The resulting OM angular acceptance graph can be seen in figure 5.4. The produced graph does not match the histogram 3.2 in all detail, but fluctuations

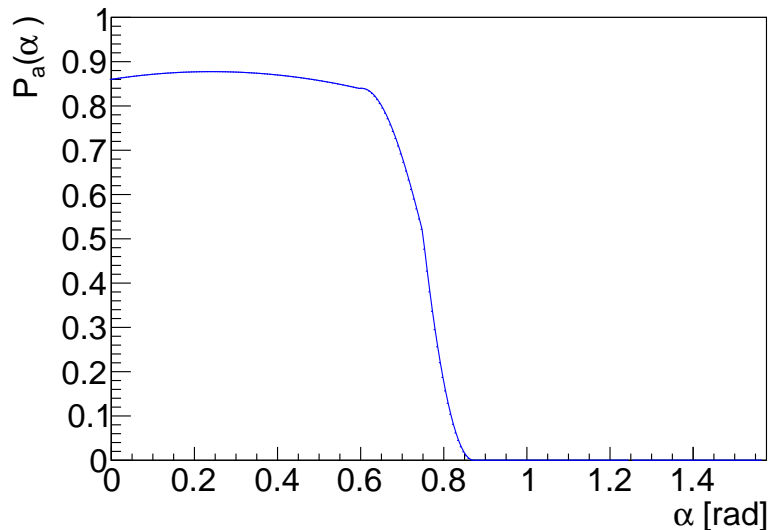


Figure 5.4: Graph resulting from the 3 functions (5.7). The functions are used to determine the angular acceptance. The value of α determines which function is valid. The probability is calculated in combination with the angle α . The graph is approximating the Winston cone acceptance histogram 3.2, which is part of a lookup table in the *Novel Track Reconstruction*.

in histogram 3.2 are far greater than any discrepancies. Therefore, this is not worsening the results. It is to note that the probability for an angle greater than 0.87 rad is not 0 in the original histogram. This is a result of the simulation that generated the original histogram. Photons that have been scattered or reflected multiple times could be detected by the OM, but these photons will have a delayed TOF and could worsen the reconstruction results. Therefore, the probability is set to 0 instead, which essentially weights hits that could arrive at the OM under these angles with 0 in the TDH.

5.2.5 Additional light weighting and evaluation

Additional methods that determine the probability that light from the vertex is detected have been investigated. Two of these, which are considered to improve reconstruction the most, are the *survival probability* and the *hit probability*.

Survival probability The survival probability $P_{\text{surv}}(d)$ states the probability that a detected photon has travelled a certain distance without being scattered or absorbed. It considers scattering and absorption effects. The equation is as follows,

$$P_{\text{surv}}(d) = \exp\left(-\frac{d}{A_L}\right), \quad (5.8)$$

where d is the distance and A_L is the attenuation length. The attenuation length A_L can be calculated by,

$$A_L = \frac{1}{\frac{1}{L_{\text{abs}}} + \frac{1}{L_{\text{sct}}}}, \quad (5.9)$$

where L_{abs} is the mean absorption length and L_{sct} is the mean scattering length. Figure 5.5 shows the survival probability $P_{\text{surv}}(d)$. During the reconstruction, the wavelength of the detected photons is unknown. Therefore, the mean expected wavelength of 430 nm is chosen instead.

Hit probability The hit probability $P_{\text{hit}}(d, \alpha)$ determines how probable it is that a scintillation photon is emitted into a solid angle, which is occupied by the effective optical surface of an OM, at a distance d and orientation α . The approximative function that is used is given by

$$P_{\text{hit}}(d, \alpha) = \frac{r^2 \cos \alpha}{4d^2}, \quad (5.10)$$

where r is the effective radius of the optical surface. Figure 5.6 shows equation (5.10) for the range of the incident angle α 0 to $\pi/2$ rad and distance d from 0 to 1 m. Only the near field is shown to highlight, that this approximation is not correct for the area close to the OM.

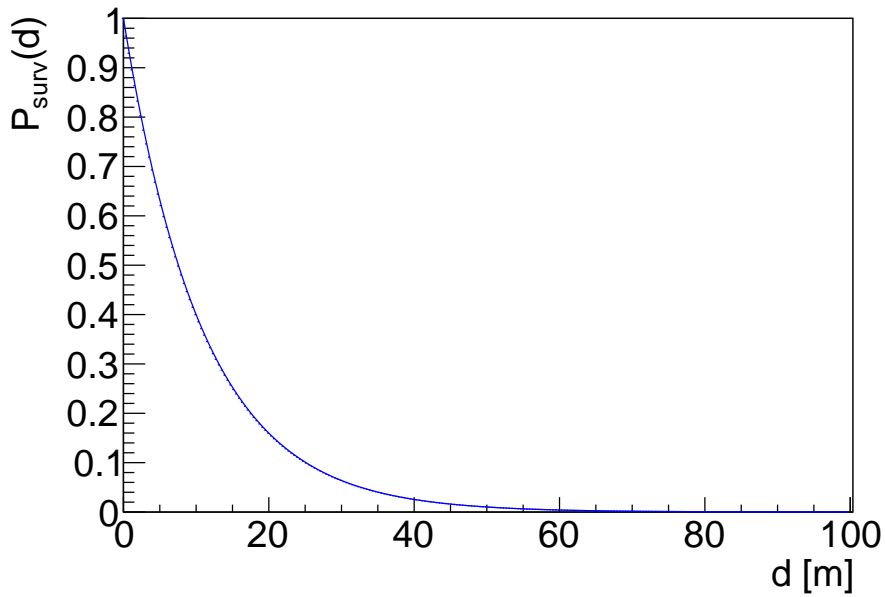


Figure 5.5: The survival probability $P_{\text{surv}}(d)$, generated with equation (5.8). The attenuation length A_L has been calculated with the values from table 3.3. The scattering and absorption length are wavelength dependent in a real experiment, but in the reconstruction the wavelength of the photons is unknown.

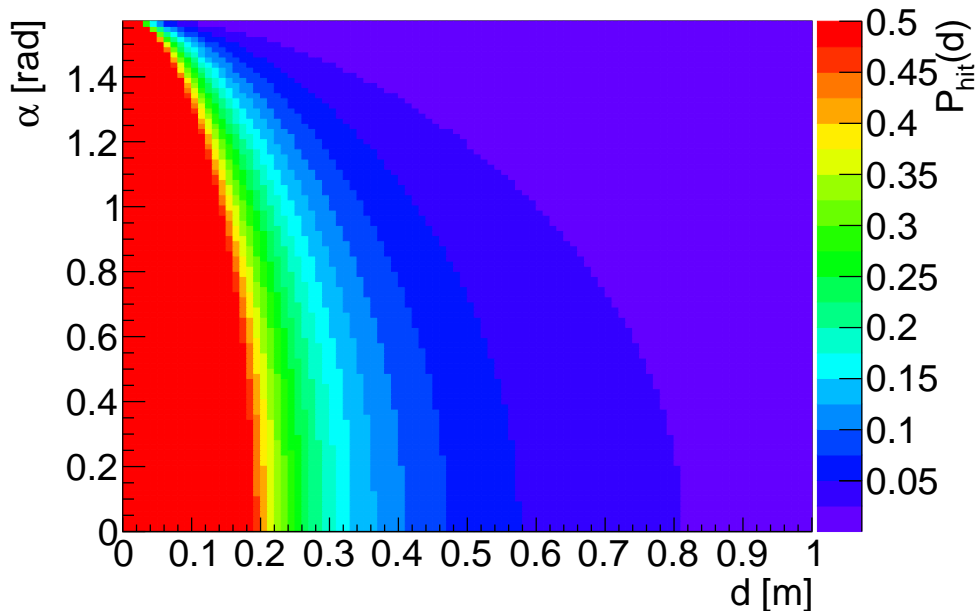


Figure 5.6: The hit probability $P_{\text{hit}}(d, \alpha)$ calculated by the approximative function (5.10). The near field of the OM from a distance d 0 m up to 1 m is shown, to highlight the overestimation near the OM. Areas where the approximation would reach values greater than 0.5 are capped. Otherwise the probability would reach infinity near 0 m.

5.2.6 Time fitting and evaluation algorithm

After the position of the primary vertex is reconstructed, the time t_{start} when the event started can be calculated. It can be done with the following formula for LE events,

$$t_{\text{start}} = \frac{1}{n} \cdot \sum_{i=0}^n \{\text{TOF}_i - t_i\} . \quad (5.11)$$

The time of flight TOF_i is calculated with equation (5.2) and t_i is the hit time of each detected photon. If all photons would be emitted instantaneous, travel along a straight line and the detection would be instantaneous as well, the same time difference would be calculated for each detected hit. But the formula (5.11) is an approximation, because scintillator emission times, scatter and absorbed and reemission effects and TTS of the PMT are implemented in the simulation. For real experimental data also additional effects from the electronics would contribute. In the simulation the TDH, calculated at the vertex, contains a superposition of these effects.

To improve the reconstruction of the event start time t_{start} , the scintillation decay distribution and the time resolution of the PMTs can be compensated. Scattering and absorption with reemission effects are not compensated. For LE events a *time evaluation histogram* TEH is calculated by filling it with the time differences from TOF and each detected photon hit. It is basically an inverted TDH without weighting any hits and only calculated at the reconstructed vertex. The inversion is done, because fitting the scintillation decay component times is simpler and to be able to distinguish TDHs and TEHs. The time difference for the TEH are calculated by,

$$t_{i,\text{-dif}} = \text{TOF}_i - t_i , \quad i \in \mathbb{N} . \quad (5.12)$$

The TEH mainly follows the combination of the decay time components of the liquid scintillator¹ and the time resolution of the PMTs² (neglecting scattered and absorbed light). This is only valid for LE events at the true vertex. A fit is performed based on the scintillator decay time components and their weights. An example for a TEH and a corresponding fit can be seen in figure 5.7.

The fit equation $f(s, t_{\text{start}})$ is given by,

$$f(s, t_{\text{start}}) = \sum_{c=1}^3 \frac{s w_c}{2 t_c} \cdot \exp \left(\frac{1}{t_c} \left((t_{\text{start}} - t_i) + \frac{t_{\text{pmtr}}^2}{2 t_c} \right) \right) \cdot \left(1 + \text{erf} \left\{ \left((t_i - t_{\text{start}}) - \frac{t_{\text{pmtr}}^2}{t_c} \right) \cdot \frac{1}{\sqrt{2} t_{\text{pmtr}}} \right\} \right) , \quad (5.13)$$

where signal strength s and event start time t_{start} are the free parameters. t_c is the mean decay

¹Decay time components of the liquid scintillator for LENA, stated in table 3.3

²LENA PMT simulation in section 3.1.3

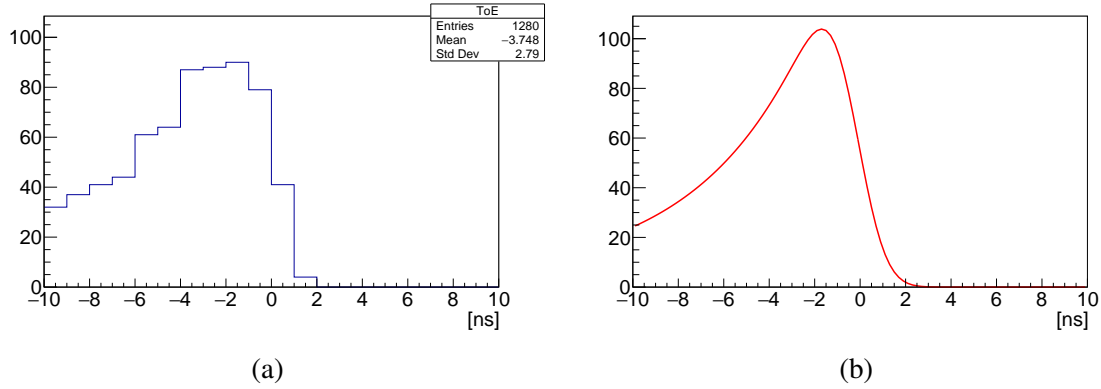


Figure 5.7: (a) is an example for the TEH, the entries are calculated by the equation (5.12). (b) is the corresponding fit from equation (5.13). This was a LE electron event in the detector center, with an energy of 5 MeV.

time of the scintillator component c . w_c is the weight of the scintillator component³. t_{pmt} is the time resolution of the PMT⁴.

The p-value is calculated, from χ^2 of the fit and the number of degrees of freedom (ndf), to test the hypothesis that a LE event was reconstructed. For a more robust reconstruction result a energy reconstruction is needed, but this was sufficient as a first evaluation method.

For HE events the start time can not be found in this way, because the events are not point like and most of the photons will be emitted from the track of an HE event and not from the vertex. However, if it is possible to only use photons that have been emitted at the vertex, it is possible to do this time reconstruction for HE events. How to determine which photons have been emitted from the vertex is discussed in the next section.

5.2.7 Direction determination and HE algorithm

The LE event vertex reconstruction, as described in the sections before, can also be applied to HE events when only photon hits from the initial vertex are considered. Such hits can be found by determining the direction of a track in a HE event.

Figure 5.8 shows the light front emitted by the vertex and the light front emitted by the track. Some of the first hits in a detector will always origin from the vertex, if the vertex is inside the detector. If the direction of the track can be determined, the OMs which have first hits from the vertex can be determined as well.

When the vertex reconstruction is used without any information of the event it will deliver a point near the track middle. An additional energy reconstruction or the p-value obtained from the TEH fit 5.2.6 can be used to determine if the event is a HE event. Stated next is, how to use the track direction and a point near the track as a first estimate, to identify OMs with first hits from the primary vertex. The LE reconstruction is performed again, using only the first hits that are considered to origin from the vertex. This will move the currently estimated vertex along

³Decay time components of the liquid scintillator for LENA, stated in table 3.3

⁴LENA PMT simulation in section 3.1.3

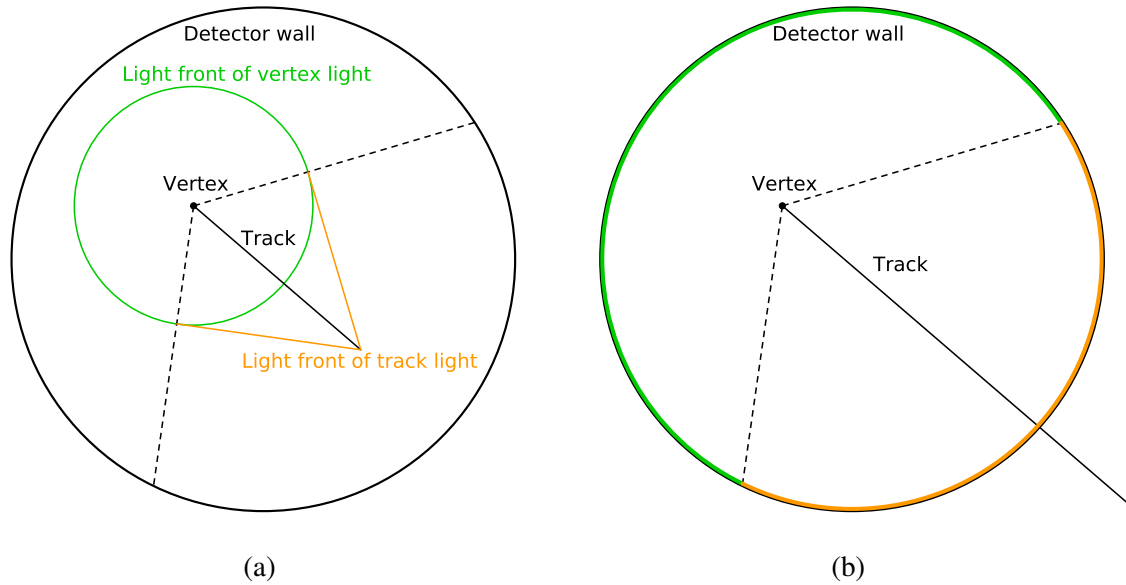


Figure 5.8: Figure (a) shows a schematic snapshot of a developing HE event. The light fronts propagate towards the detector wall. In figure (b), the HE particle left the detector and the areas where the OMs have first hits from the vertex (green) and where from the track (orange) have been marked.

the track in the direction of the true vertex. This process can be iterated, till the reconstructed vertex stops changing its position, then the reconstructed vertex is at the position of the the true HE event vertex.

To determine the OMs with first hits from the track light front, the solid angle Ω can be estimated. The opening angle α_{Ω} , of Ω is given by,

$$\alpha_{\Omega} = 2 \cdot \cos\left(\frac{1}{n_{LS}}\right), \quad (5.14)$$

where n_{LS} is the refractive index for the liquid scintillator. The mean expected wavelength is taken for the refractive index. It is assumed that the particle is travelling with the speed of light.

Determining a direction Determining a direction of a particle with only a point near the middle of the track can be achieved by looking at TOF differences. It is assumed that the HE particle is travelling with the speed of light. It will reach an OM in the direction that it is travelling faster than a photon that started with the particle at the vertex and is travelling in the same direction. The calculated TOF for the photon will be longer than the measured first hit time. For an optical module perpendicular to the track on the level of the vertex the calculated TOF and the first hit time of the OM should show no significant difference. As a rule of thumb, the shorter the actual hit time of an OM is compared to the calculated photon TOF from the vertex, the more likely it is that that is the direction the HE particle travelled in.

A problem is that the actual vertex is unknown, but what is known is a point near the middle of the track. Depending on where the vertex is assumed to be, the established rule of thumb

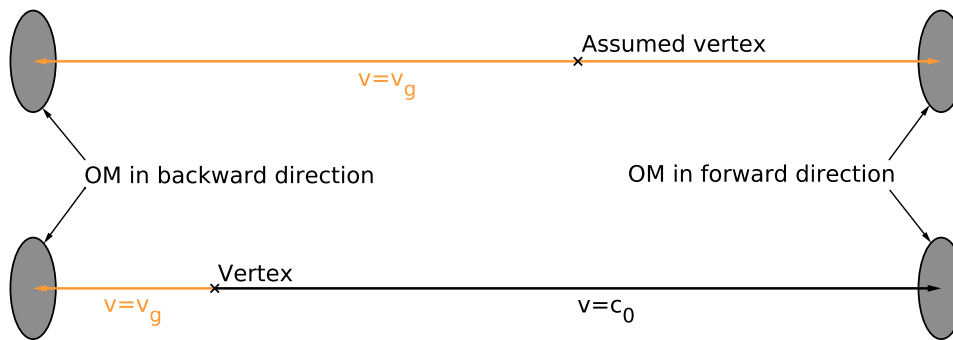


Figure 5.9: A schematic explaining the differences in calculated time of flight and actual first hit time. The upper panel is the assumed situation with light traveling along the track with velocity v_g . The lower panel is the actual event. In this case there would be a difference in calculated time of flight and first hit time in the backwards direction.

might not be valid, but for the backwards direction the same difference in calculated time of flight and hit time appears. This happens because a photon from the actual vertex has to travel only a fraction of the distance, that is assumed from the middle of the track. A schematic of these effect can be seen in figure 5.9. No matter which point on the track is assumed, there will always be either the difference⁵, in the backwards direction or in the forward direction or both, but never no difference⁵. A way to prove this is to assume there would be no difference in time for the backwards direction, which means the assumed vertex is on the actual vertex, but then there will be a difference in the forward direction because the particle and the photon have to travel the same distance and the photon velocity v_g is smaller than the particle velocity c_0 . Moving the assumed vertex along the track would then create a difference in time of flight and hit time for the backwards direction.

In the reconstruction the TOF is calculated from the assumed vertex to all OMs and the first hit times are subtracted. The mean direction where the largest differences emerge are found. Most of the time 2 directions almost perpendicular are found and sometimes only one is found. Which of the directions is the forward and which the backward direction is unknown at first, but can be determined. The next section will describe how the forward direction is found.

Finding the forward direction To determine which of the directions the forward direction of the particle track is, 2 TDH are calculated, at the estimated vertex position. But this time only first hits from OMs outside the solid angle Ω are taken into account. For the histograms both directions (A and B) are assumed to be forward. The first TDH is calculated with the solid angle Ω opening in direction A and the second TDH is calculated with the solid angle Ω opening in direction B. 2 example histograms for directions A and B are shown in figure 5.10. The vertex reconstruction finds the excess of first hit photons with originate from the track and

⁵The difference in calculated photon TOF and actual hit time.

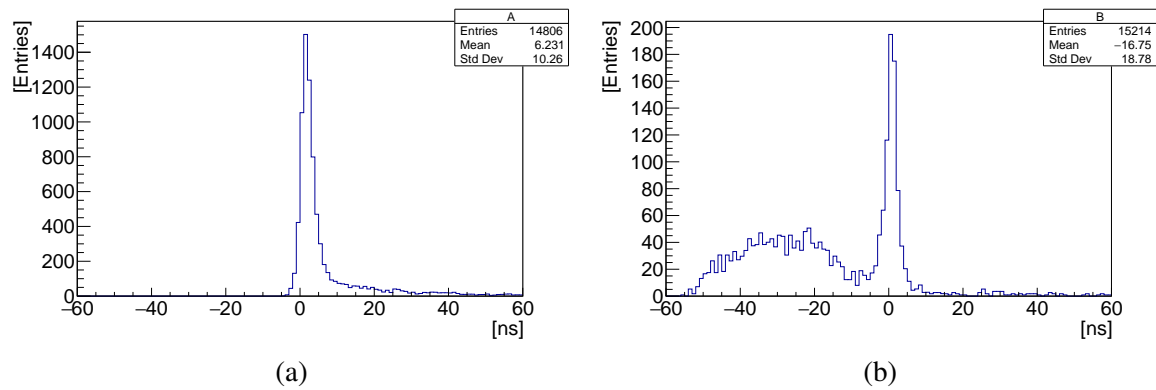


Figure 5.10: Example histograms for the direction finding for a 7.2 GeV muon event. Both directions are assumed as forward. (a) was correctly assumed as forward, because there is a clear peak with a bit of scattered light to the right. (b) was falsely assumed to be forward. Hence, the first hits from the track appear as a negative time difference to the left of the peak.

determines the forward direction. The excess of first hits is found by determining the distance in nanosecond between the first entry and the maximum entry in the histogram. For data with dark current a threshold can be defined, to determine the first entry. In this example the direction A which was used to generate the diagram A was the forward direction of the track.

Chapter 6

Results of the vertex reconstruction

In this chapter the performance of the developed vertex reconstruction is discussed. The first section will be about the results of the simulation in the LENA detector and the second section will show as an example of the reconstruction used for the JUNO detector.

6.1 LENA-Detector

6.1.1 Low energy

As an example for LE, the reconstruction of a simulated 6.7 MeV electron is discussed. Projections can be seen in figure 6.1. The center axis of the cylinder of the LENA detector is orientated

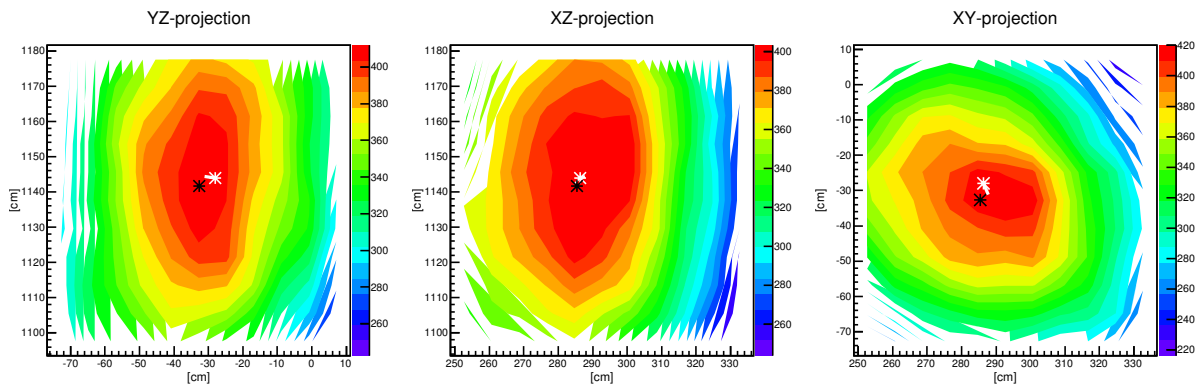


Figure 6.1: Example for a reconstruction result. A 6.7 MeV electron was reconstructed. Projections for 3 directions are shown. The black cross marks the reconstructed vertex position and the white cross is the simulated vertex. The small white line marks the distance between start and end point of the initial particle. For the projection the grid values V in that direction have been added up to a depth of 24 cm. The distance of reconstructed vertex to simulated vertex is 5.33 cm.

in along the Z axis. The projections show the final grid iteration, with the values¹ V for each 8 cm bin added up through the projection depth of 24 cm. The black mark shows the position of

¹Value V is determined by equation (5.5)

the reconstructed vertex and the white mark is the position of the true vertex. The true vertex was simulated at 2.86 m in X, -0.28 m in Y and 11.43 m in Z direction. The distance from the reconstructed vertex to the true vertex is 5.33 cm. The time it took to reconstruct the events by the algorithm was about 0.5 seconds, with 12 Intel Xenon X5650 CPUs with 2.67 GHz each. For this and all other simulations that have been reconstructed for this thesis the start time of the event is set to 0 ns and the same CPUs have been used. 0 ns was chosen for simplicity and could have been any value. The event start time was reconstructed to be 0.7 ns. No dark current was generated in any of the simulations. In principle the reconstruction should work also with dark current, but it has not been tested yet. The hits have been weighted with the angular acceptance, but not with the survival probability or hit probability. Results utilizing the survival probability and hit probability will be discussed in the paragraph 6.1.1.

The statistical possible positional resolution depends on the amount of light that has been detected. An equation approximating the statistical possible resolution r_{stat} is given by,

$$r_{\text{stat}} = t_c \frac{c_0}{\sqrt{n/3}}, \quad (6.1)$$

where t_c is the time of the fastest scintillator decay component and n is the number of detected photoelectrons. The number of detected photoelectrons is divided by 3, because of 3 dimensions. The actual resolution in X, Y and Z depends on the amount of hits containing information for that direction. As an example suggest a LE event in the middle of the LENA detector. Only a few photons will reach the caps and most of the detected photons will be around the same elevation. Hence, the information provided for the Z coordinate will be more distorted by scattering and absorption effects, than the information about X and Y of the event. Additionally not all scintillation light will decay via the fast component, which is assumed for the equation (6.1). The approximated possible resolution r_{stat} for the example event is 5.45 cm.

Position To evaluate the performance of the vertex reconstruction a sample of 10k electron events has been produced and reconstructed. The original position and direction were randomly distributed in a cylinder with radius 13.5 m and the full target height of 96.0 m inside the center of the LENA detector. The kinetic energy of the initial electrons ranges from 0.5 MeV up to 10.0 MeV. All 10k events are separated solitary events.

The reconstruction of these events took about 0.5 seconds on average. The result of the positional reconstruction can be seen in figure 6.2. About 92% of the events could be reconstructed within a maximal distance of 50 cm to the simulated vertex. The black graph represents the average approximated possible resolution r_{stat} for that energy.

The position of the reconstructed event vertex distance distribution can serve as an indicator for the possible reconstruction performance in LENA. For the best result the maximum should be coincide with the black line, then no positional improvement with the given statistical boundaries is possible. The maximum of the distribution is shifted about 2 cm to the right. This can have multiple reasons, one major reason is, that only first hits have been used for this recon-

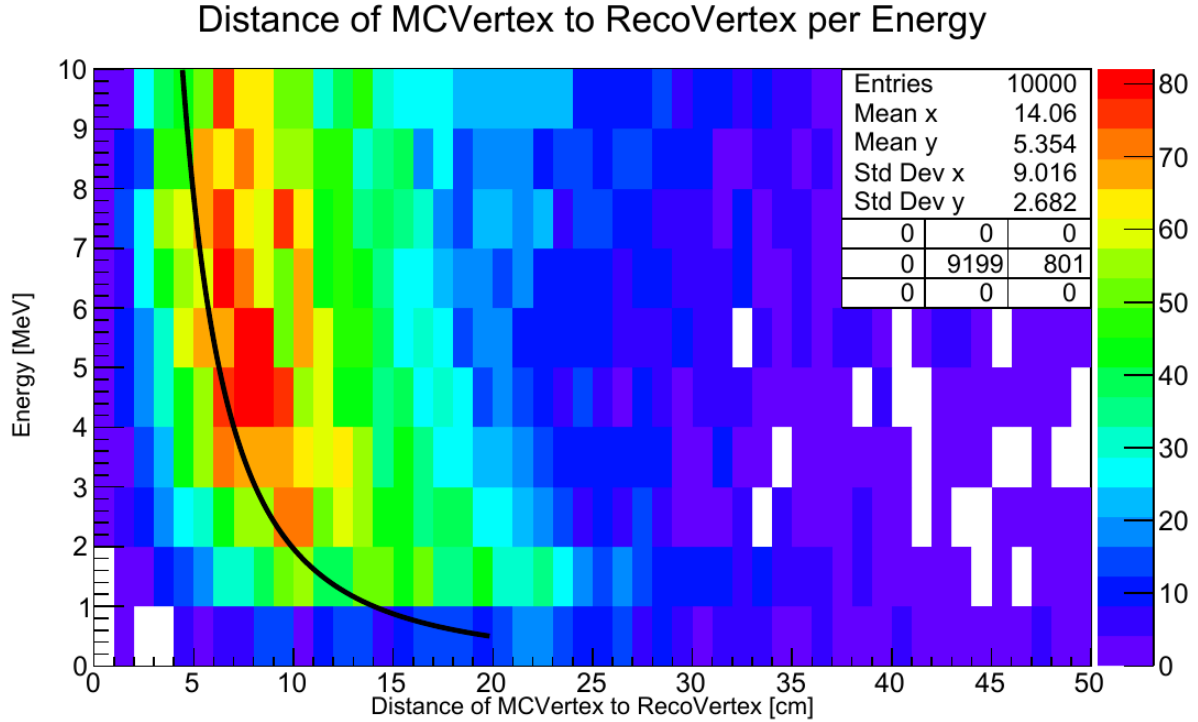


Figure 6.2: Reconstruction result for 10k electron events, with a random start position in a cylinder with radius 13.5 m inside the detector. The kinetic energy of the initial electrons ranged from 0.5 MeV to 10.0 MeV. The black graph is the average approximated possible resolution r_{stat} .

struction, instead of using all available hit information. The simplification that the photons are emitted instantaneously, travel without interaction and are detected instantaneously as well, is contributing and the negligence of survival probability and hit probability could be accountable.

The LE position reconstruction resolution has been analysed. Figure 6.3 shows the distance of the reconstructed vertex to the simulated vertex in X direction (upper panel), in Y direction (middle panel) and in Z direction (lower panel). A normal distribution is expected for each direction. The results show a superposition of different normal distributions. A reason for this is the simulated energy range. With higher energies more photons will be emitted and can be detected. Therefore, more information about the event is available and the position can be determined more precise. Because of the cylinder geometry there is less information available in the Z dimension. As expected the resolution in Z direction is the worst, for LE events, with a standard deviation of ± 10.35 cm. The standard deviation in X direction is ± 7.00 cm and in Y direction ± 7.04 cm. The combination for all directions is given by,

$$\sigma_{x,y,z} = \sqrt{\sigma_x^2 + \sigma_y^2 + \sigma_z^2} = 14.34 \text{ cm} . \quad (6.2)$$

The vertex position for 10k electron events, with an energy ranging from 0.5 MeV up to 10 MeV, was determined with a standard deviation of ± 14.34 cm.

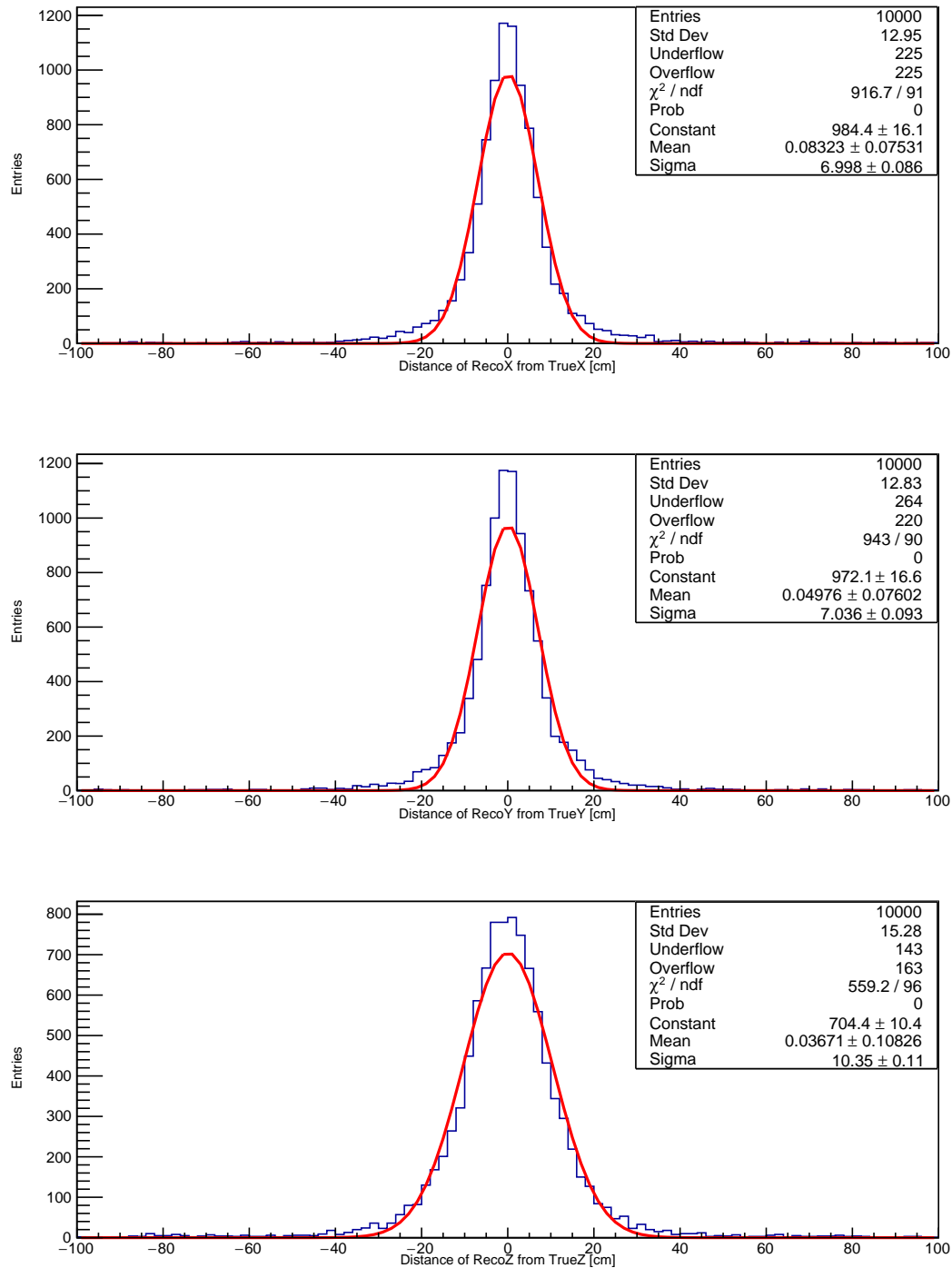


Figure 6.3: Position reconstruction resolution for LE events. The difference in each direction of true vertex to reconstructed vertex is shown, for 10k reconstructed LE events. A Gaussian distribution is fitted for each direction, because a normal distribution is expected. The resolution in X direction is ± 7.00 cm, in Y direction ± 7.04 cm and in Z direction ± 10.35 cm.

The LE vertex position reconstruction has been further analysed. In figure 6.4 the difference of reconstructed vertex to simulated vertex is shown, depending on the distance from the detector wall. One can see that the maximum is around 7.5 cm for a distance greater than 4 m.

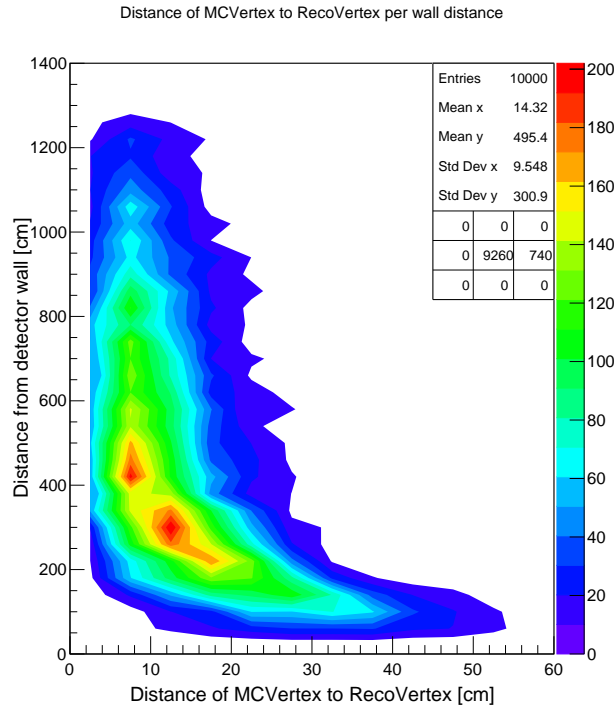


Figure 6.4: Reconstruction of 10k simulated LE electron events in the LENA detector, as a dependence of detector wall distance. The kinetic energy of the initial electrons ranged from 0.5 MeV to 10.0 MeV. First hits and angular acceptance was used for this reconstruction.

Closer to the edge of the detector the maximum shifts up to 40 cm. Away from the detector center there is less symmetry in the event detection. The reason for the worse reconstruction near the detector wall is the approximation, that the photons are emitter instantaneously, do not interact on the their way to the OMs and are detected instantaneously. This leads to a mismatch between estimated TOF and actual photon travel time. Around the center of the detector this mismatch can relativize because of the symmetry, but near the edge of the detector the effect emerges. To further expose these effects the radial distance in the XY-layer is shown in figure 6.5. To generate the radial distance, the radii in XY-direction of the simulated vertex and the reconstructed vertex have been calculated. On the x-axis of the figure 6.5 the reconstructed vertex radius has been subtracted from the simulated vertex radius. In figure 6.5(a) only first hits have been used for the reconstruction and in figure 6.5 (b) full hit information has been utilized. The reconstruction with first hits shows that the closer the simulated vertex is to the edge of the detector, the more the reconstructed vertex is found to be shifted closer to the detector edge. For the reconstruction with full hit information the opposite happens. The closer the simulated vertex is to the edge, the further away from the edge the reconstructed vertex will be shifted. For the reconstruction (a), the first hits on the other side of the detector arrive later than expected.

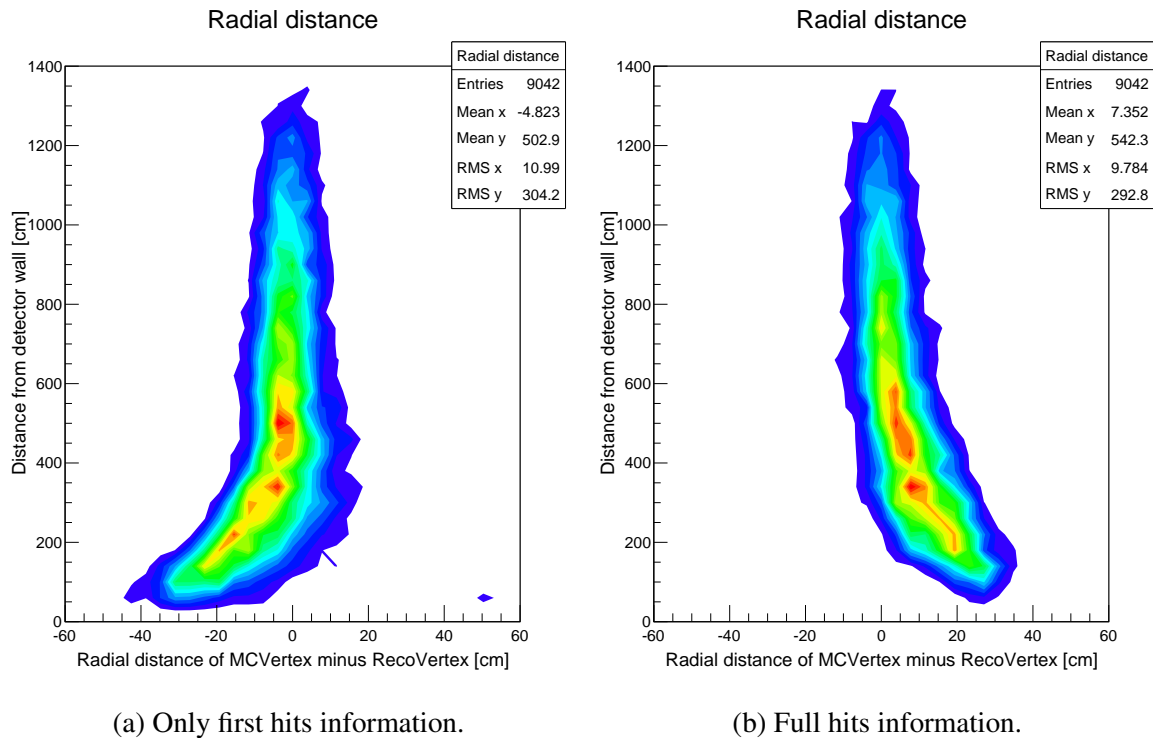


Figure 6.5: Radial distance from detector wall. The radial distance in XY-direction of the simulated vertex to the reconstructed vertex have been calculated. In figure (a) the vertex reconstruction used only first hit information and in (b) full hit information has been utilized. The number of entries is not 10k because vertices that have been simulated closer to any on the caps than the wall of the detector are not used in this analysis.

For a distance of 25 m only about 10% of the photons are not absorbed or scattered (see figure 5.5), which does not mean that 90% do not arrive, instead they are delayed and their direction is distorted. The reconstruction still considers those hits as not delayed, because only the angular acceptance was used to evaluate the hits. In case (b) (full hits), the detected light was emitted over the full scintillation decay time spectrum, which gives a delay and secondly more scattered and absorbed and reemitted light is considered, which holds even more of a delay. The effect is that the reconstructed vertex is shifted to the middle of the detector. For case (a) the vertex is shifted to the edge of the detector, because the delayed photons detected on the other side of the detector are overestimated. The few hits on the other side can push the vertex, because they are considered equally likely as the hits on the side with the event and the number of considered hits on the side with the event is reduced by only using first hit information.

In summary: In general TOFs are estimated to short. In case (a) (first hits), the first hit on the other side of the detector arrive delayed, are overvalued and there is only minimal *counterpressure* from only first hits on the event detector side. In case (b) (full hits), the hits on the other side are still delayed and overvalued, but more hits on the side of the detector with the event, can not only compensate that, but overshoot. They overshoot, because to short estimated TOFs shift the reconstruction away from any OMs.

The use of the survival probability (5.8) weighting the photon hits has been performed. An example event can be seen in figure 6.6. The visible features do not differ much from a re-

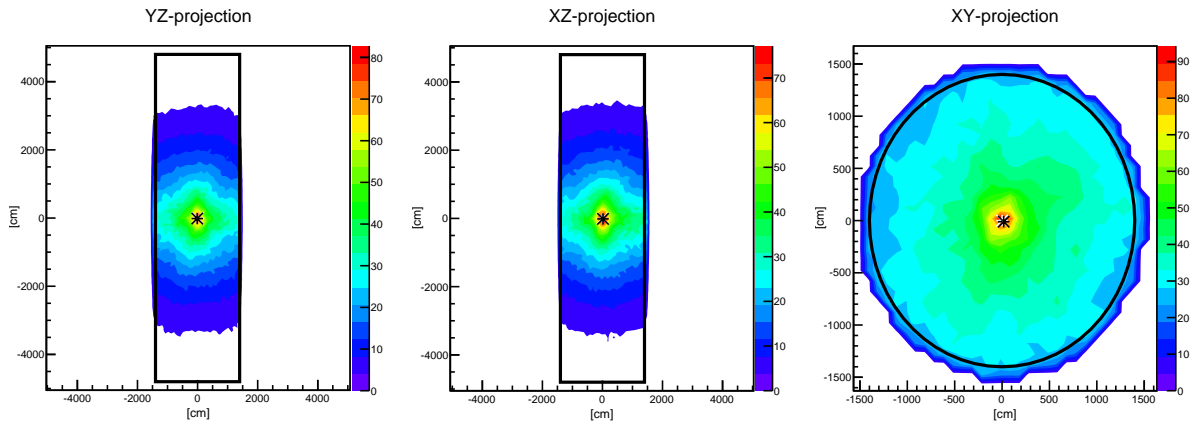


Figure 6.6: Example event for a reconstruction performed with angle acceptance and survival probability. The simulated vertex is at the center of the detector. To be able to see the effects of the survival probability the whole detector has been divided into grid points of 1 m distance. The event was a 5 MeV electron.

construction done without the survival probability, but attempts to use the survival probability equation (5.8) to weight detected hits have not enhanced the reconstruction. For events a few meter apart from the symmetry axis the vertex was shifted towards the detector center. Not as much as reconstructions with the hit probability, which will be discussed next, but still worsening the results compared to reconstructions without the survival probability.

The main reason why the utilization of the survival probability failed, is that it weights the hit with the probability, that they reach a point without interacting. This is only partly of what is needed for the reconstruction. Scattered light also reaches the OMs and would be weighted with the probability of being not scattered. This light is delayed and the direction is distorted. What actually would be needed is the combination of the survival probability with an extension, that determines the probability of scattered and absorbed and reemitted light, reaching the OMs. Furthermore the TOF needs an extension to distribute a detected hit over time, to consider delay effects. Then the survival probability would contribute to enhance the results.

Weighting photons with the hit probability (5.10) has also been conducted. It can determine the probability that a photon emitted in a random direction will be emitted in the direction, that is occupied by the photosensitive area of an OM. An example event can be seen in figure 6.7. One can see very high probability near the detector edge. The example event was positioned in the center of the detector. Therefore, symmetry effects of the detector enabled the reconstruction to correctly reconstruct the event in the center of the detector. The use of hit probability with events a few meters away from the center axis have failed and shifted the reconstructed vertex to one of the OMs.

The main reason why the utilization of the hit probability has failed is that, it is an approximation. It overestimates shorter distances. Furthermore without any prior knowledge of the event all positions in the detector are equally likely to have the event happen at that position.

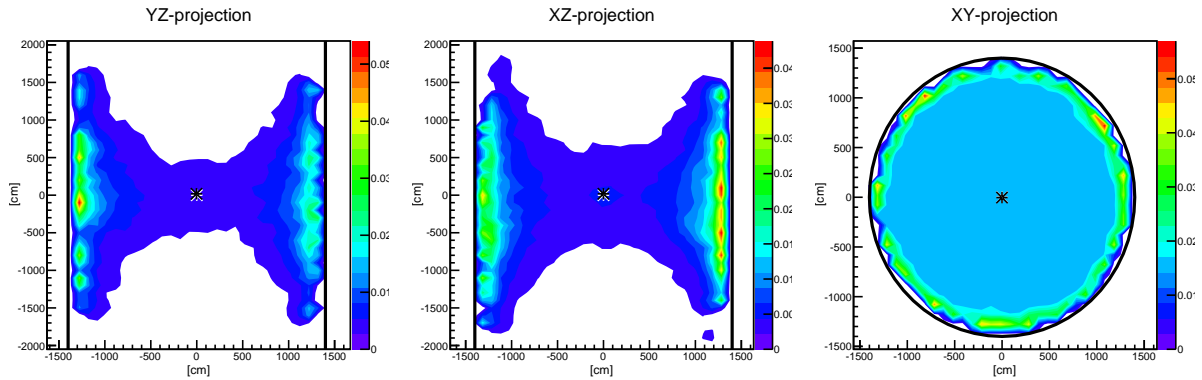


Figure 6.7: Example event for the reconstruction of a 5 MeV electron in the center of the detector. The angular acceptance and hit probability have been used. To be able to see the effects of the hit probability the whole detector has been divided into grid points of 1 m distance.

By using the hit probability approximation, points near OMs would suddenly be more likely to have events happen there, which is not true.

Time The result for LE event start time reconstruction can be seen in figure 6.8. The sample of events are 10k electron events in the energy range from 0.5 MeV up to 10 MeV. The position is randomly distributed within a cylinder with radius of 13.5 m and the full target height of 96.0 m inside the center of the LENA detector. The start time of the simulated events is 0 ns. Because the time reconstruction is only done when the position of the vertex is found, the result is highly dependent on how close the reconstructed vertex is to the simulated one. For the event start time reconstruction figure only vertices that have been reconstructed within 20 cm from the simulated vertex have been considered. A Gaussian distribution around the simulated event time of 0 ns is expected. Hence, a Gaussian distribution was fitted to the result. The mean value is -0.21 ns. An excess can be seen to negative times. This is the result of underestimated TOFs. The fit in the TEH will compensate scintillation decay time and the PMT time resolution, but not the delay of absorption with reemission and the scattering of light. In the TEH these hits are shifter to the negative side, which can be understood with equation (5.12). Hence, the fit will also be shifted to negative times. The time resolution for the event start is ± 0.33 ns. But this result has to be noted with care, because of the mean value shift of -0.21 ns.

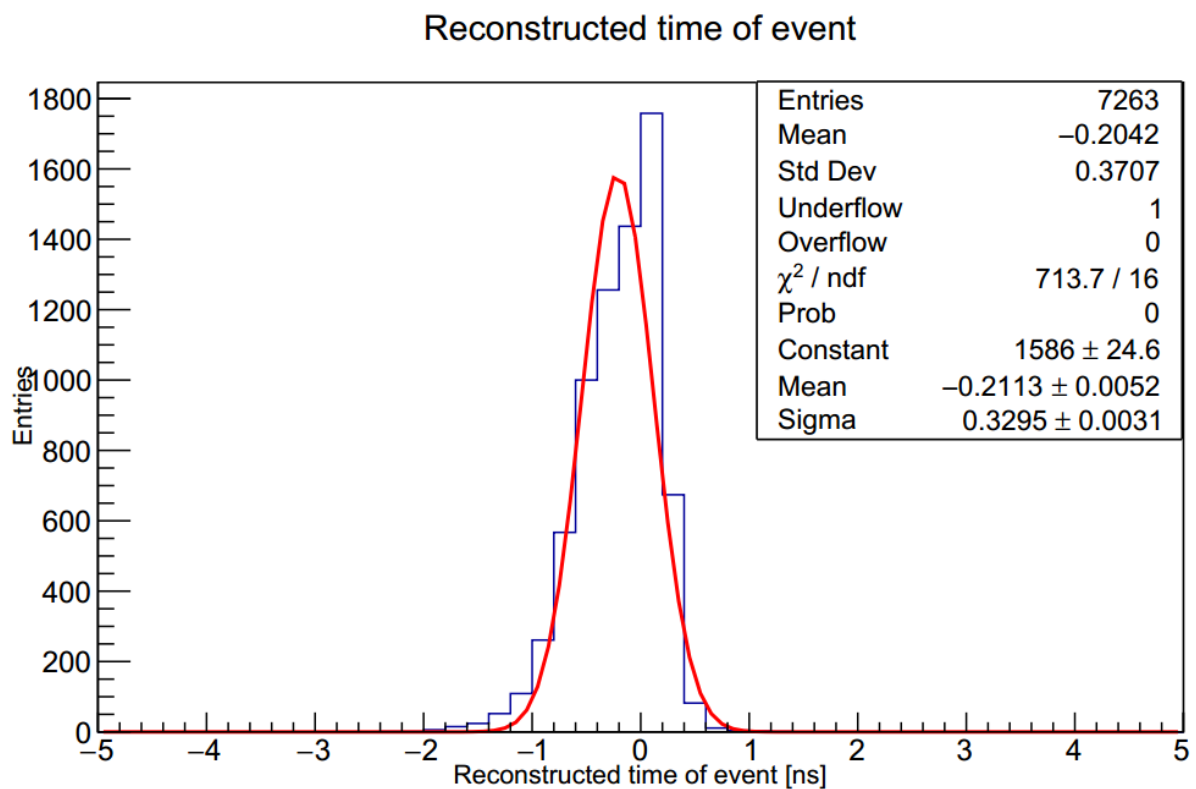


Figure 6.8: Reconstructed time for electron events in the energy range from 0.5 MeV up to 10 MeV. Simulated sample event start time is 0 ns. The time reconstruction is executed when the position of the vertex is reconstructed and the quality is depending on how close the reconstructed vertex is from the simulated one. Therefore, only vertices that have been reconstructed closer than 20 cm to the true vertex are considered for this figure.

6.1.2 High energy

For the HE vertex reconstruction a sample of 2500 muons was used. The events are contained inside the detector volume and have an energy range from 5 GeV up to 10 GeV. An example for a HE muon event reconstruction can be seen in figure 6.13. The reconstruction of a muon,

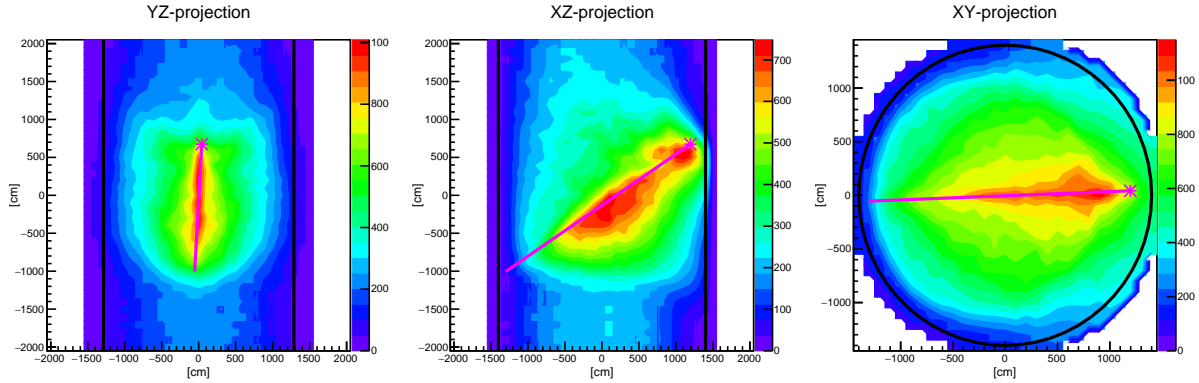


Figure 6.9: Example reconstruction for a HE event. The first iteration of a muon, with an energy of 5.8 GeV. To be able to see the whole track the reconstruction grid was extended over the whole detector. The position of the true vertex is at the pink marker and the track of the particle is marked with a pink line. The projection adds the grid point values V up in a slice depth of 10 m.

with an energy of 5.8 GeV. The first iteration, which was altered to display the whole detector by setting the first estimate in to the center and expanding the grid over the whole detector. The grid values² V are added up in the projection, by a slice depth of 10 m. The first iteration for HE events is done as if it would be a LE event. The fit of the TEH determines a very low p-value, which will reject the hypothesis that it this is a LE event. The process to determine the primary vertex for a HE event is executed, as described in section 5.2.7. A final HE vertex reconstruction result can be seen in figure 6.13, which will be discussed later in the next paragraph.

Position & time resolution The distance of reconstructed vertex to simulated vertex and the determined event start time can be seen in figure 6.10. The statistical possible resolution r_{stat} is smaller for HE events, because of more photons that are emitted and therefore more can be detected. Hence, there is more information about the event available. But also more scattered and absorbed and reemitted light will be detected. This makes it more difficult to reach that resolution. For the developed vertex reconstruction the statistical possible resolution is not obtainable without further development. The main reason for this is that only first hits are used in the HE vertex reconstruction. The p-value from the TEH fit was used, to determine if a HE reconstruction is needed. 2073 of 2500 events have been identified correctly as HE events. For a more consistent determination an energy reconstruction needs to be done. The reconstructed event start time resolution is ± 0.27 ns. The mean time reconstruction for HE events is not around the 0 ns, which has been simulated. The reason for this is the underestimated TOFs. The same

²Value V is determined by equation (5.5)

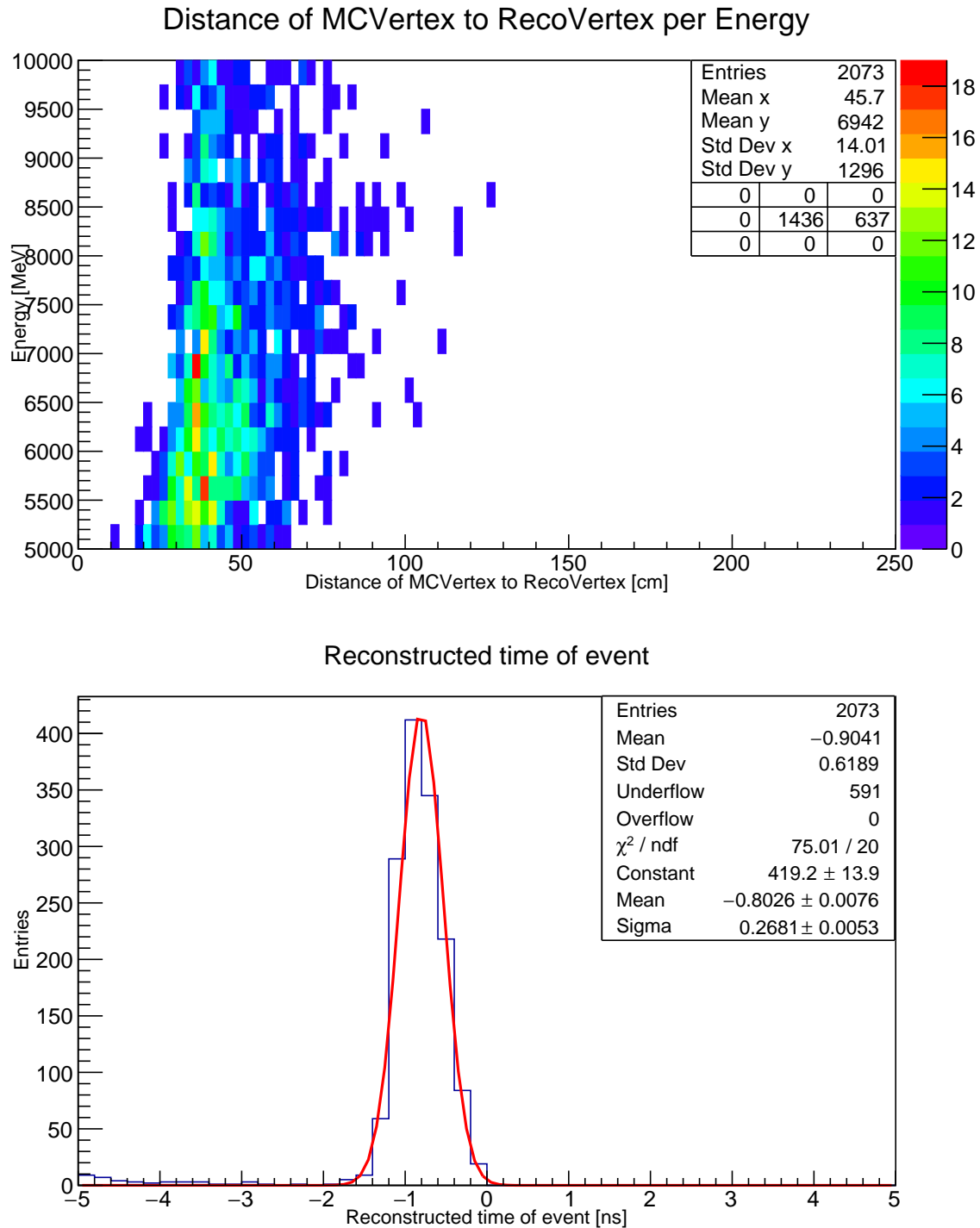


Figure 6.10: HE event vertex reconstruction. Upper part distance of reconstructed vertex to simulated vertex, depending on kinetic energy of initial particle. Lower part the event start time reconstruction. The simulated event start time for this sample is 0 ns. The algorithm depends on the p-value of the TEH fit, to determine a HE event. Only the 2073 events that have correctly been identified as HE events were used for this figure. Initially 2500 muon events have been reconstructed, with an energy range from 5 GeV up to 10 GeV.

reason as for the LE applies, but with even more scattered light and light from the track, the event times get reconstructed even more in the negative time range. Additionally and the actual main reason for the time difference is that the vertex position has been reconstructed about 30 cm away from the simulated vertex. This this can be seen in the upper panel of figure 6.10, where the most of reconstructed vertices have been reconstructed 30 cm away from the true vertices. The 30 cm shift is even more apparent in figure 6.11. The distance of reconstructed vertex to true vertex in X and Y direction follow a normal distribution, which is not the case in Z direction. This can be explained by the sample of 2500 muon events and that the reconstructed vertices are actually shifted along the track direction of the particles. The track direction of the muon events is initially random, but only contained muon events have been selected into the sample of these 2500 muon events. Contained events start and end inside the detector and because the LENA detector is a cylinder, the sample is bias towards tracks that generally go up or down the cylinder. Very few tracks in this sample stay at one height and go across the X-Y level. This lets the shift of the vertex along the track become apparent fir the Z direction.

To show that the reconstructed vertex is actually shifted about 30 cm along the track direction, the closest point on the track to the reconstructed vertex has been determines and the distance of that point to the true vertex has be plotted. The result is shown in figure 6.12. The mean value for the shift along the track direction is 30.4 cm. As an example, the final iteration of a 6.7 GeV muon is shown in figure 6.13. The reconstructed vertex was reconstructed close to the true particle track. the distance from the reconstructed vertex to the true vertex is about 35 cm.

The reason why the reconstructed vertex is shifted along the track for HE events is partly due to the underestimated TOFs and party to the exclusion of OM in the direction of the track. The TOF is underestimated, because it is neglected that the scintillation light is not emitted instantaneous, the light travelling through the scintillator is subject to absorption with reemission and scattering and the light is not detected instantaneous. Therefore, a TDH further away from the majority of OMs will create a higher value V , because the difference of TOFs and measured hit times match closer to one time in the TDH. This creates as higher peak and shorter rise time and therefore the higher slop, which the value V represents. By excluding all OMs in solid angle Ω , which are in the direction of the track, less *counterpressure* exists in the direction of the track and the vertex shifts along the track direction. A second reason could be first hits from the track that have falsely been taken into account do to a mismatch of reconstructed direction and true particle direction.

To get a value how close the vertex is reconstructed to the track, the nearest point on the track for each reconstructed vertex is found and the distance, between that point and the reconstructed vertex in each direction, is calculated. The result can be seen in figure 6.14. The distribution in Z direction does not completely follow a normal distribution. This is probably caused by the bias of contained muon sample. The sigma value for X and Y direction are greater than in figure 6.11. This might be a hit that the reconstructed vertices are also shifted towards the detector center and can also be explained by underestimated TOFs. The standard deviation for the determination of the track distance in X direction is ± 21.61 cm, in Y direction ± 21.65 cm

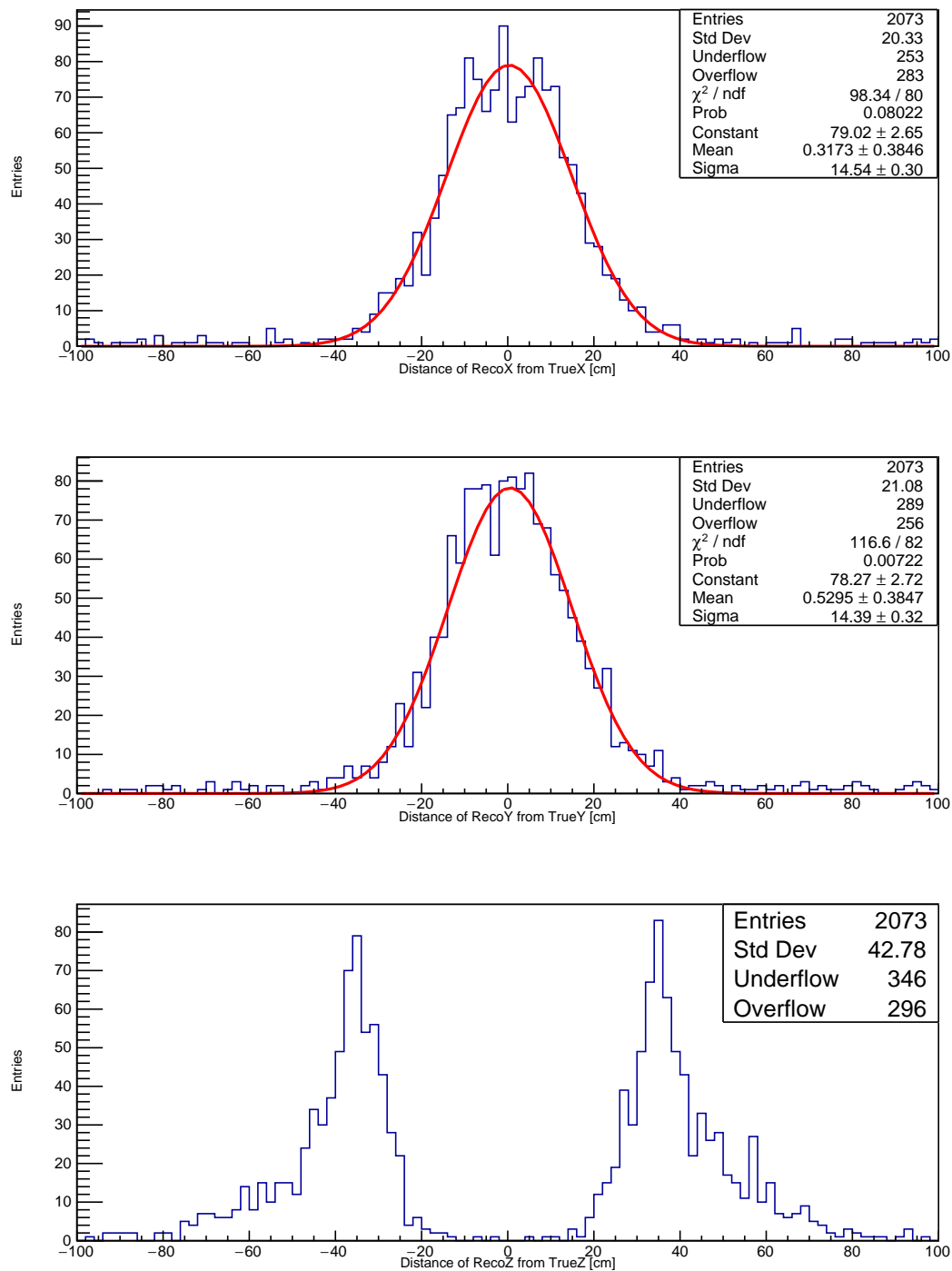


Figure 6.11: Distance in each direction reconstructed vertex to true vertex. The X and Y directions shows a normal distribution, but the Z direction does not. The reason is, the reconstructed vertex is shifted about 30 cm along the track and the muon sample is bias. The sample mostly contains events that generally go along the Z axis of the detector, which makes the shifted vertex visible.

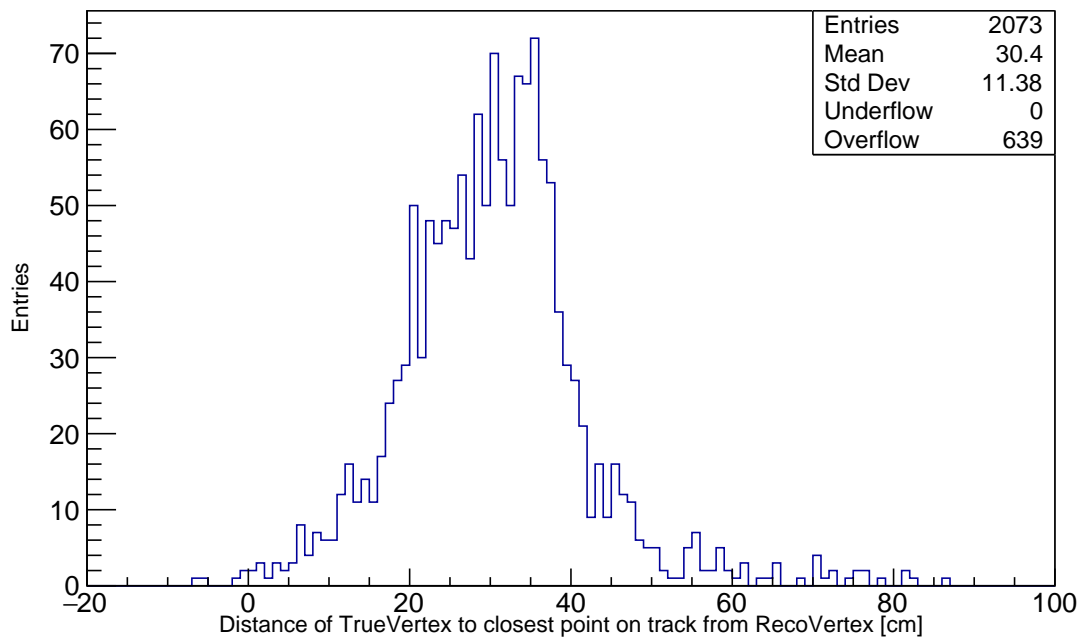


Figure 6.12: The shift of HE event reconstructed vertex. The closest point on the track to the reconstructed vertex was calculated and the distance from that point to the true vertex has been determined. The mean value is 30.4 cm. The true vertex is at 0 and the track proceeds in positive x direction.

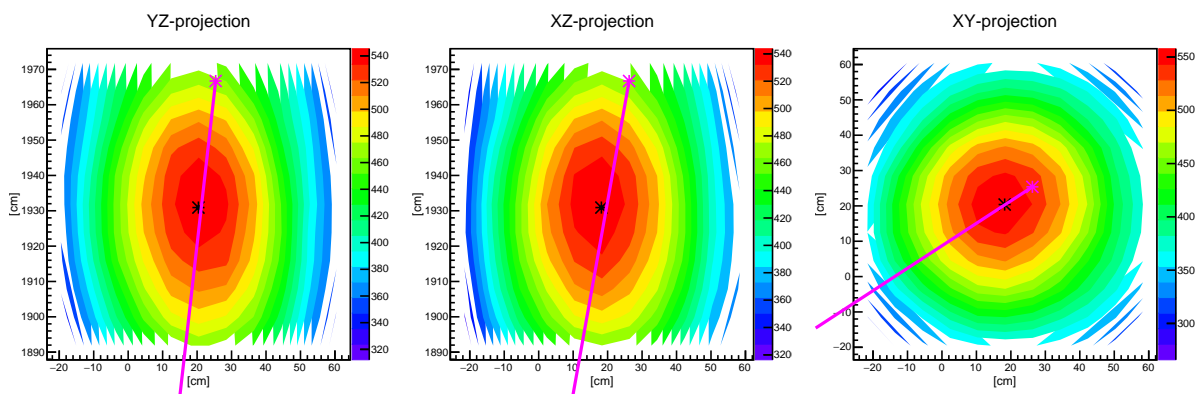


Figure 6.13: Example reconstruction for a HE event. The final iteration. The vertex (black mark) was reconstructed close to the track (pink track) about 35 cm away from the true vertex (pink mark). In the projection the value V for each grid point was added for a slice of 24 cm.

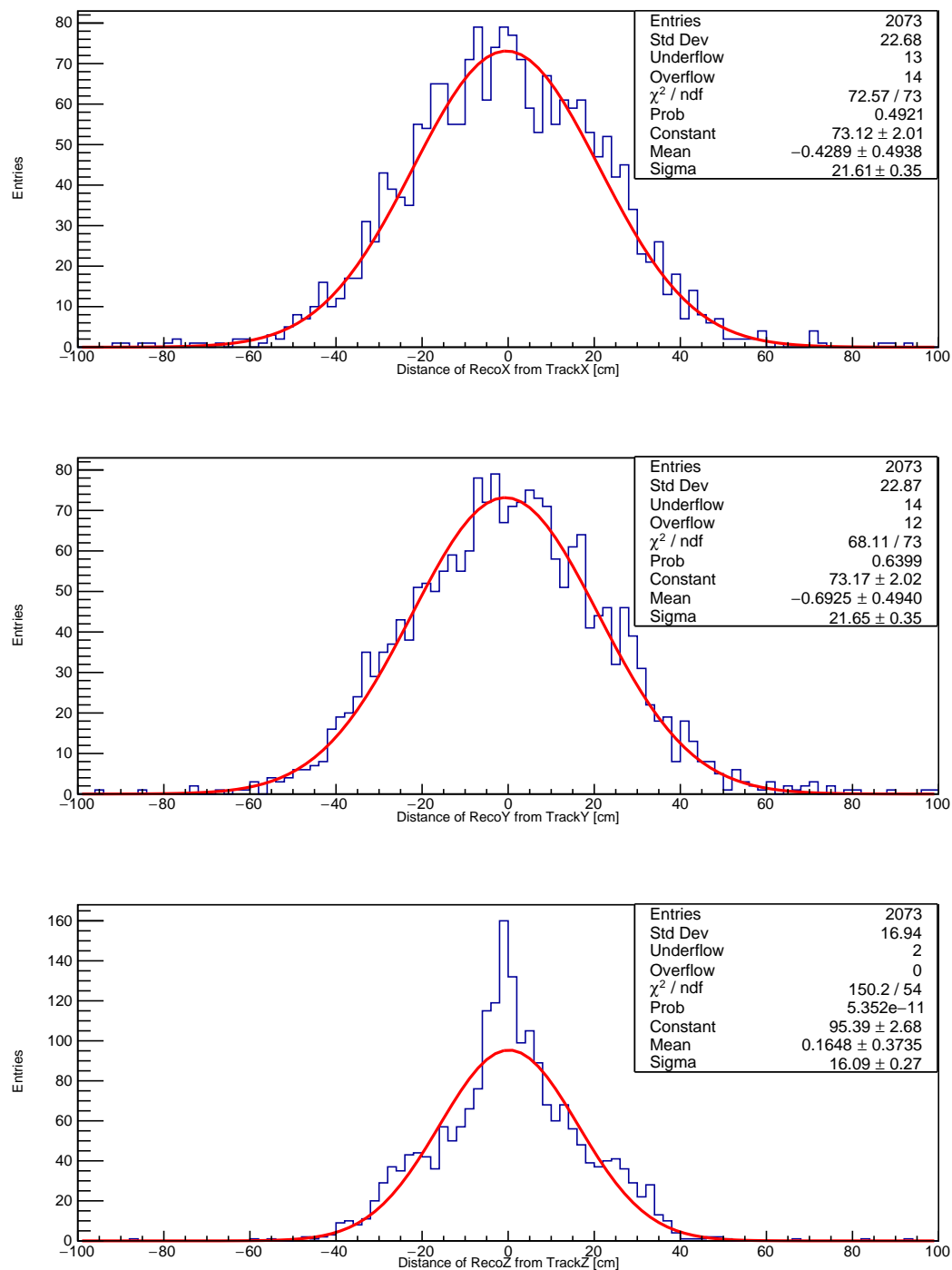


Figure 6.14: Distance from closest point on track to reconstructed vertex for each direction. A normal distribution is expected for each direction. Therefore a Gaussian distribution is fitted. The σ for the X distance is ± 21.61 cm, For the Y direction ± 21.65 cm and for the Z direction ± 16.09 cm.

and in Z direction ± 16.09 cm. For the total track position distance the standard deviation can be given by,

$$\sigma_{x,y,z} = \sqrt{\sigma_x^2 + \sigma_y^2 + \sigma_z^2} = 34.56 \text{ cm} . \quad (6.3)$$

The distance of the reconstructed vertex position to the track, for 2073 muon events, with an energy ranging from 5 GeV up to 10 GeV, was determined with a standard deviation of ± 34.56 cm.

Direction resolution The HE vertex reconstruction is depending on the reconstructed direction of the initial particle. A figure showing the angle difference between true direction and reconstructed direction can be seen in 6.15. For 99.2% of the 2500 muon events the direction

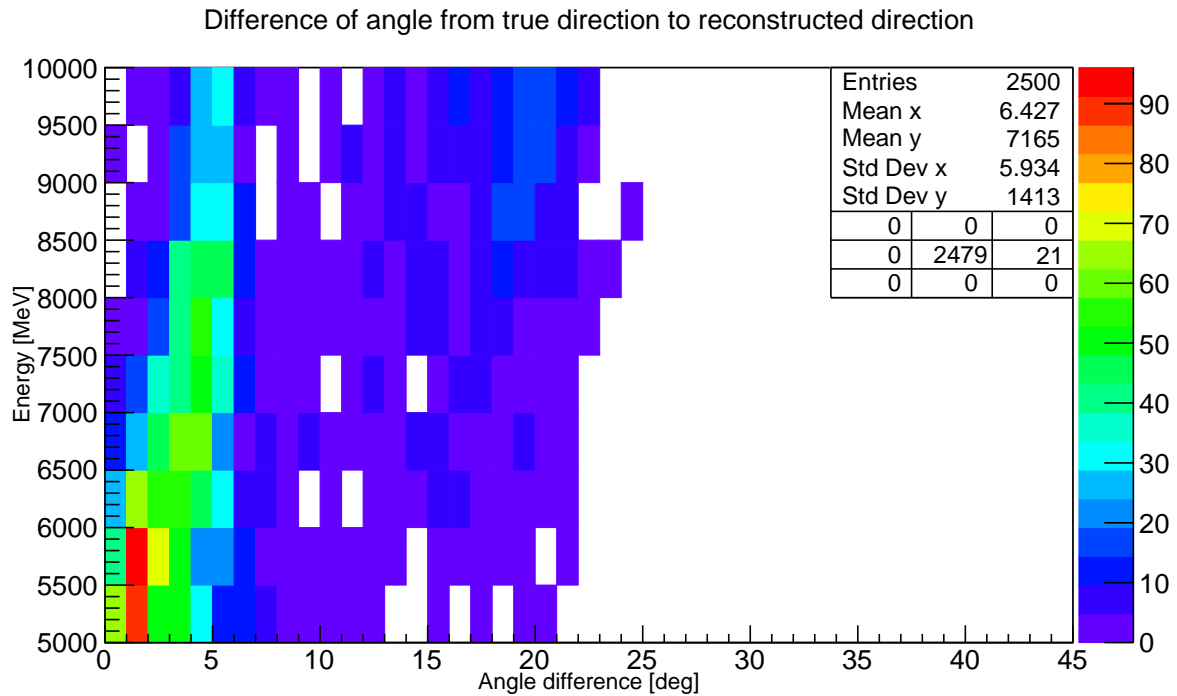


Figure 6.15: Angular difference of true direction to reconstructed direction, for HE events, depending on the energy of the event.

of the true track could be determined within a distance of 25 degrees and for 75.7% the true track directions could be determined within 7 degrees. This essentially means by expanding the solid angle Ω , by about 7 degrees, 75% of the HE events will not consider any first hits from the track light front (unless it was scattered). It is not possible to obtain a normal distribution of the angle difference, because two vectors can only create a radially symmetric system. The validity of results obtained by introduce a coordinate system that has nothing to do with the radial alignment of the vectors is insignificant.

6.2 JUNO-Detector

Events simulated in JUNO have been reconstructed. As a proof of concept, that the vertex reconstruction can be used for JUNO. The result of one of these reconstructions can be seen in figure 6.16. This is the reconstruction of a LE event in the center of the JUNO detector.

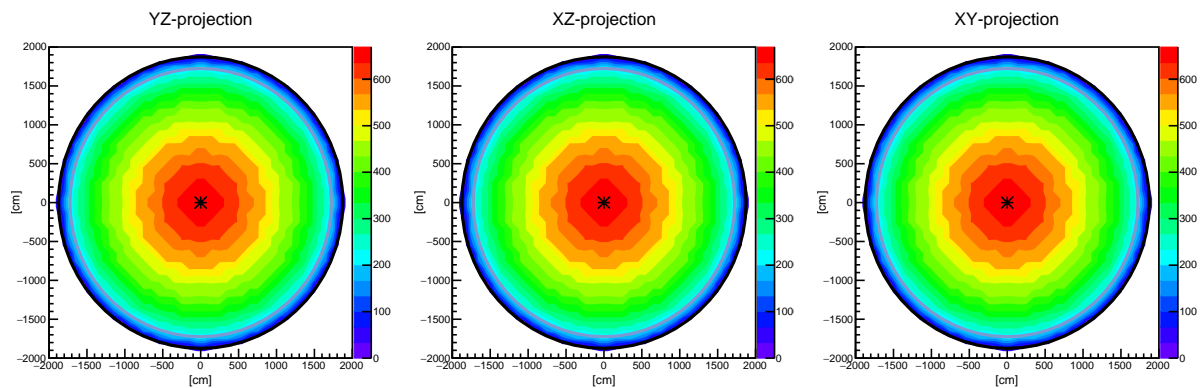


Figure 6.16: Example event, for a reconstruction of a JUNO event. A LE event was simulated in the center of the detector. The reconstruction is able to correctly determine the vertex in the center of the detector (black mark), but only due to symmetry effects. The reconstruction is not fully adapted to the JUNO geometry yet. The reconstruction was altered to expand the grid over the whole detector. The grid points have a distance of 1 m. The values V are added up in a slice of the depth of 10m.

The symmetry for an event in the center of the detector enables the reconstruction to correctly determine the vertex in the center. The vertex reconstruction can already be used with data simulated with the JUNO-simulation, but is not fully adapted yet. The different effects of the acrylic sphere and the water are not implemented yet. Therefore this preliminary result has to be seen as a proof of concept for the future development of this reconstruction.

Chapter 7

Conclusion and outlook

The aim of this thesis was the development of a vertex reconstruction, which is able to determine the start position and time of an event. Additionally the vertex reconstruction is needed to work with events in the energy range of a few MeV up to multiple GeV. Furthermore, the integration into the existing *Novel Track Reconstruction* project should be possible, without the need of recoding.

The vertex reconstruction developed during this thesis meets the stated requirements. It was designed to work with the *Novel Track Reconstruction Approach* and has already been used to determine the vertex in simulated events for the LENA-detector and the JUNO-detector. In principle this vertex reconstruction is able to work with any unsegmented liquid scintillator detector and does not rely on the geometry of the detector. It utilizes time-wise light propagation effects to determine the spatial event start. The event start time is reconstructed from the determined vertex position.

To test the performance of the algorithm, multiple events in the LENA detector have been reconstructed. For the energy range from 0.5 to 10.0 MeV, a sample of 10k electron events was simulated and reconstructed. 92.0% of the events could be reconstructed within a distance of 50 cm of the true vertex. The positional standard deviation for this sample is ± 14.06 cm and the event start time standard deviation is ± 0.33 ns. The time needed to reconstruct one of these low energy events is about 0.5 s, for 12 Intel Xenon X5650 CPUs with 2.67 GHz each.

To further comprehend these results, they have been analysed with regards to quality of the reconstruction for different positions inside the detector and variable weighting factors for detected photon hits. So far, the best results have been obtained around the center of the detector, with first hits information and by only applying the angular acceptance to weight the detected hits. Applying the survival probability has not provided the desired results. The main reason for this is the underestimation of time of flights, because light emission times, absorption with reemission, scattering and detection times, have been neglected. The equation used for the hit probability is an approximation and overestimates spatial regions near the optical modules.

In the future, the weighting factors will be adjusted to improve the reconstruction. This can be done by extending the equations for survival probability and the time-of-flight to also consider the delay effects mentioned. A lookup table created by a simulation could provide the necessary

adjustments. The approximation for the hit probability will be replaced to determine the near field probability correctly.

For the high energy range, of a few GeV, an already existing sample, of 2.5k contained muon events in the energy range from 5.0 to 10.0 GeV, was used. At the current stage the reconstructed vertex is found about 30 cm shifted along the particle track. This can be explained by underestimated photon time-of-flights. The position standard deviation as a distance to the particle track, for GeV events, was determined to be ± 34.56 cm and the time standard deviation is ± 0.27 ns. The time needed to reconstruct a GeV event is about 10 s, for 12 Intel Xenon X5650 CPUs with 2.67 GHz each.

The GeV range suffers even more from the effects of neglected light effects. The use of first hit information is suppressing the scattered light effects, but in the GeV range more light results in more first hits from scattered light as well. In a addition light from the track can further decrease the performance of the reconstruction.

To perform the high energy vertex reconstruction, the event direction is needed. Therefore, a algorithm for direction determination of GeV events in scintillator detectors was developed. The only precondition that is needed to use the algorithm is a point near the track of the event. To determine the performance of the direction reconstruction, the same 2.5k muon events have been used. For 99.2% of the events the direction of the true track could be determined within a distance of 25 degrees. For 75.7% the difference between true track and reconstructed track is less then 7 degrees. The algorithm takes a few milliseconds to execute.

Furthermore, the reconstruction has also been performed exemplarily with results provided by the JUNO detector simulation and in the near future will be fully applicable for the event reconstruction in the JUNO detector.

List of Figures

1.1	Pauli and letter of neutrino proposal	3
1.2	A schematic view of the Standard Model.	5
1.3	Diagrams describing the fusion processes in the sun.	11
1.4	A diagram showing the possible realisation for NO and IO.	17
2.1	This schematic shows the cherenkov wavefront.	23
2.2	A scheme of a common PMT layout.	25
2.3	Different possibilities for the creation of pre- and after-pulses.	25
2.4	A PMT with light concentrator.	26
2.5	The profile of a silicon strip detector.	27
2.6	The profile view of a LAPPD.	28
2.7	A cross section of the LENA detector.	31
2.8	The scintillation process anticipated for LENA.	32
2.9	The basic OM planned for LENA.	33
2.10	Reactor neutrino spectra in L/E space.	35
2.11	A profile view of the planned JUNO detector.	36
2.12	A concept view of a MCP-PMT.	38
3.1	LENA detector simulation geometrical layout.	40
3.2	Winston Cone acceptance histogram.	44
3.3	A schematic view showing the simulated geometry of the JUNO detector.	45
3.4	Refractive indices and absorption lengths in the JUNO simulation.	47
3.5	Wavelength dependent properties of the liquidcintillator in the JUNO simulation.	48
3.6	Example for a PMT implemented in the JUNO simulation.	49
4.1	The basic principal of the <i>Novel Track Reconstruction</i>	53
4.2	The time and energy reconstruction resolution for RecTimeLikeAlg.	56
5.1	A schematic for time of flight.	60
5.2	Example of time difference histograms	60
5.3	Layout of the grid.	64
5.4	Approximated angular acceptance.	66
5.5	The survival probability $P_{\text{surv}}(d)$	68

5.6	The hit probability $P_{\text{hit}}(d, \alpha)$	68
5.7	The TEH and a corresponding fit.	70
5.8	Schematic of a developing HE event.	71
5.9	Schematic for calculated time of flight to actual first hit time.	72
5.10	Example histograms for the direction finding algorithm.	73
6.1	Example for a reconstruction result.	75
6.2	Reconstruction result for 10k electron events.	77
6.3	Position reconstruction resolution for LE events.	78
6.4	Dependence of detector wall distance.	79
6.5	Radial distance from detector wall.	80
6.6	Example event for survival probability.	81
6.7	Example event for hit probability.	82
6.8	Reconstructed time for LE electron events.	83
6.9	Example reconstruction for a HE event.	84
6.10	HE event vertex reconstruction for time & position.	85
6.12	Shift of HE event reconstructed vertex.	88
6.13	Example reconstruction for a HE event.	88
6.14	Distance from closest point on track to reconstructed vertex.	89
6.15	Angular difference for HE events.	90
6.16	Example event, for a reconstruction of a JUNO event.	91

List of Tables

1.1	A best-fit result, for the squared masses and mixing angles. [28]	16
2.1	The variables used in the <i>Bethe-Bloch-equation</i> . [52]	21
2.2	Precision improvement for Δm_{21}^2 , $ \Delta m_{ee}^2 $ and $\sin^2(\Theta_{12})$	35
2.3	The needed radiopurity for liquid scintillator to be used in JUNO.	37
3.1	Table containing the geometric parameters used for the LENA event simulation.	40
3.2	Table describing the optical module distribution in LENA simulation.	41
3.3	Parameters for the liquid scintillator (LAB) used in LENA simulation.	42
3.4	The geometric parameters describing the JUNO detector in the simulation.	46
3.5	Number of PMTs used in the JUNO detector simulation.	46
3.6	The scintillation light decay times and corresponding weights in JUNO simulation.	48
4.1	List of reconstructions currently developed within the SNiPER framework	54

List of abbreviations and acronyms

BF	branching fraction
bis-MSB	1,4-Bis(2-methylstyryl) benzene
CC	charge current
CCD	Charge-coupled Device
CE	collection efficiency
CL	confidence level
CMB	cosmic microwave background
CNO	carbon–nitrogen–oxygen
DE	detection efficiency
DSNB	defuse supernova background
GERDA	Germanium Detector Array
GUT	Grand Unification Theory
HE	high energy
IBD	inverse β -decay
IO	inverted ordering
KATRIN	Karlsruhe Tritium Neutrino Experiment
JUNO	Jiangmen Underground Neutrino Observatory
LAB	linear alkylbenzene
LAGUNA	Large Apparatus for Grand Unification and Neutrino Astrophysics
LAPPD	Large-Area Picosecond Photo-Detectors
LE	low Energy
LENA	Low Energy Neutrino Astronomy
LSM	Laboratoire Souterrain de Modane
MC	Monte Carlo
MCP	multi channel plate
MO	mass ordering

MSW	Mikheyev-Smirnov-Wolfenstein
NC	neutral current
ndf	number of degrees of freedom
NN	nucleon-nucleon
NO	normal ordering
OM	optical module
PDE	photon detection efficiency
p.d.f.	probability density function
PE	photoelectron
PMNS	Pontecorvo–Maki–Nakagawa–Sakata
PMT	photomultiplier tube
pp	proton-proton
PPO	5-diphenyloxazole
QE	quantum efficiency
R&D	research and development
SK	Super Kamiokande
SN	supernova
SNEWS	SuperNova Early Warning System
SNiPER	Software for Non-collider Physics ExpeRiment
SM	standard model
SNO	Sudbury Neutrino Observatory
SSM	standard solar model
SSD	silicon strip detector
TDH	time difference histogram
TEH	time evaluation histogram
TOF	time of flight
TTD	transit time spread

Bibliography

- [1] M. G. Aartsen et al. Letter of Intent: The Precision IceCube Next Generation Upgrade (PINGU). 2014.
- [2] N. Agafonova et al. Discovery of τ neutrino appearance in the cngs neutrino beam with the opera experiment. *Phys. Rev. Lett.*, 115:121802, Sep 2015.
- [3] S. Agostinelli et al. GEANT4: A Simulation toolkit. *Nucl. Instrum. Meth.*, A506:250–303, 2003.
- [4] M. Agostini et al. Results on Neutrinoless Double- β Decay of ^{76}Ge from Phase I of the GERDA Experiment. *Phys. Rev. Lett.*, 111(12):122503, 2013.
- [5] M. Agostini et al. Spectroscopy of geoneutrinos from 2056 days of Borexino data. *Phys. Rev.*, D92(3):031101, 2015.
- [6] John Allison et al. Geant4 developments and applications. *IEEE Trans. Nucl. Sci.*, 53:270, 2006.
- [7] Fengpeng An et al. Neutrino Physics with JUNO. *J. Phys.*, G43(3):030401, 2016.
- [8] J. Angrik et al. KATRIN design report 2004. 2005.
- [9] I. Antcheva et al. Root - a c++ framework for petabyte data storage, statistical analysis and visualization. *Computer Physics Communications*, 180:2499–2512, December 2009.
- [10] T. Araki et al. Experimental investigation of geologically produced antineutrinos with KamLAND. *Nature*, 436(7050):499–503, Jul 2005.
- [11] V. N. Aseev et al. An upper limit on electron antineutrino mass from Troitsk experiment. *Phys. Rev.*, D84:112003, 2011.
- [12] G. Bellini et al. Cosmogenic Backgrounds in Borexino at 3800 m water-equivalent depth. *JCAP*, 1308:049, 2013.
- [13] J. B. Birks. *The Theory and Practice of Scintillation Counting: International Series of Monographs in Electronics and Instrumentation (Volume 27)*. Pergamon Press New York, 1964.

- [14] J. Boger et al. The Sudbury Neutrino Observatory. *Nuclear Instruments and Methods in Physics Research A*, 449:172–207, July 2000.
- [15] J. I. Crespo-Anadón. Double Chooz: Latest results. *Nucl. Part. Phys. Proc.*, 265-266:99–104, 2015.
- [16] G. Danby, J. M. Gaillard, Konstantin A. Goulianos, L. M. Lederman, Nari B. Mistry, M. Schwartz, and J. Steinberger. Observation of High-Energy Neutrino Reactions and the Existence of Two Kinds of Neutrinos. *Phys. Rev. Lett.*, 9:36–44, 1962.
- [17] Stefano Dell’Oro, Simone Marcocci, and Francesco Vissani. New expectations and uncertainties on neutrinoless double beta decay. *Phys. Rev.*, D90(3):033005, 2014.
- [18] Zelimir Djurcic et al. JUNO Conceptual Design Report. 2015.
- [19] Andrey Elagin. Large-Area Picosecond Photo-Detectors. University of Chicago, FroST - II Workshop, Mainz, 2016. <https://indico.mitp.uni-mainz.de/event/83/session/2/contribution/26/material/slides/0.pdf>.
- [20] Electron Tube Division. *PHOTOMULTIPLIER TUBE R12199*. HAMAMATSU PHOTONICS K.K., Arzbergerstr. 10, D-82211 Herrsching am Ammersee, Germany, 1 edition, July 2015. https://www.hamamatsu.com/resources/pdf/etd/R12199_TPMH1356E.pdf.
- [21] E. Fermi. Versuch einer Theorie der β -Strahlen. I. *Zeitschrift fur Physik*, 88:161–177, March 1934.
- [22] The Nobel Foundation. *Nobel Lectures*. Elsevier Publishing Company, Amsterdam, 1964.
- [23] The Nobel Foundation. The nobel prize in physics 1995. Nobelprize.org. Nobel Media AB 2014. Web. 25 Nov 2016. http://www.nobelprize.org/nobel_prizes/physics/laureates/1995/, 1995.
- [24] The Nobel Foundation. The nobel prize in physics 2015. Nobelprize.org. Nobel Media AB 2014. Web. 25 Nov 2016. http://www.nobelprize.org/nobel_prizes/physics/laureates/2015/, 2015.
- [25] S. Fukuda et al. Solar B-8 and hep neutrino measurements from 1258 days of Super-Kamiokande data. *Phys. Rev. Lett.*, 86:5651–5655, 2001.
- [26] Y. Fukuda et al. The Super-Kamiokande detector. *Nucl. Instrum. Meth.*, A501:418–462, 2003.
- [27] Carlo Giunti and Marco Laveder. Statistical Significance of the Gallium Anomaly. *Phys. Rev.*, C83:065504, 2011.
- [28] M. C. Gonzalez-Garcia, M. Maltoni, and T. Schwetz. Updated fit to three neutrino mixing: status of leptonic CP violation. *Journal of High Energy Physics*, 11:52, November 2014.

- [29] D. Hellgartner. Lepton track reconstruction in LENA and attenuation length measurements in liquid scintillators. Diploma thesis, Tech. U. Munich, 2011.
- [30] D. Hellgartner. *Advanced Event Reconstruction in LENA and Precision Attenuation-Length Measurements in Liquid Scintillators*. Dissertation, Tech. U. Munich, 2015.
- [31] Shunsaku Horiuchi, John F. Beacom, and Eli Dwek. The Diffuse Supernova Neutrino Background is detectable in Super-Kamiokande. *Phys. Rev.*, D79:083013, 2009.
- [32] H. Thomas Janka, Florian Hanke, Lorenz Huedepohl, Andreas Marek, Bernhard Mueller, and Martin Obergaulinger. Core-Collapse Supernovae: Reflections and Directions. *PTEP*, 2012:01A309, 2012.
- [33] JUNO collaboration. Basic Distributions of JUNO. Institute of High Energy Physics, Conference talk - JUNO software workshop Paris, 2016. http://juno.ihep.ac.cn/mediawiki/index.php/Analysis:Basic_Distributions_of_JUNO.
- [34] Soo-Bong Kim, Thierry Lasserre, and Yifang Wang. Reactor neutrinos. *Adv. High Energy Phys.*, 2013:453816, 2013.
- [35] H. V. Klapdor-Kleingrothaus and I. V. Krivosheina. The evidence for the observation of $0\nu\beta\beta$ decay: The identification of $0\nu\beta\beta$ events from the full spectra. *Mod. Phys. Lett.*, A21:1547–1566, 2006.
- [36] John G. Learned, Stephen T. Dye, Sandip Pakvasa, and Robert C. Svoboda. Determination of neutrino mass hierarchy and θ_{13} with a remote detector of reactor antineutrinos. *Phys. Rev. D*, 78:071302, Oct 2008.
- [37] W. R. Leo. *Techniques for Nuclear and Particle Physics Experiments: A How-to Approach*. Springer, 1992.
- [38] Yu-Feng Li, Jun Cao, Yifang Wang, and Liang Zhan. Unambiguous Determination of the Neutrino Mass Hierarchy Using Reactor Neutrinos. *Phys. Rev.*, D88:013008, 2013.
- [39] Tao Lin. JUNO Detector Simulation. Institute of High Energy Physics, Conference talk - JUNO software workshop Paris, 2016. <http://juno.ihep.ac.cn/offline/Doc/detsim/>.
- [40] S. Lorenz. *Topological Track Reconstruction in Liquid Scintillator and LENA as a Far-Detector in an LBNO Experiment*. Dissertation, Physik-Department, der Universität Hamburg, Dezember 2016.
- [41] Haoqi Lu. JUNO Detector Simulation. Institute of High Energy Physics, Conference talk - JUNO software workshop Paris, 2016.
- [42] G. Mention, M. Fechner, Th. Lasserre, Th. A. Mueller, D. Lhuillier, M. Cribier, and A. Letourneau. The Reactor Antineutrino Anomaly. *Phys. Rev.*, D83:073006, 2011.

- [43] R. Mitalas and K. R. Sills. On the photon diffusion time scale for the sun. *Astrophysical J.*, 401(2):759–760, 1992.
- [44] R. Möllenberg. *Monte Carlo Study of Solar ^8B Neutrinos and the Diffuse Supernova Neutrino Background in LENA*. Dissertation, Tech. U. Munich, 2013.
- [45] R. Möllenberg, Franz von Feilitzsch, Dominikus Hellgartner, Lothar Oberauer, Marc Tippmann, Vincenz Zimmer, Jürgen Winter, and Michael Wurm. Detecting the Diffuse Supernova Neutrino Background with LENA. *Phys. Rev.*, D91(3):032005, 2015.
- [46] Randolph Möllenberg, Franz von Feilitzsch, Dominikus Hellgartner, Lothar Oberauer, Marc Tippmann, Jürgen Winter, Michael Wurm, and Vincenz Zimmer. Detecting the upturn of the solar ^8B neutrino spectrum with LENA. *Phys. Lett.*, B737:251–255, 2014.
- [47] Dmitry V. Naumov. Recent results from Daya Bay experiment. *EPJ Web Conf.*, 95:04043, 2015.
- [48] L. Oberauer, C. Grieb, F. v. Feilitzsch, and I. Manno. Light concentrators for Borexino and CTF. *Nuclear Instruments and Methods in Physics Research A*, 530:453–462, September 2004.
- [49] H. M. O’Keeffe, E. O’Sullivan, and M. C. Chen. Scintillation decay time and pulse shape discrimination in oxygenated and deoxygenated solutions of linear alkylbenzene for the SNO+ experiment. *Nucl. Instrum. Meth.*, A640:119–122, 2011.
- [50] K. A. Olive et al. Review of Particle Physics. *Chin. Phys.*, C38:090001, 2014.
- [51] N. Palanque-Delabrouille, C. Yèche, J. Baur, C. Magneville, G. Rossi, J. Lesgourgues, A. Borde, E. Burtin, J.-M. LeGoff, J. Rich, M. Viel, and D. Weinberg. Neutrino masses and cosmology with Lyman-alpha forest power spectrum. *JCAP*, 11:011, November 2015.
- [52] C. Patrignani et al. Review of Particle Physics. *Chin. Phys.*, C40:100001, 2016.
- [53] W. Pauli. Open letter to the group of radioactive people. Copy of the original letter by Physics Institute of the ETH Zürich, Dezember 1956.
- [54] Liu Qin, Wu Wenjie, and Hec Miao. Vertex and Energy Reconstruction in SNIKER. USTC, Wuhan University and IHEP, Conference talk - JUNO software workshop Paris, 2016.
- [55] Georg G. Raffelt. Supernova neutrino observations: What can we learn? *Nucl. Phys. Proc. Suppl.*, 221:218–229, 2011.
- [56] G. Ranucci, A. Goretti, and P. Lombardi. Pulse-shape discrimination of liquid scintillators. *Nucl. Instrum. Meth.*, A412:374–386, 1998.
- [57] K. Scholberg. Supernova Neutrino Detection. *Annual Review of Nuclear and Particle Science*, 62:81–103, November 2012.

- [58] Kate Scholberg. SNEWS: The Supernova early warning system. 1999. [AIP Conf. Proc.523,355(2000)].
- [59] Kate Scholberg. Supernova Neutrino Detection. *Ann. Rev. Nucl. Part. Sci.*, 62:81–103, 2012.
- [60] Boris Schäling. *The Boost C++ Libraries*. 2011.
- [61] Seon-Hee Seo. New Results from RENO and The 5 MeV Excess. *AIP Conf. Proc.*, 1666:080002, 2015.
- [62] N. Serra. The standard model of particle physics. Technical report, Universität Zürich (UZH), 2015. www.physik.uzh.ch/groups/serra/StandardModel.html.
- [63] Tobias Stempfle. Reconstruction of Spatially Extended Events in Borexino. Master's thesis, Tech. U. Munich, 2013.
- [64] Nikola Tesla and Ben Johnston. *The Autobiography of Nikola Tesla*. Experimenter Publishing Company, Inc., New York, 1 edition, 1919.
- [65] B. von Krosigk, L. Neumann, R. Nolte, S. Rottger, and K. Zuber. Measurement of the proton light response of various LAB based scintillators and its implication for supernova neutrino detection via neutrino-proton scattering. *Eur. Phys. J.*, C73(4):2390, 2013.
- [66] M. Weber. Introduction to silicon detectors. Science and Technology Facilities Council, Rutherford Appleton Laboratory, 2006. http://www.ppd.stfc.ac.uk/PPD/resources/pdf/lecture02_weber.pdf.
- [67] D. R. Williams. NASA Sun Fact Sheet. <http://nssdc.gsfc.nasa.gov/planetary/factsheet/sunfact.html>, 2016.
- [68] J. M. Winter. Phenomenology of Supernova Neutrinos, Spatial Event Reconstruction, and Scintillation Light Yield Measurements for the Liquid-Scintillator Detector LENA. Diploma thesis, Tech. U. Munich, 2007.
- [69] Walter Winter. Neutrino tomography: Learning about the earth's interior using the propagation of neutrinos. *Earth Moon Planets*, 99:285–307, 2006. [,285(2006)].
- [70] M. Wurm. Status of LENA R&D. JGU Mainz, Conference talk - NNN 2014 at APC Paris, 2014. <http://indico.in2p3.fr/event/10162/session/9/contribution/30/material/slides/0.pdf>.
- [71] Michael Wurm et al. Optical Scattering Lengths in Large Liquid-Scintillator Neutrino Detectors. *Rev. Sci. Instrum.*, 81:053301, 2010.
- [72] M. Yeh, S. Hans, W. Beriguete, R. Rosero, L. Hu, R. L. Hahn, M. V. Diwan, D. E. Jaffe, S. H. Kettell, and L. Littenberg. A new water-based liquid scintillator and potential applications. *Nucl. Instrum. Meth.*, A660:51–56, 2011.

-
- [73] Liang Zhan, Yifang Wang, Jun Cao, and Liangjian Wen. Determination of the Neutrino Mass Hierarchy at an Intermediate Baseline. *Phys. Rev.*, D78:111103, 2008.
- [74] H. Zhang et al. Supernova Relic Neutrino Search with Neutron Tagging at Super-Kamiokande-IV. *Astropart. Phys.*, 60:41–46, 2015.
- [75] J. H. Zou, X. T. Huang, W. D. Li, T. Lin, T. Li, K. Zhang, Z. Y. Deng, and G. F. Cao. Sniper: an offline software framework for non-collider physics experiments. *Journal of Physics: Conference Series*, 664(7):072053, 2015.
- [76] K. Zuber. *Neutrino Physics*. Series in High Energy Physics, Cosmology and Gravitation. CRC Press, 2 edition, 2011.

Acknowledgment

Thank you. Thanks to my parents for the support, that you gave me during this thesis. Thanks to Prof. Dr. Caren Hagner for the opportunity to write this thesis and for always being open and supportive about any questions I had. Thanks to Dr. Björn Wonsak for the interesting and important topic of this thesis and for all the support about physics and the reconstruction. Thanks to Dr. Sebastian Lorenz for all the help with the reconstruction. Thanks to Henning Rebber for the fun times in Paris and for the correction of this thesis. Thanks to Dr. Björn Opitz for the correction of this thesis. Thanks to Stefan Bieschke for the countless time that we decided to become helicopter pilots and all the other fun stuff. Thanks to Felix Benckwitz for the fun talks and coming as late to the office as myself. Thanks to Hauke Schmidt for the assistance with any computer related questions and the parallelization of the reconstruction. Thanks to the *Bier um 4* cooperative. In general, thanks for the pleasant atmosphere, created by all the people in the *Forschungsgruppe Neutrinophysik*: Prof. Dr. Walter Schmidt-Parzefall, Dr. Daniel Bick, Dr. Joachim Ebert, Hans-Jürgen Ohmacht, Benjamin Büttner, Annika Hollnagel, Mikko Meyer, Lisa Steppat, Daniel Hartwig, Benedict Kaiser, Simon Reichert, Benedict Schacht, Katarina Voss and Bosse Bein.

Erklärung

Hiermit bestätige ich, dass die vorliegende Arbeit von mir selbständig verfasst wurde und ich keine anderen als die angegebenen Hilfsmittel – insbesondere keine im Quellenverzeichnis nicht benannten Internet-Quellen – benutzt habe und die Arbeit von mir vorher nicht einem anderen Prüfungsverfahren eingereicht wurde. Die eingereichte schriftliche Fassung entspricht der auf dem elektronischen Speichermedium. Ich bin damit einverstanden, dass die Masterarbeit veröffentlicht wird.

Hamburg, December 19, 2016

David J. Meyhöfer